POLITECNICO DI MILANO
DIPARTIMENTO DI ENERGIA
CORSO DI DOTTORATO IN ENERGETICA

MULTI-DIMENSIONAL SIMULATION OF INTAKE AND EXHAUST SYSTEMS FOR INTERNAL COMBUSTION ENGINES

Doctoral dissertation of:
Andrea Montorfano, 738613

Tutor and supervisor:
prof. Angelo Onorati

The Chair of the Doctoral Program:
prof. Carlo E. Bottani

XIV cycle – 2012

sbroccati, ma lieti:
è Dio che fa.

Abstract

Multi-dimensional Computational Fluid Dynamics (CFD) techniques applied to Internal Combustion Engines (ICE) problems are the subject of the present work.

In the first part, an original approach for the simulation of wallflow Diesel Particulate Filters (DPF) by the Finite Volume Method is presented. Filtrating walls are modeled as porous membranes with an associated pressure drop term, while monolith channels are simplified as one-dimensional arrays of FV cells. By this method, it is possible to simulate within the same fluid domain both the full-scale particulate trap and the inlet-outlet pipes. Results are obtained both at the global scales and at the filter channel scale. The model includes also particulate matter transport and deposition in order to study the filter loading cycle. Simulations have been validated by comparison against experimental data. The solver exhibits great accuracy both in terms of global quantities and at channel-scale level and also very good predictivity.

In the second part, Large Eddy Simulation of the ERCOFTAC test case n. 83 (wall-mounted hump) is presented. The purpose is to study the influence of some setup parameters on a channel flow case with separation. In particular, the influence of the inlet boundary condition is investigated, by comparing the following models: fixed velocity profile, mapping plane and synthetic turbulence generation. Simulations results are validated against reference measurements, showing some discrepancies. The influence of near wall mesh and subgrid model is discussed as well.

Keywords Computational Fluid Dynamics, CFD, Internal Combustion Engines, Diesel Particulate Filters, DPF, porous media, Large Eddy Simulation, LES, wall-mounted hump, synthetic turbulence.

Acknowledgements

My gratitude is, on top of all, to all the people of the Internal Combustion Engine group at Politecnico di Milano, in particular to Professor Giancarlo Ferrari and my tutor, Professor Angelo Onorati. Also, special thanks to Professor Federico Piscaglia who supported and supervised me throughout all my research activity.

First part of my research (Diesel Particulate Filters) has been partially sponsored by Fiat Powertrain Technologies, whose financial support is gratefully acknowledged.

Research about Large Eddy Simulation has been primarily carried out at Chalmers University of Technology, Göteborg, Sweden. I am profoundly indebted to Prof. Lars Davidson, head of the Division of Fluid Dynamics, and Prof. Håkan Nilsson, who gave me this opportunity and supported me during this time. Computation resources for this part of the project have been made available by LUNARC (Center for scientific and technical computing, Lund University) through SNIC (Swedish National Infrastructure for Computing).

Finally, I wish to express my gratitude to my family and all of my *gesàtt* friends, for they never will me lack for their love and their loyalty.

Andrea Montorfano
March 2012

Contents

Introduction

Among different technologies for power generation, internal combustion engines play a dominant role in many fields, where low to medium energy power is requested but, on top of all, simplicity and compactness are required. Automotive propulsion, in particular, is almost completely done with gasoline or Diesel engines (the both of them covers the 97.1% of EU passenger cars fleet [2], not counting NG or LPG engines). Also, commercial vehicles rely totally on ICEs, either in the traditional or hybrid fashion.

As a consequence, research and development in automotive industry are continuously advancing, while their main focus shifts according to upcoming priorities. Recently, the most of research efforts are directed towards increasing efficiency and reducing polluttants: from 1995 to 2008, average CO_2 output of passenger cars has fallen by 20%, while polluting emissions dropped by more than 86% for NOx and 95% for Particulate Matter (PM) since regulatory norm Euro 0 was introduced [1].

The design of a modern clean and efficient engine requires a deep comprehension of the underlying physics and an accurate design of all critical components. Among all processes involved, at the moment the most important ones are those related with the gas exchange and combustion stages, since they are directly responsible for engine performance and emissions. A detailed study of occuring phenomena can be done either experimentally or by simulation.

In this context, simulations by means of Computational Fluid Dynamics (CFD) techniques have gained more and more importance, due to the level of detail that can be obtained in a relatively short time. Even prior to the prototyping stage, numerical analysis of some components (like cylinder head, intake ducts, aftertreatment devices) can show critical points and help improving the design, with clear cost-effective benefits. The present thesis work originates in such a context.

1 CFD for ICEs

CFD techniques for engines can be divided into two families. On one hand, we have one-dimensional methods [92, 91, 85], that allows for simulating the whole gas path through the intake and exhaust systems. They are usually accurate and fast, but level of detail is not great.

On the other hand, we have multi-dimensional methods that are used for studying a narrower part of the domain (like a single component or device), but that can provide data with a greater level of detail. Our present work belongs to the latter family.

Multi-D methods are usually divided into three categories [67]: Finite Volumes, Finite Differences and Finite Elements. Among them, the Finite Volume Method is probably the most popular, due to its ease of implementation, even for complex geometries. Also, the physics of the problem can be extended as needed, since including new models is very intuitive and free from any conceptual difficulty. On the other hand, FVM suffers of a lower accuracy with respect to other methods (convergence order can hardly be more than two) and error analysis is quite complicated.

All algorithms and procedures reported in the present thesis work have been developed in the FV framework and implemented in the open-source code OpenFOAM® [90, 62]. The adoption of an open-source software was somehow forced by our need to extend the code as needed; also, it allowed us to have a deep insight into the program structure and to gain a thorough knowledge of all procedures used.

2 Structure of the work

By definition, all phenomena that involve a fluid phase can be simulated with CFD, that means that every component of the gas path of an ICE might be the object of the present work. But research had to be narrowed and focused on some parts, namely, Diesel Particulate Filters and turbulent channel flow.

Diesel Particulate Filters, described in details in section 1, are devices used to remove solid particles from exhaust gases of Diesel engines. At the moment, this is the only technology that is able to strongly reduce (up to 99%) Particulate Matter emission. As it will be shown, despite their adoption is now well estabilished, only a few comprehensive and accurate modeling approaches do exist. Our attempt will be to design and implement a novel procedure to overcome some of the limitations of the other methods.

Another open problem of CFD, and fluid-dynamics in general, is connected to turbulence [66]. Its accurate modeling is of foremost importance in many fields, and especially to predict performance of an ICE, since it affects any stage of gas exchange process, intake

stroke and combustion. Currently, many turbulence modeling solutions rely on Large Eddy Simulation. Increasing computing power available to both academia and industry widened the use of this technique, once limited to specialized high-performance computing or fundamental research. Though quite simple in its application, the mathematics implied in LES approach is quite complex and many factors have to be taken into account for a correct application and interpretation of results. The present work aims at evaluating the influence of the inlet boundary condition on a relevant LES test-case that, despite is not engine-related, has a wide set of reference data for comparison.

The structure of this thesis is as follows. In the rest of this chapter, sections 3 and 4, respectively the fundamental equations of fluid dynamics and the basics of FVM will be briefly recalled, to set up some reference points.

Chapter 1 and 2 will be devoted to DPF modeling: the problem will be first outlined in sections 1.1 and 1.2, then a review of the present state-of-art (section 1.3) follows. Modeling approach will be detailed in sections 1.4 (hydrodynamics part) and 1.5 (soot transport and deposition). Results and discussion are presented in chapter 2.

Second part of the work (chapters 3 and 4) is about LES. In chapter 3, the test case used for our investigations is presented together with experimental reference data and numerical setup. Afterwards, results are reported and discussed in chapter 4.

3 Governing equations

The object of the present study is the behavior of gas flows through engine ducts and devices by means of Computational Fluid Dynamics: although the actual flow conditions may vary from one case to another, the same set of governing equations can be used as a physical basis to the simulation work. Equations will be presented here for completeness and to highlight some underlying hypotheses that are often omitted: from time to time such hypotheses will be verified in the rest of the work.

All of the following equations are written under the *continuum hypothesis*: the fluid is continuosly distributed throughout its volume and completely fills the space it occupies [57]. In other words, time and length scale of all the involved phenomena are much greater than the discrete structure of matter and all fluid properties can be regarded as continuous functions of space and time. Moreover, only the case of a monophase fluid will be studied.

According to the continuum hypothesis, it is possible to define a control volume Ω, whose boundary is $S = \partial\Omega$, and to write the conservation equation of the generic physical property ϕ:

$$\frac{d}{dt}\int_{\Omega} \rho\phi(\mathbf{x}, t)\,\mathrm{d}\Omega = \int_{\Omega} Q_{\phi}\,\mathrm{d}\Omega \tag{1}$$

The LHS of Eq. (1) is called *material derivative* of ϕ, and represents its total variation in time:

$$\frac{d}{dt}\int_\Omega \rho\phi(\mathbf{x},t)\mathrm{d}\Omega = \frac{\partial}{\partial t}\int_\Omega \rho\phi(\mathbf{x},t)\mathrm{d}\Omega + \int_S \rho\phi(\mathbf{x},t)\mathbf{U}\cdot\mathbf{n}\mathrm{d}S \tag{2}$$

where $\mathbf{U}$ is the fluid velocity and $\mathbf{n}$ is the surface normal vector of S. Q_ϕ is a generic source for ϕ. Eq. (1) can be rewritten as:

$$\frac{\partial}{\partial t}\int_\Omega \rho\phi(\mathbf{x},t)\,\mathrm{d}\Omega + \int_S \rho\phi(\mathbf{x},t)\mathbf{U}\cdot\mathbf{n}\,\mathrm{d}S = \int_\Omega Q_\phi\,\mathrm{d}\Omega \tag{3}$$

The first term on LHS of Eq. (3) is also called 'first time derivative term' and the second one 'convection term'; the latter represents the variation of ϕ within the control volume as a consequence of advection by the fluid velocity, and can also be written in the following form by means of the Gauss theorem:

$$\int_S \rho\phi\mathbf{U}\cdot\mathbf{n}\,\mathrm{d}S = \int_\Omega \nabla\cdot(\rho\phi\mathbf{U})\,\mathrm{d}\Omega \tag{4}$$

Finally, if the control volume is constant with time, it is possible to express the balance equation for ϕ in the following indefinite form:

$$\frac{\partial\rho\phi}{\partial t} + \nabla\cdot(\rho\phi\mathbf{U}) = Q_\phi \tag{5}$$

3.1 Continuity equation

Continuity equation governs the mass conservation in the domain:

$$\frac{\partial\rho}{\partial t} + \nabla\cdot(\rho\mathbf{U}) = 0 \tag{6}$$

If the fluid is incompressible (ρ = constant), the above equation can be simplified as:

$$\nabla\cdot\mathbf{U} = 0 \tag{7}$$

3.2 Momentum equation

The momentum equation of a compressible fluid with body forces, reads [26]:

$$\frac{\partial}{\partial t}\int_\Omega \rho\mathbf{U}\mathrm{d}\Omega + \int_S \rho\mathbf{U}\mathbf{U}\cdot\mathbf{n}\mathrm{d}S = \int_S \boldsymbol{\sigma}\cdot\mathbf{n}\mathrm{d}S + \int_\Omega \rho\mathbf{b}\mathrm{d}\Omega \tag{8}$$

or, exploiting Gauss theorem:

$$\frac{\partial\rho\mathbf{U}}{\partial t} + \nabla\cdot\rho\mathbf{U}\mathbf{U} = \nabla\cdot\boldsymbol{\sigma} + \rho\mathbf{b} \tag{9}$$

where $\boldsymbol{\sigma}$ is the stress tensor and $\mathbf{b}$ are the body forces.

Into the stress tensor, two contributions can be considered, namely, pressure and viscous effects:

$$\sigma_{ij} = (-p + 2\lambda \nabla \cdot \mathbf{U})\delta_{ij} + \tau_{ij} \tag{10}$$

τ_{ij} is the viscous stress tensor, which depends on the fluid type. For newtonian fluids, the definition of τ_{ij} is:

$$\tau_{ij} = 2\mu S_{ij} + \lambda S_{kk}\delta_{ij} \tag{11}$$

where S_{ij} is the rate of strain tensor:

$$S_{ij} = \frac{1}{2}\left(\frac{\partial u_i}{\partial x_j} + \frac{\partial u_j}{\partial x_i}\right) \tag{12}$$

Thus, the hydrostatic part of σ_{ij} can be written as:

$$\frac{1}{3}\sigma_{kk} = -p + \lambda S_{kk} + \frac{2}{3}\mu S_{kk} \tag{13}$$

For incompressible fluids, since $\nabla \cdot \mathbf{U} = 0$, the hydrostatic part of σ_{ij} is identically equal to the pressure p. For compressible fluids, since $\nabla \cdot \mathbf{U} \neq 0$, generally it is assumed that:

$$\lambda + \frac{2}{3}\mu = 0 \tag{14}$$

so that the viscosity enters only the deviatoric part of σ and the hydrostatic part is equal to the thermodynamic pressure everywhere. The latter condition is called *Stokes hypothesis* and it is generally assumed as true, though this fact has not been conclusively demostrated yet; in particular, some doubts subsist when the fluid undergoes non-equilibrium thermodynamic changes like acoustic waves [22]. In the remainder of this study, however, the Stokes condition will be assumed as true everywhere.

From the above considerations, the usual form of the momentum equation arises, with the pressure term explicitly written as (summation convention applies):

$$\frac{\partial \rho \mathbf{U}}{\partial t} + \nabla \cdot (\rho \mathbf{U}\mathbf{U}) = -\nabla p + \nabla \cdot (\mu \boldsymbol{S}) + \rho \mathbf{b} \tag{15}$$

3.3 Energy equation

For most engineering flows, the energy of the fluid can be represented by its enthalpy, whose conservation equation reads:

$$\frac{\partial \rho h}{\partial t} + \nabla \cdot (\rho h \mathbf{U}) = \nabla \cdot (k \nabla T) + \mathbf{U} \cdot \nabla p + \boldsymbol{\sigma} : \nabla \mathbf{U} + \frac{\partial p}{\partial t} \tag{16}$$

The meaning of various terms on RHS of Eq. (16) is:

- $\nabla \cdot (k \nabla T)$ heat tranfer by conduction (Fourier's Law)

- $\mathbf{U} \cdot \nabla p + \partial p / \partial t$ work made by pressure forces
- $\boldsymbol{\sigma} : \nabla \mathbf{U}$ work made by viscous stresses and pressure forces

In the case of an incompressible fluid with constant specific heat, the energy equation may be simplified to a convection/diffusion equation for temperature:

$$\frac{\partial \rho T}{\partial t} + \nabla \cdot (\rho T \mathbf{U}) = \nabla \cdot \left(\frac{\mu}{\mathrm{Pr}} \nabla T \right) \tag{17}$$

3.4 Passive scalars

The conservation equation for a generic passive scalar can be written by taking into account convection, diffusion and source terms:

$$\frac{\partial \rho \phi}{\partial t} + \nabla \cdot (\rho \phi \mathbf{U}) = \nabla \cdot \left(\Gamma_k \nabla \phi \right) + Q_\phi \tag{18}$$

4 The Finite Volume Method

The Finite Volume methodology for solving partial differential equations like those shown in section 3 is well estabilished at the time this study is carried out [26, 87]. Only a few concepts will be recalled for they will serve as a basis in the following chapters. Unless otherwise specified, all numerical techniques described here are also implemented in OpenFOAM® .

4.1 Discretization of differential operators

4.1.1 Time discretization

The time derivative term is usually discretized by means of a finite-difference ratio. The simplest scheme is the Euler one:

$$\frac{\partial \phi}{\partial t} \approx \frac{\phi^n - \phi^{n-1}}{\Delta t} \tag{19}$$

where the superscript n denotes the timestep number and Δt is the duration of the time step itself. Euler scheme has order of accuracy equal to 1.

More sophisticated methods are the backward differencing scheme (second order):

$$\frac{\partial \phi}{\partial t} \approx \frac{3\phi^n - 4\phi^{n-1} + \phi^{n-2}}{2\Delta t} \tag{20}$$

and the Crank-Nicholson blended scheme (first-second order):

$$\frac{\partial \phi}{\partial t} \approx (1+\alpha) \left[\frac{\phi^n - \phi^{n-1}}{\Delta t} - \alpha(1+\alpha) \frac{\phi^{n-1} - \phi^{n-2}}{\Delta t} - \alpha \phi_{\partial t}^{n-2} \right] \tag{21}$$

The order of the method is chosen by varying the coefficient α: if $\alpha = 1$ the method is a pure Crank-Nicholson differencing scheme (second order); if $0 < \alpha < 1$ a blending with an Euler scheme is gradually applied to improve stability; with $\alpha = 0$ the formulation reduces to pure Euler scheme.

4.1.2 Space discretization

Discretization of the space domain is done by splitting the geometry in several small volumes with an arbitrary (but usually simple) shape. Treatment of physical quantities can be done according to either the *colocated* or the *staggered* arrangement.

Within the *colocated* arrangement, all variables of interest (pressure, velocity, energy, temperature, etc) are associated with the center of the computational cell, while *fluxes* of extensive quantities are calculated on the cell faces (see Fig. 1). Such an approach is simpler to implement on complex grids with respect to the *staggered* arrangement (where velocity is put at cell vertices instead than center) but it poses some issues from a computational point of view [87] and some modifications to interpolation schemes must be done. From now on, the use of a colocated scheme will be implied, since it is the same approach implemented in OpenFOAM® .

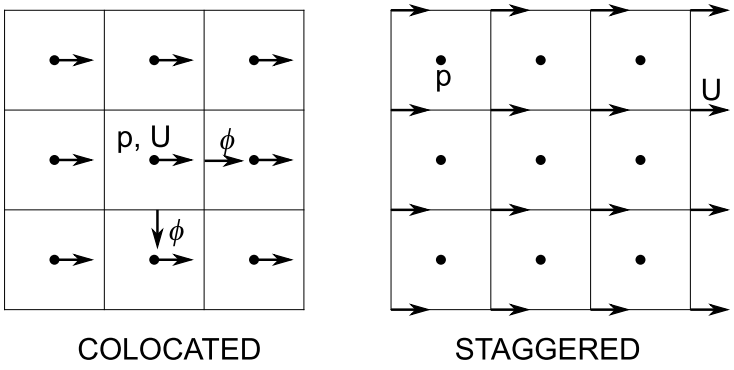

Figure 1: Classic variable arrangement used in FV. Left: in colocated approach, pressure and velocity are both located at cell centers. Right: in a staggered arrangement, pressure is at cell centers, whereas velocity is at grid nodes.

Calculation of spatial derivatives is based on the Gauss theorem in its generalized form, written for the discrete case (23). In this case the computational cell is supposed to be a polyhedron with N_f faces, and all surface quantites are constant along each cell face.

$$\int_\Omega \nabla \star \psi \, \mathrm{d}\Omega = \int_S \psi \star \mathrm{d}\mathbf{S} \tag{22}$$

$$\approx \sum_{i=1}^{N_f} \psi_f \star \mathbf{S_i} \tag{23}$$

where $(\star)$ is used to denote either inner product or dot product and $\mathbf{S_i}$ is the outward normal surface vector of face i. Therefore, the discretization of differential operators can be seen as a mere interpolation problem, to compute face-centered quantities:

$$\psi_w = \alpha_w \psi_P + (1 - \alpha_w)\psi_W \tag{24}$$

Values of interpolation weights α_w depend on the chosen scheme (pure linear, upwind, limited, ...). Results of interpolation can enter either the RHS of the problem or the coefficients matrix, depending on whether the variable is considered explicitly or not.

Gradient Gradients at cell centers can be calculated using Eq. (25):

$$\int_\Omega \nabla\psi \, \mathrm{d}\Omega \approx \sum_{i=1}^{N_f} \psi_f \mathbf{S_i} \tag{25}$$

or by a Least-Squares method [61, 62]. If Gauss theorem is used, values of ψ_f are computed using linear interpolation between cell-centered values.

On the other hand, if face-normal gradient is needed, it can be computed directly as a finite difference between cell-centered values (refer to Fig. 2):

$$\nabla^\perp_w \psi = \frac{\psi_P - \psi_W}{(P - W)\cdot \mathbf{n}} \tag{26}$$

where $\mathbf{n} = \mathbf{S}/\|\mathbf{S}\|$ and $(P - W)$ is the distance vector between cell centers.

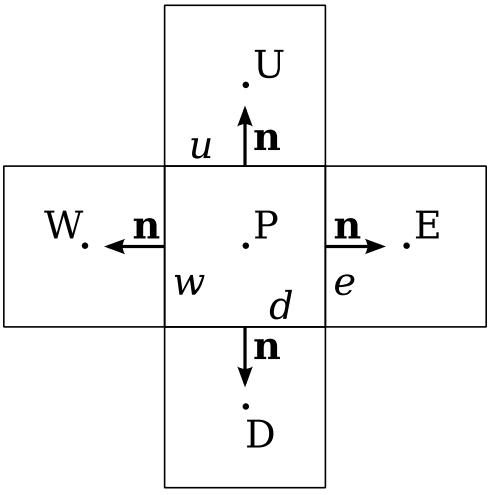

Figure 2: Schematic of a FV computational molecule. Considered cell is 'P', whereas neighbouring cells are denoted with names (W, E, U, D). **n** is the outward face-normal vector.

Divergence Gauss theorem can be applied to divergence too, leading to:

$$\int_\Omega \nabla \cdot \mathbf{U} \, \mathrm{d}\Omega \approx \sum_{i=1}^{N_f} \mathbf{U_f} \cdot \mathbf{S_i} \tag{27}$$

If the divergence term is computed explicitly, usually the interpolated field on faces is obtained by linear interpolation. On the other hand, when the divergence operator represents the convection term in governing equations, it is computed implicitly and different interpolation schemes can be used to to ensure boundedness (e.g. upwind, TVD limited, QUICK, etc.).

Laplacian Laplacian term can be computed using Gauss theorem as well:

$$\int_\Omega \nabla^2 \psi \, \mathrm{d}\Omega = \int_\Omega \nabla \cdot (\nabla \psi) \, \mathrm{d}\Omega \approx \sum_{i=1}^{N_f} \nabla_f^\perp \psi \cdot \mathbf{S_i} \tag{28}$$

In this case the face-centered gradient is computed using Eq. (26) with, if needed, a correction term to take into account mesh non-orthogonality. Computing the laplacian term this way allows for a better treatment of pressure-velocity coupling since we can take advantage of Rhie-Chow interpolation [69] and obtain checkerboarding-free pressure and velocity fields, even if a nonstaggered variable arrangement is used [43].

4.2 Pressure-velocity coupling

Pressure appears in momentum equation (15) as a surface force, that drives the flow in absence of other source terms. However, velocity field is also subjected to continuity equation, that may be regarded (at least for incompressible flows) as a kinematic constraint. Thus, a strong connection exists between pressure gradient and continuity, and therefore it is important that pressure field is constructed in such a way that guarantees continuity. Such a problem is generally called the pressure-velocity coupling problem. In the following paragraphs, we will briefly explain the pressure-velocity coupling techniques used in segregated solvers, like OpenFOAM® PISO and SIMPLE.

The basic idea is that pressure can be inserted in continuity equation by taking the divergence of momentum equation and using continuity to simplify the resulting expression, to finally obtain a Poisson equation for pressure:

$$\nabla \cdot (\nabla p) = -\nabla \cdot \left[\nabla \cdot (\rho \mathbf{U}\mathbf{U} - \boldsymbol{S}) - \rho \mathbf{b} + \frac{\partial \rho \mathbf{U}}{\partial t} \right] \tag{29}$$

The above expression (29) can be further simplified if considering constant density and viscosity, leading to the common expression used in incompressible solvers:

$$\nabla \cdot (\nabla p) = -\nabla \cdot \left[\nabla \cdot (\rho \mathbf{U}\mathbf{U} \right] \tag{30}$$

The coupling algorithms implemented in OpenFOAM rely on the following procedure that belongs to the class of pressure-correction methods. Several variants of the method described below exist (SIMPLE, SIMPLEC, SIMPLER, PISO), but the OpenFOAM implementations of the general PISO/SIMPLE algorithm are based on the following canvas.

Once the FV discretization has been performed, the momentum equation can be written as:

$$A_P u_{i,P}^{n+1} + \sum_l A_l u_{i,l}^{n+1} = Q^{n+1} - \left(\frac{\partial p^{n+1}}{\partial x_i}\right)_P \tag{31}$$

where A are the system matrix cofficients, for $P = 1 \dots N_{\text{cells}}$ and $l = 1 \dots N_{\text{neighbors of P}}$. A *predicted* velocity, that does not satisfy continuity, can be computed as:

$$u_{i,P}^{*} = \frac{Q^n - \sum_l A_l u_{i,l}^n}{A_P} - \frac{1}{A_P}\left(\frac{\partial p^n}{\partial x_i}\right)_P \tag{32}$$

where the first term on RHS of Eq. (32) can be written as $\tilde{u}_{i,P}$ for convenience. Then, predicted velocity is inserted into continuity equation leading to a Poisson equation for corrected pressure:

$$\frac{\partial}{\partial x_i}\left[\frac{\rho}{A_P}\frac{\partial p^{n+1}}{\partial x_i}\right]_P = \left[\frac{\partial \rho \tilde{u}_i}{\partial x_i}\right]_P \tag{33}$$

Finally, corrected velocity is obtained from corrected pressure as:

$$u_i^{n+1} = \tilde{u}_{i,P} - \frac{1}{A_P}\left(\frac{\partial p^{n+1}}{\partial x_i}\right)_P \tag{34}$$

In OpenFOAM the system matrix diagonal coefficients are indicated with the symbol $\mathscr{A}_P$, whereas the expression $Q^n - \sum_l A_l u_{i,l}^n$ with the symbol $\mathscr{A}_H$: this notation will be used from now on.

Chapter 1

Modeling of Diesel Particulate Filters

More stringent limits on emissions for Diesel engines adopted in Europe and in the US require the use of after-treatment devices both on heavy and light duty engines. Diesel Particulate Filters (DPF) are currently the most common technology used to reduce Particulate Matter (PM) emissions in diesel fueled passenger cars. Depending on their material, DPF have shown high filtration efficiencies (frequently in excess of 92%) and thermal durability. Among different technologies, wallflow DPFs play a dominant role, due to their low flow resistance compared to the filtration efficiency [25]. A sketch of a wall-flow filter is depicted in fig. 1.1. The basic structure of a wallflow trap is composed by a ceramic monolith with a honeycomb design. Filter channels (whose width has an order of magnitude of 1 mm) are alternately open and closed, so that channels that have an open end on a filter frontal section are closed on the opposite side, and vice-versa. A schematic of a channel pair with conventional names of its parts is represented in fig. 1.3

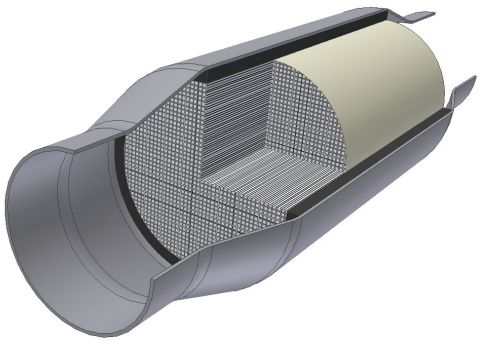

Figure 1.1: Cutaway view of a DPF inserted in an exhaust duct section. Depending on the application, cross section and pipes path may have a more complex shape that could induce flow non-uniformity.

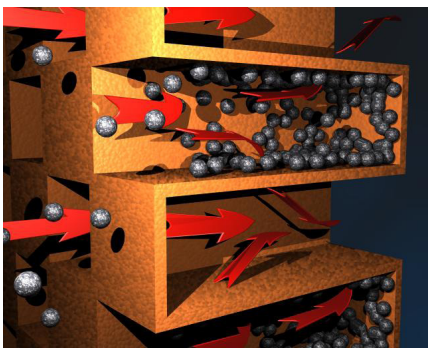

Figure 1.2: Schematic of a wallflow DPF principle. Exhaust gas enters open channels and it is forced to pass through porous walls, that intercept and collect particualte matter.

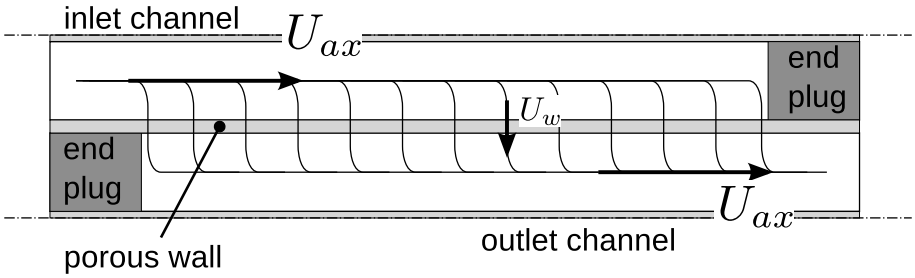

Figure 1.3: 2D sketch of a DPF channel pair. Honeycomb monolith is generated by extrusion and channel terminations are closed by inserting "end plugs". Engine side is on the left of the figure.

Working principle is represented in figs. 1.2 and 1.3. Exhaust gas enters the open channels on one side and it is forced to pass through the porous wall, that collects soot particles and removes them from the flow. Collected particles either deposites on porous walls surface or are trapped inside the medium: in both cases wall permeability decreases. As a consequence, an increase in both collection efficiency and hydrodynamic resistance is expected. When pressure difference between filter ends reaches a threshold value, deposited soot is burnt during the *regeneration phase*.

Regeneration is the most important issue with diesel traps, and it is strictly related to the hydrodynamic behaviour of the filter. In particular, longer regeneration cycles (and thus a better regeneration efficiency) would be ensured by a uniform particle distribution in the filter cross-section, that, in turn, is dependent on the flow uniformity at the filter inlet. In addition, an uneven distribution of soot particle inside the trap would lead to strong temperature gradients during regeneration, possibly leading to thermal cracks in the monolith and component failure.

1.1 Statement of the problem

In the field of DPF modeling, three main problem categories can be sorted out:

1. Fluid-dynamics of the gas flowing into the filter;
2. Soot transport within the gas and deposition onto the porous surfaces, including changes in filtrating properties and hydrodynamic resistance of the substrate;
3. Filter regeneration by combustion of the trapped soot, as a consequence of either spontaneous catalyzed reactions or external intervention.

In turn, the above-listed phenomena involve a quantity of sub-aspects, each one with its peculiar issues about physics comprehension and modeling:

- Hydrodynamics of compressible fluids
- Porous media
- Turbulence
- Multiphase flows (gas/soot particles)
- Particle deposition
- Filtration
- Surface reactions
- Conjugate heat transfer

Finally, all of the above phenomena are coupled each other, so that a complete and detailed modeling can result in a very large and stiff system of PDEs. It would be worthless and unfeasible to develop and implement such a comprehensive model, if not impossible at all. Under appropriate hypotheses, however, it is possible to decouple some parts of the problem from the rest. By doing so, the implementation becomes possible, and the whole of the phenomena can be studied as separate problems.

1.2 Scope of this work

The scope of this work is the definition and implementation of an original modeling strategy to reproduce the dynamic behaviour of DPFs during the loading stage. The proposed model should be able to account for all the main fluid-dynamic phenomena that occurs during this step, at different levels of detail.

On a global scale ($\mathcal{O}(10^{-1})$ m), the flow field inside inlet and outlet cone, that is strongly influenced by the presence of the filter, must be accurately solved to determine the flow distribution on the filter frontal section. In those regions, flow regime is always turbulent and it might show separation or recirculation regions.

On a smaller scale, corresponding to DPF channels ($\mathcal{O}(10^{-3})$ m), gas flow and soot deposition must be predicted to account for changes in DPF properties with filter loading. Moreover, distribution of PM into the filter is responsible for temperature gradients during regeneration, so that the proposed model could serve as a preparatory stage for a successive work that takes into account chemical reactions and heat transfer.

The first part of this thesis work is organized as follows. In this chapter, after a brief review of state-of-art in DPF modeling (section 1.3), the following section 1.4) will be devoted to explain an original approach for DPF hydrodynamics modeling. In the next one (1.5), a transport and deposition model for solid particles will be added to the hydrodynamics

solver to account for filter loading. Finally, extensive validation and discussion are reported in chapter 2.

1.3 State of art in DPF modeling

Prediction of pressure drop and velocity fields of Diesel Particulate Filters is a challenging problem in the field of numerical modeling. Several strategies have been developed along years for this purpose, each of them with a different degree of complexity, ranging from the first simplified analytical model to sophisticated multi-phase approach. In the followings, all strategy will be briefly presented, to highlight their strenghts and weaknesses, and to better understand the motivation of the original approach explained in the present thesis work.

1.3.1 Analytical approach

One of the first method for predicting pressure drop of a DPF is due to Konstandopoulos et al. [51]. This approach considers the filter as a standalone component and bulk gas velocity is assumed to be uniform across the whole monolith frontal area, so that only one channel pair is modeled. Inside the filter, velocity is decomposed into mean axial velocity u_i and wallflow velocity u_w (refer to Fig. 1.4).

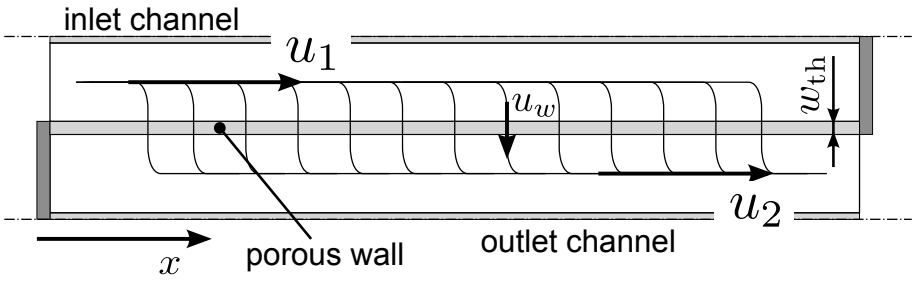

Figure 1.4: Channel-pair domain upon which the Konstandopoulos model is based. Three velocity variables are defined: u_1, u_2, and u_w.

The inlet-outlet channel pair is described by a system of ODE, namely (subscript 1 refers to inlet channel, while subscript 2 refers to outlet channel):

- Mass balance

$$\frac{d}{dx_1}\rho u_1 = -\frac{4}{a}\rho u_w \tag{1.1}$$

$$\frac{d}{dx_2}\rho u_2 = \frac{4}{a}\rho u_w \tag{1.2}$$

- Momentum balance

$$\frac{d}{dx}(\rho u_1^2) = -\frac{dP_1}{dx_1} - \frac{4}{a}\tau_1 \tag{1.3}$$

$$\frac{d}{dx}(\rho u_2^2) = -\frac{dP_2}{dx_2} - \frac{4}{a}\tau_2 \tag{1.4}$$

- Darcy law

$$P_1 - P_2 = \frac{\mu}{k} u_w \mathrm{w}_{por} \tag{1.5}$$

Pressure drop is calculated as $P_1(0) - P_2(L) = P_1(0) - P_{amb}$ and it is given by the sum of Darcy loss and friction between gas and channel.

The model has been afterwards extended to include Forchheimer inertial loss and contraction and expansion of the gas flow at the channel inlet and outlet sections [53] The final expression is given in Eq. (1.6) below. The first term of the summation refers to frictional losses and the second one refers to inertial losses:

$$\Delta P = \frac{\mu Q}{2V_{trap}}\left(a + \mathrm{w}_{por}\right)^2 \left[\frac{\mathrm{w}_{por}}{ka} + \frac{8FL^2}{3a^4}\right] + \frac{\rho Q^2\left(a + \mathrm{w}_{por}\right)^4}{V_{trap}^2 a^2}\left[\frac{\beta \mathrm{w}_{por}}{4} + 2\zeta\left(\frac{L}{a}\right)^2\right] \tag{1.6}$$

In the above expression, Q is the bulk mass flow rate, V_{trap} is the filter geometric volume ($V_{trap} = \pi/4 D^2 L$), L is the filter overall length, a is channel width and w_{por} porous wall thickness, $F = 28.454$ is a friction coefficient, k and β are, respectively, Darcy and Forchheimer constants, and $\zeta \approx 0.82$ is a loss coefficient for gas contraction and expansion.

Porous wall permeability appearing in the Darcy term, and Forchheimer coefficient (β), are evaluated by comparing the filtrating layer to a packed bed of spheres, namely (1.7):

$$k = \frac{\varepsilon^3}{150(1-\varepsilon)^2} d_c^2 \qquad\qquad \beta = \frac{1.75\,(1-\varepsilon)}{d_c\,\varepsilon^3} \tag{1.7}$$

where ε is the mean porosity and d_c the mean diameter of spherical particles.

Konstandopoulos' model has proven to predict with good accuracy the pressure drop of a clean trap and it has been extensively validated [52].

A possible shortcoming of this model lies in its lack of detail. In fact, it does not take into account, for example, the presence of channel end-plugs or an uneven distribution of gas velocity across the filter cross section. Nonetheless, its simplicity makes it a good model for fast evaluation of pressure drop in the early stages of a project or to simulate DPF behaviour within the vehicle Electronic Control Unit [63]. Still, the filter needs to be fully characterized on its flow resistance descriptors. Some guidelines about reccomended experimental practice can be found in literature [50].

This approach can be extended to take into account soot deposition, filtration process and regeneration [41] for studying the whole lifecycle of Diesel particulate traps, with the same advantages and drawbacks already mentioned.

1.3.2 Porous volume with directional permeability

Multi-dimensional simulation of DPFs is not an easy task due to the complexity of the geometry, the difference in magnitude of the lengthscales involved and the great number of physical processes to take into account. Among them, flow through porous media is probably the most challenging problem for numerical solvers [4].

The simplest strategy to simulate a wallflow monolith is to model it as a porous region with anisotropic resistance. Presence of the porous medium is taken into account by the solver by means of an additional source term in the momentum equation:

$$\nabla P_{por} = \mu \boldsymbol{D} \mathbf{U} \tag{1.8}$$

where $\boldsymbol{D} = 1/k_{ij}$ is a tensor defining the porous resistance along the coordinate directions. Most CFD codes [62, 27, 12] include this feature that is used for simulating flow through porous zones.

Components of k_{ij} can be tuned to simulate the behaviour of a real DPF, namely, using a medium to high permeability along mean flow direction and low permeability across transverse directions [94]. The only advantages of this approach are its great simplicity and its low additional computational cost. For the rest, it is questionable how well can the directional porosity approach reproduce the real behaviour of a DPF with respect of the outer flow and, anyway, up to six parameters are to be tuned. Nonetheless, it is still a rather widely used approach for applied studies [31].

1.3.3 Direct simulation of the porous wall

Porous medium approach, on the other hand, can be also used to directly model single porous walls. Such an approach allows for a detailed reproduction of the channel geometry up to a sub-millimeter scale and physical consistency is very high [65]. Direct simulation of a channel pair is straightforward to implement and it is possible to simulate soot particles by means of a lagrangian approach to perform high accuracy fundamental studies [74, 73].

On the other hand, porous walls would be composed of a great number of very small cells, leading to an high computational cost and, in addition, to a low timestep that would be necessary to comply with the CFL criterion. For these reasons, in addition with the intrinsic complexity of the geometry to be reproduced, simulation of the whole trap is precluded due to the long time required to generate the mesh and to carry out the computations.

In the end, direct simulation of the porous wall is an interesting approach by the point of view of fundamental studies, but with little or no interest for practical applications.

1.3.4 Co-simulation

Co-simulation methods consist in using two different solvers: a standard CFD one for the external ducts and a dedicated one-dimensional solver based on the method explained in section 1.3.1 for the DPF region [36]. Often, a set of 'representative channels' is taken from the cross section of the filter (e.g. on the axis, on the external circumference, and in between) to partially account for flow non-uniformity [17].

Like most co-simulation methods, this approach is inherently less efficient and its implementation is quite complex because of the intrinsic decoupling of the domains. However, due to consolidated validation of the one-dimensional model, it is the preferred choice of many commercial CFD softwares [32].

1.3.5 Coupled domains

An interesting strategy has been proposed by Hinterberger et al. [39] on the basis of coupled domains. Filter monolith is represented by two fluid zones, coupled each other by an interface that represents the filtrating surfaces. Axial flow fields are modeled using anisotropic porosities, whereas mass sources and sinks within the porosities address the wall filtration mass flux. Optionally, a third domain representing solid walls between filter segments can be added to study heat transfer between fluid and monolith during the regeneration phase.

All domains are intrinsically coupled via their interface and are considered as a whole fluid region by the CFD solver. This approach is much more efficient than co-simulations and allows for a greater level of detail with respect to use bulk porous blocks.

1.4 A new approach to DPF modeling

The most straightforward way to model porous walls of DPF would be to consider them as fluid zones with porous resistance term (a number of works exist in this field. See e.g. [65]). Such an approach allows for great accuracy since is the closest to the real world, but it poses some issues by the point of view of practical application. Being the usual thickness of a porous wall less than 1 mm (more often, between 0.5 and 0.1 mm), and due to the need of having at least three cells in the wall-normal direction, porous cell size would turn to be very small compared to other region of the domain. As a consequence, the number of total cells increases by a significan amount and, in addition, a very low timestep is required to comply with the CFL criterion $u\Delta t/\Delta x < 1$ [26].

Moreover, when moving from the global scale (inlet/outlet cones) to channel scale, characteristic lengths vary a lot and so the cell size. Thus, a low timestep is anyway required to

solve the whole flow, whereas for the largest part of the domain less stringent requirements have to be met.

Computational cost is not the only drawback of such an approach. Mesh generation of a complex shape like a detailed honeycomb monolith can be very time consuming as number of channel increases. So, an automatic mesh generation algorithm would be of great convenience.

The former problem (porous cells size) could be overcome by considerating that thickness of porous walls is negligible if compared to their length. Thus, it is possible to model porous walls as zero-thickness surfaces with a flow resistance term. This is the base of the porous surface approach that will be outlined in section 1.4.2.1.

The latter issue (scale difference and mesh generation), in turn, has been dealt by considering each channel as a 1D array of cells, in which the cell-centered velocity represents the mean channel velocity and cell-face fluxes the wallflow velocity. Such a simplifying approach will be explained in section 1.4.2.2.

1.4.1 Physics overview

The mean flow inside a DPF channels pair can be regarded as constituted by two components, represented in Fig. 1.5: the mean axial velocity U_{ax} and the wallflow (or transverse) velocity U_w. This decomposition is the base of almost all zero-D and one-D fluid-dynamic models of DPF that have been explained in chapter 1.3, e.g. [51, 54, 41], and it has been proven to be effective when studying the hydrodynamics of the trap.

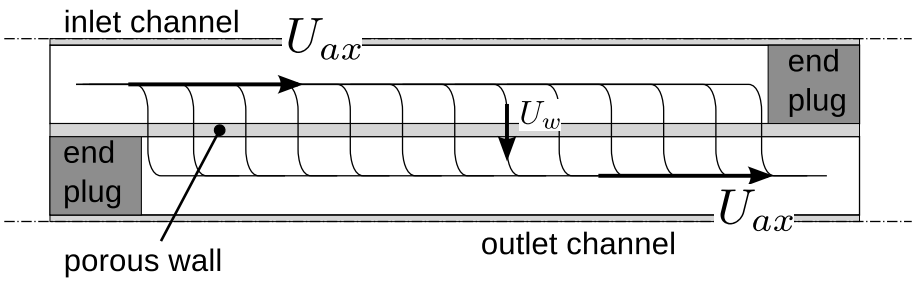

Figure 1.5: Mean velocity can be decomposed into axial component (centered on the channel axis) and transverse component (normal to porous wall).

The axial component gradually decreases in inlet channels and, conversely, it gradually increases in outlet channels as mass is transferred through the porous wall. Friction between gas and solid walls can be estimated with the following considerations. Let C_f be the wall

friction coefficient [26]:

$$\boldsymbol{\tau} = \frac{1}{2} C_f \rho \mathbf{u}^2 \tag{1.9}$$

that is, obviously, a function of Reynolds number. For pipe laminar flow, that is the prevalent regime in filter channels, fritcion factor is obtained as:

$$C_{f,0} = 64/\mathrm{Re} \tag{1.10}$$

If walls are porous, there is momentum suction or injection through the solid boundaries, so the aforementioned expression has to be modified as follows [70, 47]:

$$C_{f,s} = F_s(\mathrm{Re_w}) C_{f,0} \tag{1.11}$$

$$C_{f,i} = F_i(\mathrm{Re_w}) C_{f,0} \tag{1.12}$$

where $\mathrm{Re_w}$ is the wall Reynolds number (D_h is channel hydraulic diameter):

$$\mathrm{Re_w} = \frac{U_w D_h}{\nu} \tag{1.13}$$

A semi-empirical correlation for $F(\mathrm{Re_w})$ was found by Raithby [68]:

$$F(\mathrm{Re_w}) = \frac{1}{16}\left[0.0481 + \frac{0.0494}{(\mathrm{Re_w} + 4.7)^{0.8}}\right]^{-1} \tag{1.14}$$

where suction and injection are discriminated by the sign of U_w (suction has $U_w < 0$). However, for usual values of $\mathrm{Re_w}$ encountered in practice, variation of $F(\mathrm{Re_w})$ are under 10%, so Konstandopoulos [51] suggests that mass suction/injection can be neglected and the usual expression of C_f for fully-developed pipe flow can be adopted.

Responsible of mass exchange is the wall-flow velocity (or transverse velocity), that usually assumes an U-shaped distribution with a minimum located at about mid-length along the wall (skewness of curve $U_W(x)$ is determined by filter permeability and inlet velocity). Fluid motion through porous walls is governed by Darcy's law, that, in general form, reads:

$$\nabla P = \frac{\mathbf{u}\mu}{\boldsymbol{k}_{\mathbf{por}}} + \mu \nabla^2 \mathbf{u} \tag{1.15}$$

DPF walls, however, are very thin compared to their length, so that Darcy velocity can be considered as composed by the wallflow component alone. Written in one dimension, Eq. (1.15) is simplified as:

$$\frac{\mathrm{d}P(x)}{\mathrm{d}w} = \frac{U_w \mu \mathrm{d}w}{k_{\mathrm{por}}} \mathrm{d}w \tag{1.16}$$

where w is the wall-normal direction and k_{por} is now a scalar.

Darcy law is suited for calculating local pressure drop, only if the following condition on porous Reynolds wall is met [9]:

$$\mathrm{Re_p} = \frac{U_i \sqrt{k_{\mathrm{por}}}}{\nu} \ll 1 \tag{1.17}$$

Again, Konstandopoulos [51] shows that average porous Reynolds number is around 0.13, and that small regions where this value is exceeded have a negligible influence on the whole flow.

1.4.2 Porous surface approach

1.4.2.1 Porous wall as a surface

As anticipated at the beginning of the present section, porous wall thickness is very small compared to other dimensions (channel side and length). On the other hand, the direction of the gas crossing the porous layer can be considered orthogonal to the filtrating surface in almost every point and, due to the small thickness of the wall compared with the channel hydraulic diameter, there is no gas accumulation within the porous volume.

Therefore, it is possible to completely neglect the thickness of porous walls and consider them as ideal surfaces (membranes) that nonetheless offer a significant porous resistance to the flow. Darcy equation (1.16) is integrated over the wall thickness and gives:

$$\frac{\Delta P}{\Delta x} = \frac{1}{\Delta x} \frac{U_w \mu \mathrm{w}_{por}}{k_{\mathrm{por}}} \tag{1.18}$$

where w_{por} is the wall thickness and Δx the distance between cell centers of two adjacent control volumes. Either w_{por} and k_{por} are physical properties associated to porous surfaces, so they are inserted into the equations as cell face terms.

In fig. 1.6 the 'porous surface' approach is depicted, where a is the filter true channel width, w_{por} is the porous wall thickness and $a' = a + \mathrm{w}_{por}$ is the channel transverse pitch and the channel width of the modeled monolith.

It must be however noted that, as a consequence of neglecting the wall thickness, the total Open Frontal Area of the filter will be different in the modeled geometry with respect to the real one, thus affecting the gas velocity entering the filter. Nevertheless, it is possible to apply a correction term to the momentum equation to take into account such a side-effect.

1.4.2.2 Filter channel as 1D array

When studying the global behaviour of a particulate trap, the decomposed velocity field (described in section 1.4.1), together with pressure, are enough to describe the global flow inside

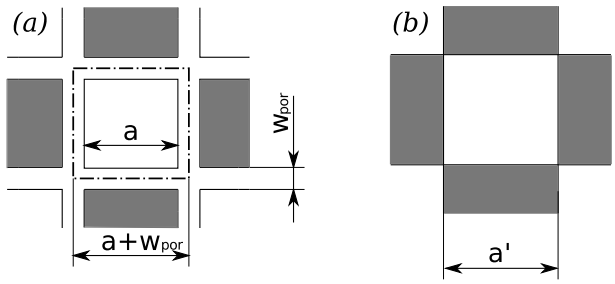

Figure 1.6: Simplification of porous walls as ideal surfaces. (a): Original geometry (gray represents closed channel ends) with a = channel width. (b) simplified model: porous wall thickness w_{por} is neglected in the geometrical model and channel width is increased to $a' = a + w_{por}$

the monolith. Thus, it is possible to neglect any transverse velocity variation *within the single channel* and consider each channel as an array of control volumes. Likewise, the monolith can be regarded as a matrix of 1D channels divided by porous surfaces, which offer a significant flow resistance both in the normal direction (porous term) and in the streamwise direction (friction). Channel end faces are alternatively set to open/closed following a chessboard pattern to replicate the actual filter frontal surface (cf. fig. 1.8). End plugs are correctly accounted for by adding a small length to each channel, whose cells have non-permeable walls.

Since the porous surfaces are just sources of surface stresses (and not actual solid walls), the fluid-dynamic solver 'sees' only one fluid domain. Surface forces are applied on those cell faces classified as 'porous', whose side is equal to the channel pitch a' of fig. 1.6. Thus, each cell in the monolith zone will have two to four 'porous' faces, one or two 'fluid' faces (with no stress applied) and could have also some 'closed' (wall) faces. The resulting mesh is represented in figs. 1.7 and 1.8.

Using only one cell per channel width, allows for having the same (approximate) cell size both in the external flow and in the filter region. Clear numerical benefits arise from such a simplification.

1.4.3 Modeling the source terms

The porous surface introduced in the previous section comes out as an interface between distinct volumes. Hence, it has to belong to some set of cell faces, since in the FV framework all quantities are continuous within the same cell. It follows that the indefinite momentum equation (15) is not valid anymore, since the continuum hypothesis (upon which the Gauss theorem is based) no longer holds. However, the momentum equation can be written for a

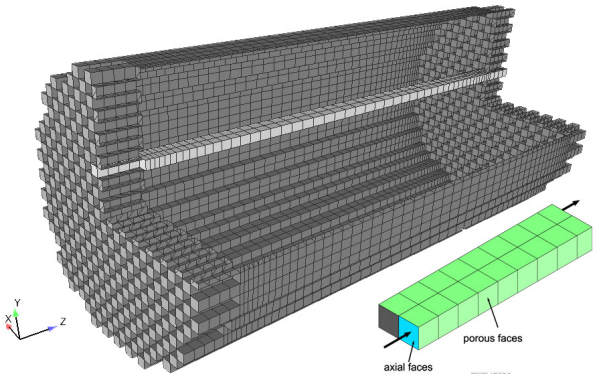

Figure 1.7: Global view of a full-scale model of DPF. Each channel is modeled by a 1D array of cells (bottom-right corner of the figure). Note that only one channel is represented in the global view for clarity, but there is one per each cell on the frontal face. Also, extensions of channels due to end-plugs are visible.

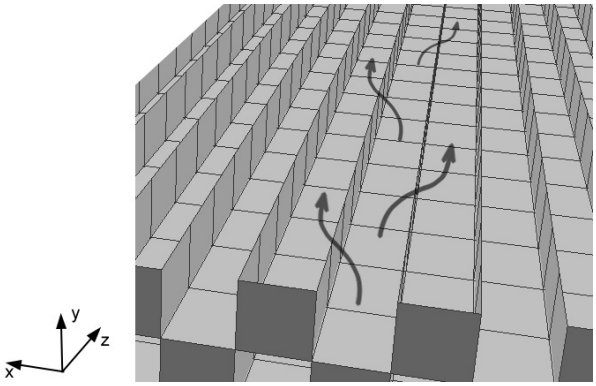

Figure 1.8: Close-up view of channel network inside the trap. Arrows represent exhaust gas path. Dark faces represent closed ends (wall), whereas light-coloured ones are porous faces.

finite control volume as usual:

$$\frac{\partial}{\partial t}\int_\Omega \rho\mathbf{U}\,\mathrm{d}\Omega+\int_\Omega \nabla\cdot(\rho\mathbf{UU})\,\mathrm{d}\Omega=-\int_\Omega \nabla p\,\mathrm{d}\Omega+\int_\Omega \nabla\cdot(\mu\boldsymbol{S})\,\mathrm{d}\Omega+\int_\Omega \rho\mathbf{b}\,\mathrm{d}\Omega+\int_S (D\,\mathbf{n})\,\mathrm{d}S \quad (1.19)$$

In the above equation (1.19), D represents the Darcy/Forchheimer resistance (multiplied by the unit area vector since it is always normal to the surface) which includes both viscous and inertial effects [53]:

$$D=-\frac{1}{a'}\left[\frac{\mu \mathrm{w}_{por}}{k_{\mathrm{por}}}u_w+\beta\rho \mathrm{w}_{por}u_w^2\right] \quad (1.20)$$

where k_{por} is the wall permeability, w_{por} its thickness, u_w is the wall-normal velocity and β is the Forchheimer coefficient. Obviously, the Darcy/Forchheimer term is defined only on boundaries classified as 'porous', otherwise, it can be supposed identically zero. When considering a cell belonging to the filter region, the surface integral of the Darcy/Forchheimer

term on the control volume is nearly zero, because the cell face areas on two opposing porous faces are the same and the corresponding wallflow velocities are very similar. As a consequence, because of the colocated arrangement of OpenFOAM, the effect on the global momentum balance would be negligible.

1.4.3.1 Variables arrangement

To overcome this problem, the pseudo-staggered approach [71] has been employed: momentum equation is not solved using the cell-centered velocity **U** but the face flux $\phi = \mathbf{U} \cdot \mathbf{S_f}$, and pressure gradient is computed at cell face instead than cell centers. Cell-centered velocity is regarded as a secondary variable, used only to compute some terms (like rate-of-strain tensor) and for postprocessing. The difference between the standard colocated approach and the pseudo-staggered arrangement is outlined in Fig. 1.9. Following the pseudo-staggered approach, porous resistance can be seen as a surface stress that counteracts the pressure gradient between two adjacent cells, Eq. (1.21):

$$\frac{1}{a'}\left(-\frac{\mu \mathrm{w}_{por}}{k_{\mathrm{por}}} u_w - \beta \rho \mathrm{w}_{por} u_w^2\right) = \frac{1}{a'}(p_2 - p_1) \tag{1.21}$$

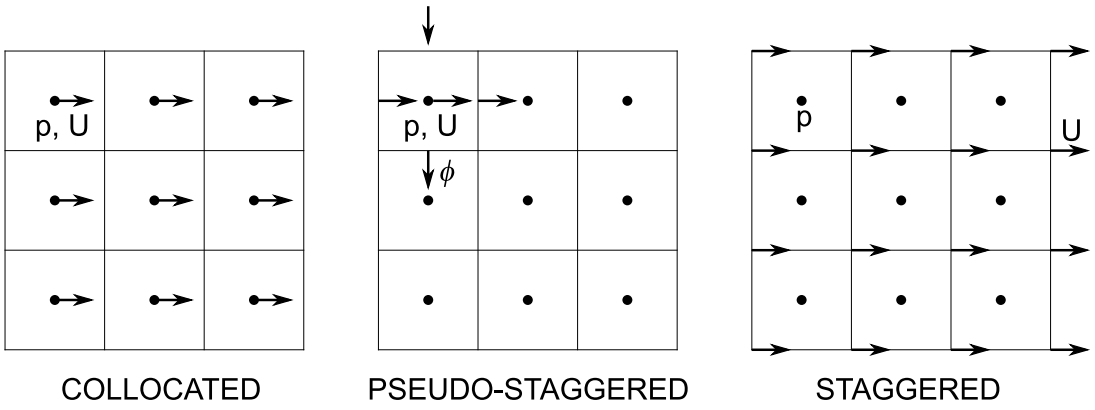

Figure 1.9: Representation of the pseudo-staggered variable arrangement. While the classic colocated approach (right) considers pressure and velocity both at the cell center, and the staggered approach puts velocity on nodes (left), the pseudo-staggered arrangement keeps pressure at velocity at cells center, but momentum is solved in the flux variable ϕ.

1.4.4 Solution procedure

Solution procedure for a pseudo-staggered arrangement is slightly different from the standard approach used by OpenFOAM, since all operators are designed for the colocated ap-

proach and it is not possible to treat implicitly the face flux ϕ. The SIMPLE algorithm outlined in section 4.2 needs to be adapted to the new situation.

The momentum predictor equation still needs to be written in colocated variables, for velocity in the convection and the diffusion terms has to be considered implicitly to build the system matrix. On the other hand, porous resistance has to be inserted as a force balance on the cell boundary and this is achieved via a *reconstruction* procedure:

$$\int_S (D\,\mathbf{n})\,\mathrm{d}S \approx \left[\sum_{f=1}^{n_f} \frac{\mathbf{S_f}^2}{\|\mathbf{S_f}\|}\right]^{-1} \sum_{f=1}^{n_f} \frac{\mathbf{S_f}}{\|\mathbf{S_f}\|} D \tag{1.22}$$

$$= \left[\sum_{f=1}^{n_f} \frac{\mathbf{S_f}^2}{\|\mathbf{S_f}\|}\right]^{-1} \sum_{f=1}^{n_f} \frac{\mathbf{S_f}}{\|\mathbf{S_f}\|} \frac{1}{a'} \left[-\frac{\mu \mathrm{w}_{por}}{k_{\mathrm{por}}} \frac{\phi}{\rho\|\mathbf{S_f}\|} - \beta\rho \mathrm{w}_{por}\left(\frac{\phi}{\rho\|\mathbf{S_f}\|}\right)^2\right] \tag{1.23}$$

where face-normal velocity is evaluated using the face flux: $u_w = \phi/(\rho\|\mathbf{S_f}\|)$. For simplicity, the reconstruction procedure will be denoted with symbol $\vec{\sum}$:

$$\int_S (D\,\mathbf{n})\,\mathrm{d}S \approx \vec{\sum} \frac{1}{a'} \left[-\frac{\mu \mathrm{w}_{por}}{k_{\mathrm{por}}} \frac{\phi}{\rho\|\mathbf{S_f}\|} - \beta\rho \mathrm{w}_{por}\left(\frac{\phi}{\rho\|\mathbf{S_f}\|}\right)^2\right] \tag{1.24}$$

Then, the standard predictor-corrector loop for a pseudo-staggered arrangement follows:

1. Calculation of predicted velocities using neighbouring cells coefficients:

$$\mathbf{U}^* = \frac{\mathscr{A}_H}{\mathscr{A}_D} \tag{1.25}$$

2. Calculation of predicted fluxes using $\mathbf{U}^*$:

$$\phi^* = \rho_f \mathbf{U}_f^* \cdot \mathbf{S_f} \tag{1.26}$$

3. Correction of fluxes with porous resistance:

$$\phi^{**} = \phi^* + \frac{1}{\mathscr{A}_{D,f}} \frac{1}{a'} \left[-\frac{\mu_f \mathrm{w}_{por}}{k_{\mathrm{por}}} \frac{\phi^*}{\rho_f\|\mathbf{S_f}\|} - \beta\rho \mathrm{w}_{por}\left(\frac{\phi^*}{\rho_f\|\mathbf{S_f}\|}\right)^2\right] \tag{1.27}$$

4. Solution of Poisson equation for pressure:

$$\nabla \cdot \left(\frac{1}{\mathscr{A}_{D,f}} \nabla p^{n+1}\right) - \nabla \cdot \phi^{**} = 0 \tag{1.28}$$

5. Update fluxes with corrected pressure:

$$\phi^{***} = \phi^{**} - \frac{1}{\mathscr{A}_{D,f}} \nabla_f^{\perp} p^{n+1} \tag{1.29}$$

6. Correct velocity with updated fluxes:

$$\mathbf{U}^{n+1} = \mathbf{U}^* + \vec{\sum} \frac{\mathscr{A}_{D,f}}{\rho_f} \left(\phi^{***} - \phi^*\right) \tag{1.30}$$

1.4.4.1 Remarks on the implicit porous term modeling

Since the Darcy/Forchheimer term (1.22) is evaluated using the predicted fluxes ϕ^*, Eq. (1.28) contains a very large explicit source term, that causes severe stability problems, expecially for low permeabilities (high resistance). Therefore, very low under-relaxation factors (or very small timesteps for transient cases) are required to achieve stability: this poses a great limit on the size of the simulation, since for large domains (or long simulation time) the computational cost may become unaccettable.

On the other hand, were it possible to insert the source term implicitly, i.e., with the flux computed with the present-timestep velocity instead than the old value, stability of the system would improve by a significant amount. During this study, some attempts have been made in this direction and a possible solution is proposed here.

The discretized momentum equation reads:

$$\mathscr{A}_P \mathbf{u_P} = \mathscr{A}_H - \nabla p - \vec{\sum} C_D \mathbf{u_f} \tag{1.31}$$

where the Darcy/Forchheimer term has been written as a constant coefficient C_D multiplied by the face velocity $\mathbf{u_f}$. The same expression may be written in terms of face-centered velocities:

$$\mathscr{A}_{D,f} \mathbf{u_f} = \mathscr{A}_{H,f} - \nabla_f^{\perp} p - C_D \mathbf{u_f} \tag{1.32}$$

so that it is possible to isolate the variable $\mathbf{u_f}$:

$$\mathbf{u_f}\left(1 - \frac{C_D}{\mathscr{A}_{D,f}}\right) = \frac{\mathscr{A}_{H,f}}{\mathscr{A}_{D,f}} - \frac{1}{\mathscr{A}_{D,f}} \nabla_f^{\perp} p \tag{1.33}$$

$$\mathbf{u_f} = \frac{\mathscr{A}_{H,f}}{\mathscr{A}_{D,f}} \left(1 - \frac{C_D}{\mathscr{A}_{D,f}}\right)^{-1} - \frac{1}{\mathscr{A}_{D,f}} \left(1 - \frac{C_D}{\mathscr{A}_{D,f}}\right)^{-1} \nabla_f^{\perp} p \tag{1.34}$$

In a similar way as the classic segregated methodology, the Poisson equation can be written by taking the divergence of Eq. (1.34):

$$\nabla \cdot \left(\frac{1}{\tilde{\mathscr{A}}_{D,f}} \nabla p^{n+1} \right) - \nabla \cdot \tilde{\phi}^* = 0 \tag{1.35}$$

where:

$$\tilde{\phi}^* = \phi^* \left(1 - \frac{C_D}{\mathscr{A}_{D,f}}\right)^{-1} \quad \text{and} \quad \tilde{\mathscr{A}}_{D,f} = \mathscr{A}_{D,f} \left(1 - \frac{C_D}{\mathscr{A}_{D,f}}\right) \tag{1.36}$$

The above formulation (1.35) can be regarded as implicit since the porous resistance term modifies the system matrix of coefficients. This method has been proven to be far more stable than the explicit one, allowing for the use of quite large timesteps, irrespective of the magnitude of the Darcy/Forchheimer coefficient. However, it must be noted that formulation of the implicit source term in Eq. (1.31) is inexact: the Darcy/Forchheimer coefficient

must be multiplied by the *face-normal* component of the velocity and not by the whole vector. Unfortunately, fixing this issue is not straightforward at all, since the Darcy/Forchheimer term should be dot-multiplied by the unit area vector:

$$D = C_D \mathbf{u_f} \cdot \mathbf{n} \tag{1.37}$$

and, as a consequence, coefficients of the Poisson equation would turn to be vectors instead than scalars. Such a situation is not permitted by the standard linear solvers of OpenFOAM.

1.4.4.2 Axial friction

Friction between gas and porous walls can be accounted for by the source term introduced in section 1.4.1 [51, 41], since each cell is surrounded by 4 solid walls.

The friction sink term in the momentum equation reads:

$$Q_F = F\frac{\mu u_{ax}}{a^2} \tag{1.38}$$

where the F constant assumes the constant value of 28.454. Q_F is continuous within the volume, thus it can be inserted as a body force source proportional to the cell-centered velocity; however, since only the axial component of the velocity is considered, an explicit treatment of the source term must be used:

$$Q_{F,P}^{m-1} = -\frac{F\mu}{a'^2} \cdot \mathbf{u}_P^{m-1} \cdot [\mathbf{i}_3 \cdot \mathbf{i}_3{}^T] \tag{1.39}$$

where $\mathbf{i}_3$ is the unit vector oriented along the axial direction of the filter and a' is the filter channel width.

1.4.4.3 Open frontal area correction

Since the porous face approach neglected the thickness of filtrating walls, the total Open Frontal Area (OFA) of the filter is overestimated. As a consequence, for the same mass flow rate, all velocities are underestimated. This leads to an underestimation of the pressure drop as well, since all sink terms are proportional to velocity. The aim of this section is to correlate the underestimation in the predictions of pressure drop to the discrepancy of OFA caused by filter schematization, in order to apply a correction in the NS equations.

The average velocity of the gas entering a single channel is:

$$u_1 = \frac{\dot{V}}{n_{chan} \cdot a^2} \tag{1.40}$$

and, for a given flow rate $\dot{V}$, different grids lead to different velocities at the inlet section of the open channels in the filter cross section. Momentum equations for DPF channels in the

two different grids may be written for grid 1 (width=a, Fig. 1.6-a) as:

$$\nabla \cdot (\rho_1 \mathbf{u_1} \cdot \mathbf{u_1}) = -\nabla p + \nabla \cdot \sigma + \mathbf{Q} \tag{1.41}$$

and for grid 2 (width=a+w, Fig. 1.6-b):

$$\nabla \cdot (\rho_2 \mathbf{u_2} \cdot \mathbf{u_2}) = -\nabla p' + \nabla \cdot \sigma' + \mathbf{Q}' \tag{1.42}$$

The difference between Eq. (1.41) and Eq. (1.42) is as follows:

$$\nabla \cdot \left[\rho \left(\mathbf{u_1} \cdot \mathbf{u_1} - \mathbf{u_2} \cdot \mathbf{u_2}\right)\right] = -\nabla (p - p') \tag{1.43}$$

where differences in stress tensors and sink terms have been neglected.

In a FV approach convective terms are integrated as follows:

$$\begin{aligned} \int_V \nabla \cdot (\rho \mathbf{u} \cdot \mathbf{u}) dV &= \int_S d\mathbf{S} \cdot (\rho \mathbf{u} \cdot \mathbf{u}) = \\ &= \sum_f \mathbf{S_f} \cdot (\rho \mathbf{u} \cdot \mathbf{u}) = \\ &= \sum_f \mathbf{u} \cdot \phi \mathbf{n_f} \end{aligned} \tag{1.44}$$

Hence, Eq. (1.43) can be written in the following form:

$$\sum_f \mathbf{u_1}_f \cdot \phi_1 \mathbf{n_f} - \sum_f \mathbf{u_2}_f \cdot \phi_2 \mathbf{n_f} = -\nabla (\Delta p) \tag{1.45}$$

where u_{1f} and u_{2f} are flow velocities defined over the cell face center in grid 1 and 2 of Fig. 1.6 respectively.

Under the hyphotesis that gas density ρ does not vary significantly in the two cases, to enforce the equivalence between fluxes over the channel cell faces of the two different grids ($\phi_1 = \phi_2$), one has:

1. for “axial” faces:

$$\mathbf{u_1}_f = \eta^2 \, \mathbf{u_2}_f \tag{1.46}$$

2. for “porous” faces

$$\mathbf{u_1}_f = \eta \, \mathbf{u_2}_f \tag{1.47}$$

where η is the width ratio and it is defined as:

$$\eta = \frac{a + w}{a} \tag{1.48}$$

Finally, Eq. (1.45) may be written as:

$$\nabla (\Delta p) = -\sum_f (C_f - 1) \mathbf{u_2}_f \cdot \phi \mathbf{n_f} = \mathbf{C} \tag{1.49}$$

where C_f is equal to η^2 or to η for axial or porous faces respectively.

1.4.5 Turbulence modeling

Last issue to be covered by hydrodynamics modeling is the problem of turbulence. The first consideration to be made is that, generally speaking, all quantities of interest for a DPF study are steady or slowly varying with time, so that the flow structures in the inlet and outlet cones of the filter can be successfully modeled using a RANS/URANS approach. On the other hand, flow model inside the monolith channels is one-dimensional, so fluid-dynamic losses are taken into account by an appropriate resistance factor and no turbulence modeling is needed inside the filter.

One of the most problematic points concerning classic RANS models is that they are generally unable to catch turbulence intermittency, so an appropriate treatment is needed when switching from turbulent to laminar regions, that was achieved by modifying the original $k-\varepsilon$ and $k-\omega$ RANS models.

According to the Boussinesq hypothesis, the Reynolds stress tensor can be calculated as:

$$\tau_{ij} - \frac{1}{3}\tau_{kk} = -2\mu_t S_{ij} \tag{1.50}$$

where S_{ij} represents the rate-of-deformation tensor: $S_{ij} = 1/2(\partial U_j/\partial x_i + \partial U_i/\partial x_j)$. Then, the turbulent viscosity μ_t can be obtained as a function of the turbulent kinetic energy:

$$\mu_t = \rho C_k \frac{k^2}{\varepsilon} \qquad (k-\varepsilon \text{ family}) \tag{1.51}$$

$$\mu_t = \rho \frac{k}{\omega} \qquad (k-\omega \text{ family}) \tag{1.52}$$

Thus, to deactivate the chosen model in the monolith, the turbulent kinetic energy k has been artificially forced to zero in such a region to account for both the lack of turbulence inside the filter and the dissipation of the existing one when the gas passes through the monolith.

The consistency and robustness of the solution are not invalidated by this simple procedure as long as an upwind-biased scheme is used in the conservation equation for k, that is anyhow required to mantain boundedness of the solution.

1.4.6 Mesh generation strategies

Last point concerning hydrodynamics modeling is mesh generation strategy that has to be adopted when using a porous face approach. We recall here that each channel has to be represented by a 1D array of FV cells, each one as wide as the real monolith channel pitch (Fig. 1.6). Secondly, all channel ends present an alternate chessboard pattern of open/closed faces, that have to be imposed as boundary conditions; moreover, open ends have to be

prolonged by a certain amount to represent the presence of an 'end plug' on the adjoining closed ends. Finally, the monolith region has to be connected with inlet and outlet cones, that may have complex meshes since they have to represent the actual exhaust system where the filter is inserted.

To reduce the time required for preprocessing, the following semi-automatic procedure has been estabilished to generate the complete FV mesh for CFD simulaitions:

1. The raw filter region mesh is generated by extruding a 2D scketch representing the frontal area of the filter. Each channel is represented by a square cell in the 2D domain (Fig. 1.10).

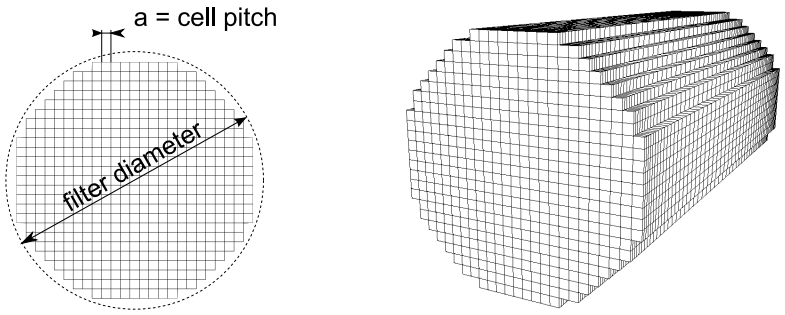

Figure 1.10: Mesh generation, first step: monolith extrusion from a 2D sketch of the frontal section

2. Front and rear faces are imposed a chessboard pattern of open/closed cells by an automatic algorithm (Fig. 1.11)

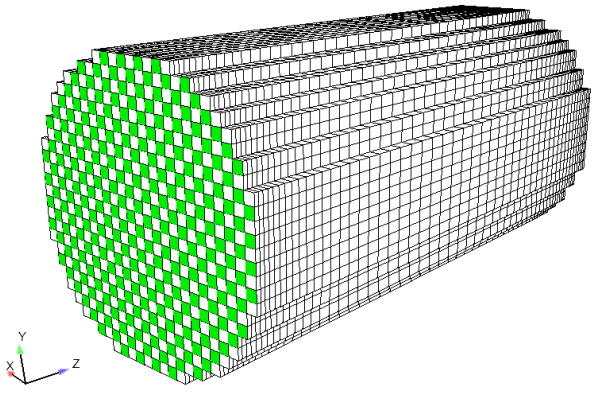

Figure 1.11: Mesh generation, second step: automatic setup of open-closed ends

3. Open-ends are pinpointed and extruded by a certain amount (given by filter specifications) to take into account the presence of the end-plugs (Fig. 1.12). Plug sides are by default set as 'walls'

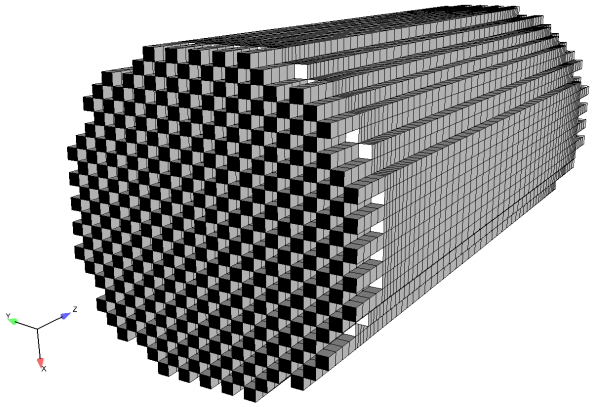

Figure 1.12: Mesh generation, third step: extrusion of additional length corresponding to end-plugs

4. Mesh of inlet and outlet pipe can be generated with any method, paying particular attention to quality parameters on the matching interface (Fig. 1.13).

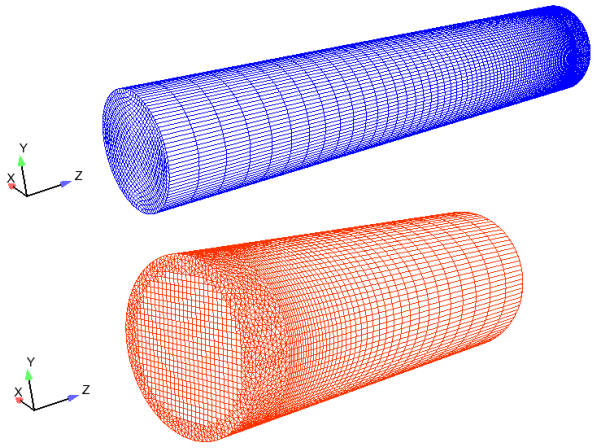

Figure 1.13: Mesh generation, fourth step: creation of inlet/outlet pipes mesh

5. All pieces (monolith, plugs, inlet and outlet) are stitched together to obtain a unique fluid domain (Fig. 1.14).

6. Porous faces are automatically identified given filter main axis and start/end coordinates (Fig. 1.15).

The above procedure can be performed in nearly automatic fashion with the use of appropriate shell script, obviously with the exceptions of inlet/outlet cones that are strongly case-dependent.

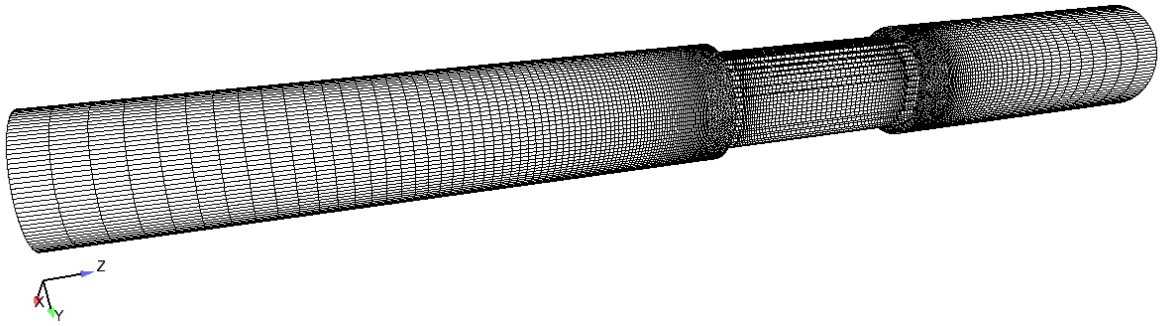

Figure 1.14: Mesh generation, fifth step: final assembling

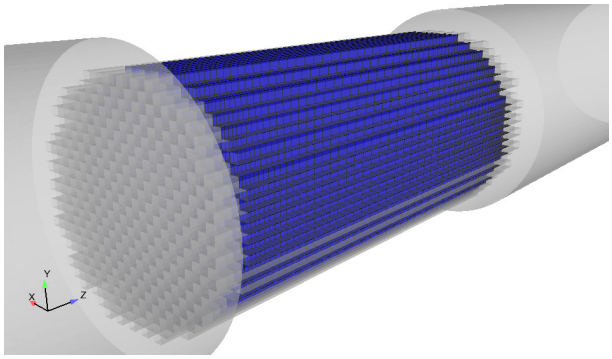

Figure 1.15: Mesh generation, sixth step: porous faces setup

1.5 Soot transport and deposition

The modeling approach explained in the previous chapter assumes the fluid is a monophase gas, thus the classic compressible Navier-Stokes equations are employed to describe the flow. However, soot particles produced during the fuel combustion process in a Diesel engine are convected by the exhaust gas flow into the filter, thus a multiphase flow has to be studied.

1.5.1 Soot particles modeling

Modeling of multiphase disperse flow can be carried out by two opposite philosophies: lagrangian or scalar. In the lagrangian approach the flow is considered as composed by two phases: carrier gas and solid particles. Particles are grouped into 'parcels' with the same physical properties (e.g. diameter, density) and motion equation is solved for each parcel, taking into account interactions between particle themselves and coupling between particles and fluid. Lagrangian approach is very fundamental and accurate, but it requires a great computational expense on the simulation, especially if the number of parcels is high.

In the scalar approach, solid phase is considered as a chemical specie, which is convected

within the gas as a passive scalar. In this case, fluid flow is not influenced by the second phase and, on the other hand, soot and gas velocities are considered equal at every point. Obviously, such approximations are valid only for small and lightweight particles and low concentrations, for the Stokes number has to be lower than one by some order of magnitude. The scalar approach, however, is much more simplified with respect to the lagrangian one, and it involves a negligible computational effort, so it is very suitable for large simulations (in terms of both geometric and temporal length scales).

In the following section, the lagrangian approach will be briefly described and some results from a previous work will be presented. The purpose of that section is to evaluate the lagrangian approach for DPF modeling and check whether some simpler strategy might be applied. In particular, the Stokes number of particles will be monitored: in case it remains well below unity, a scalar approach can be used for soot modeling.

1.5.1.1 Lagrangian modeling

Governing equations Motion equation for a Lagrangian particle is:

$$\rho_p \frac{\pi d_p^3}{6} \frac{\partial \mathbf{V}}{\partial t} = \mathbf{F}(r, m) \tag{1.53}$$

where $\mathbf{V}$ is the absolute velocity of the particle (with diameter d_p and density ρ_p), and $\mathbf{F}$ is the total applied force [5]

$$\mathbf{F} = \frac{3}{8} \frac{\rho}{\rho_p} \frac{\|\mathbf{W}\|\mathbf{W}}{d_p/2} C_D + \mathbf{g} \tag{1.54}$$

where the drag coefficient C_D is defined as follows [3]:

$$C_D = \begin{cases} \dfrac{24}{\mathrm{Re}_d}\left(1 + \dfrac{1}{6}\mathrm{Re}_d^{2/3}\right) & \mathrm{Re}_d < 1000 \\ 0.424 & \mathrm{Re}_d > 1000 \end{cases} \tag{1.55}$$

with Re_d the particle Reynolds number:

$$\mathrm{Re}_d = \frac{2\rho\|\mathbf{W}\| r}{\mu_{\mathrm{air}}(T)} \tag{1.56}$$

and $\mathbf{W}$ the relative velocity between particle and gas:

$$\mathbf{W} = \mathbf{U} - \mathbf{V} \tag{1.57}$$

It is possible to improve Eq. (1.54) by taking into account the Stokes-Cunningham slip factor C_C, whereas the gravity $\mathbf{g}$ can be neglected due to the small (sub-micron) dimensions of the particles [3]:

$$\frac{d\mathbf{V}}{dt} = \frac{3\nu C_D \mathrm{Re}_p}{2d_p^2(2\rho_p/\rho + 1)C_C} \tag{1.58}$$

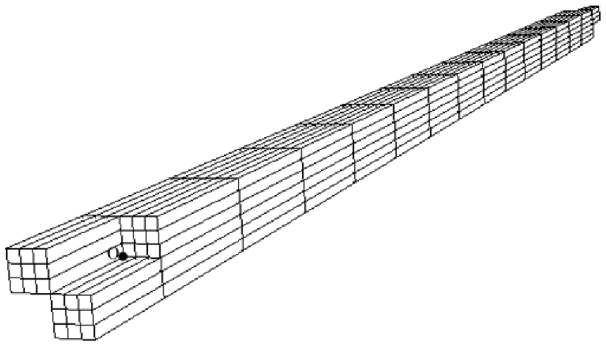

Figure 1.16: FV mesh of a channel quadruple to be used with soot lagrangian modeling.

C_C can be calculated as [73]:

$$C_C = 1 + 2\frac{\lambda}{d_p}\left(1.257 + 0.4\mathrm{e}^{-0.55\mathrm{Kn}}\right) \tag{1.59}$$

where λ is the mean molecular free path according to Sharipov [75]:

$$\lambda = \frac{\sqrt{\pi}\mu}{2p}\sqrt{2RT} \tag{1.60}$$

being R the gas constant.

The Brownian force can be evaluated as a gaussian random variable with mean value [15, 24]:

$$\bar{\mathbf{F}}_\mathbf{b} = \frac{216\nu \mathrm{k_B} * T}{\pi^2 \rho d_p^5 (\rho/\rho_p)^2 C_C} \tag{1.61}$$

with κ_B as the Boltzmann constant.

The lagrangian approach for modeling soot particles in Diesel particulate filters has been used by us as a preparatory stage for the full-scale DPF simulation. Since the computational effort is substantial, we employed a simplified 4-channel model (Fig. 1.16) to check whether a scalar modeling of soot would be suitable for the problem. Simulations of this section were carried out by a modified version of KIVA3V computer program particularly designed for DPF. The basics of such changes were done by Piscaglia et al. [65] and they were afterwards extended by us [59, 64].

Reference data Soot properties used to validate the lagrangian approach were taken from the experimental work by Wirojsakunchai et al. [93]: exhaust gas from a research engine was analyzed to obtain particle diameter probability density function for three operating conditions, namely, 'mode 3' (high speed, low load), 'mode 4' (low speed and low load) and 'mode 5' (low speed and high load). Such distributions were used to generate injected particles diameters by a Monte Carlo method [5]. In Fig. 1.17 the experimental PDFs are represented, together with the histograms of the diameter of particles used in the simulations.

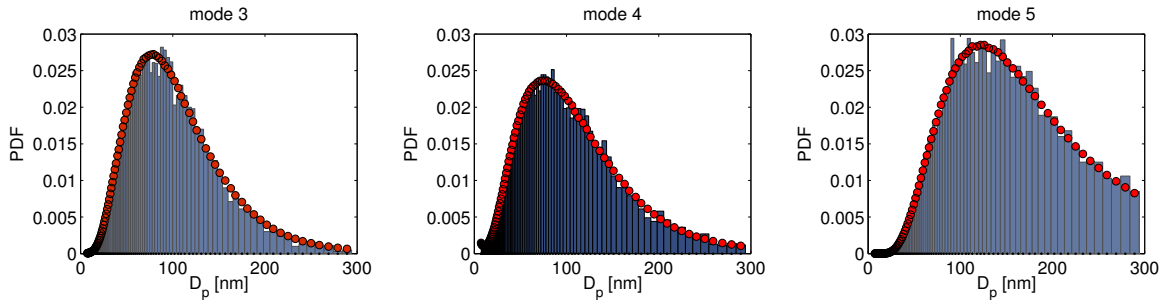

Figure 1.17: PDFs of soot particle used for validating the lagrangian approach. For a description of engine working conditions, see [93]

Results In Fig. 1.18 the histogram of particle Stokes number is represented: distribution is higly skewed towards very low values ($\approx 10^{-4}$) and maximum values of St are always lower than 10^{-3}. As a consequence, the particle diameter distributions does not change along the filter axial direction, cf. figs. 1.19 and 1.20.

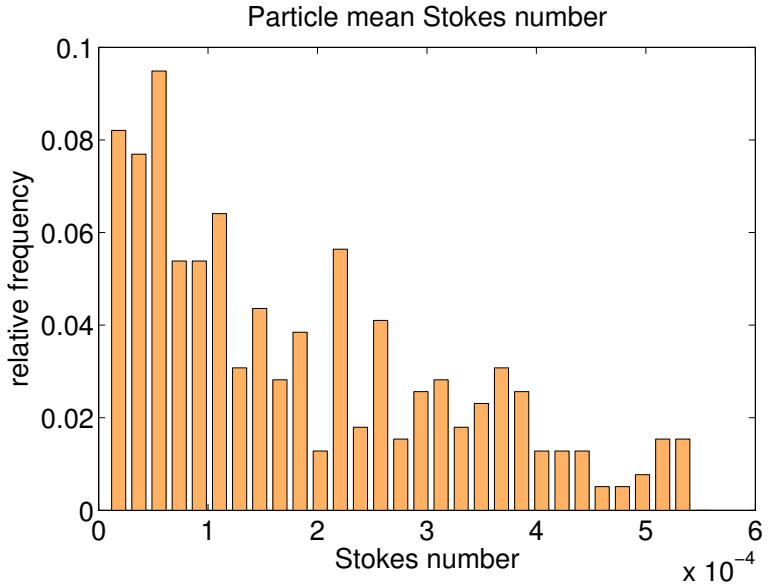

Figure 1.18: Histogram of particle Stokes number obtained by simulation.

Since the Stokes number has been proven to be very low and thus the particle distribution is uniform along the filter length, it is possible to state that simulating soot particles as a convected chemical specie is an accettable approximation. From now on, this approach will be used for filter loading study.

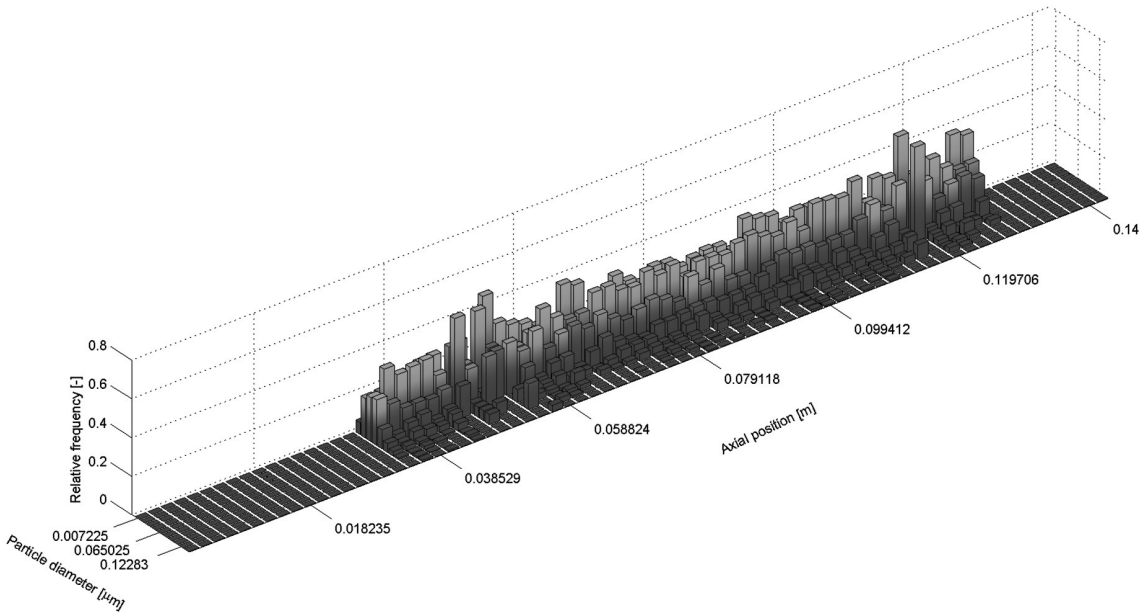

Figure 1.19: Histograms of particle diameter for different axial coordinate z. No substantial variation of PDF can be inferred.

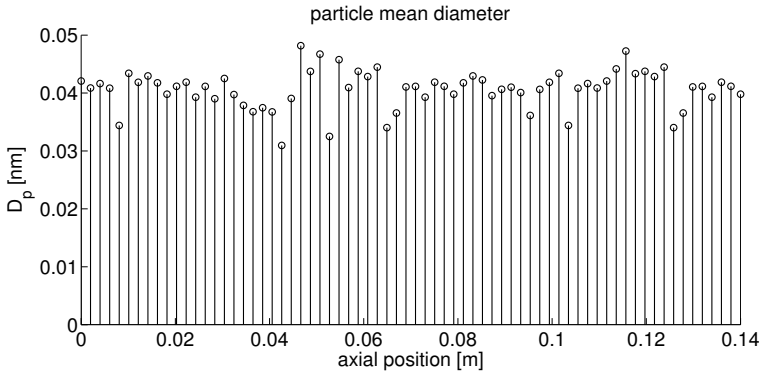

Figure 1.20: Mean particle diameter along filter axial coordinate. Distribution is statistically uniform.

1.5.2 Scalar modeling

1.5.2.1 Governing equation

When considering soot as a passive scalar advected by the gas flow, its distribution is supposed to be homogeneous within the control volume, and concentration is expressed by its mass fraction:

$$s = \frac{m_{gas}}{m_{soot}} \tag{1.62}$$

that obeys to the following governing equation (1.63):

$$\frac{\partial \rho s}{\partial t} + \nabla \cdot (\rho s) + \Gamma \nabla^2 s \tag{1.63}$$

where Γ is the diffusion coefficient due to turbulent dispersivity, brownian motion and thermophoresis. Usually diffusive effects are negligible in cold flows: they will be therefore neglected from now on and eventually reconsidered in a later study.

1.5.2.2 Soot particles deposition

Soot deposition takes place on porous surfaces and can be modeled by inserting a surface sink term in Eq. (1.63):

$$\frac{\partial \rho s}{\partial t} + \nabla \cdot (\rho s) + \Gamma \nabla^2 s = \dot{S} \tag{1.64}$$

Sink term $\dot{S}$ has to be applied only on porous surfaces:

$$\dot{S} = \begin{cases} \eta_f \cdot \phi_{soot} & \text{for porous surfaces} \\ 0 & \text{otherwise} \end{cases} \tag{1.65}$$

where η_f is the filtration efficiency (ref. section 1.5.2.3) and $\phi_{soot} = \phi_f s_f$ is soot mass flux across porous surface.

In the FV framework, Eq. (1.64) reads:

$$\rho \frac{s_p^{n+1} - s_p^n}{\Delta t} + \sum_f \phi_f s_f^{n+1} - \sum_f \eta_f \phi_f s_f = 0 \tag{1.66}$$

$$\rho \frac{s_p^{n+1} - s_p^n}{\Delta t} + \sum_f (1 - \eta_f) \phi_f s_f^{n+1} = 0 \tag{1.67}$$

$$\rho \frac{s_p^{n+1} - s_p^n}{\Delta t} + \sum_f (1 - \eta_f) \phi_f \left[\alpha_f s_p^{n+1} + (1 - \alpha_f) s_N^{n+1} \right] = 0 \tag{1.68}$$

where the effect of porous surfaces for soot removal are included in the convection term. Subscript N designates the neighbour cell that lies on the other side of face f, and α_f are the interpolation weights. The purpose of sink term is not to account for soot removal from inlet channels (since this is already the outcome of convection), but to block soot from entering the outlet channels. In other words, soot filtration efficiency η_f acts only when corresponding flux ϕ_f points *inward* the cell.

Discretization procedure to get Eq. (1.66) is all but straightforward since sink term has to be selectively activated only for some faces depending on the flux direction, and these faces are not predefined at the beginning of the simulation. Therefore, the following procedure is followed:

1. Build convection equation *without* considering any sink term:

$$\rho \frac{s_p^{n+1} - s_p^n}{\Delta t} + \sum_f \phi_f s_f^{n+1} = 0 \tag{1.69}$$

2. for each cell, find faces that have soot flux pointing inwards the cell

3. for that faces, multiply linear system matrix coefficients by $(1 - \eta_f)$

4. Solve conservation equation the usual way.

1.5.2.3 Filtration model

All physical phenomena related to soot deposition on porous surfaces are taken into account by the filtration efficiency η_f that is a non-constant and local variable, that depends on the substrate porosity and the deposited soot amount.

Interception of soot particles by the filtrating walls can be due to a number of mechanisms and any expression of the collection efficiency has to take them into account. Among others, we may regard as influential only brownian diffusion and direct interception by the spherical collectors. Other phenomena that may occur can be considered as negligible for the thermophysical conditions under study: inertial impact is ineffective for Stokes number lower than 0.4, and thermophoresis can be neglected too when dealing with cold flows (it might be important however when filter regeneration is simulated).

Following the work of other authors [51, 52, 41, 56], porous wall is assumed to consist of a number of identical spherical unit cells of diameter b; each one consisting of a spherical unit collector of diameter d_{c0}, that is related to the mean physical quantities of the substrate:

$$d_{c0} = \frac{3}{2} \frac{1 - \varepsilon_0}{\varepsilon_0} d_{por} \tag{1.70}$$

where porosity is defined – as usual – as the ratio between the total volume of the unit cell and the "empty" volume not filled by the spherical collector ($1 - \varepsilon_0 = d_{c0}^3 / b^3$.)

In the above expression (1.70) and in the followings, the subscript '0' will denote 'clean trap' conditions, i.e., when soot collection has not yet taken place, so that substrate properties are defined only by porous medium characteristics.

Brownian diffusion efficiency According to [35], Brownian diffusion efficiency can be estimated as:

$$\eta_D = 3.5 g(\varepsilon) \mathrm{Pe}^{-2/3} \tag{1.71}$$

where $\mathrm{Pe} = u d_c / \Gamma_B$ is the Peclet number.

$g(\varepsilon)$ is a function of porosity and it is defined as:

$$g(\varepsilon) = \left[\frac{\varepsilon}{2-\varepsilon} - 9/5(1-\varepsilon)^{1/3} - 1/5(1-\varepsilon)^2\right]^{1/3} \tag{1.72}$$

Diffusion coefficient Γ_B due to Brownian motion can be estimated as a function of temperature, viscosity and Knudsen number of the fluid:

$$\Gamma_B = \frac{\mathrm{k_B} T}{3\pi\mu d_p}\left[1 + \mathrm{Kn}\left(1.257 + 0.4\mathrm{e}^{-1.1/\mathrm{Kn}}\right)\right] \tag{1.73}$$

Direct interception efficiency Efficiency of particle collection by direct interception is given by:

$$\eta_R = \frac{3}{2} N_R^2 \frac{g^3(\varepsilon)}{(1+N_R)^{(3-2\varepsilon)/3\varepsilon}} \tag{1.74}$$

where $N_R = d_p/d_c$ is the ratio between particle and collector diameters.

Global efficiency and substrate permeability Total interception efficiency of the unit collector can be calculated by superposing both the effects of Brownian diffusion and direct interception:

$$\eta = \eta_D + \eta_R - \eta_D \eta_R \tag{1.75}$$

The global efficiency of the filter wall per unit area can be calculated by integrating the above expression across the substrate thickness:

$$\eta_f = 1 - \exp\left[-\frac{3\eta(1-\varepsilon)\mathrm{w}_{por}}{3\varepsilon d_c}\right] \tag{1.76}$$

The particle deposition within the filter wall can be considered to form a uniform layer outside the unit collectors. The result leads to an increase in the unit collector diameter and a decrease in the local porosity and permeability of the filter wall. This can be expressed as:

$$d_c = 2\left[\frac{3 \cdot m_c}{4\pi \cdot \rho_{soot,w}} + \left(\frac{d_{c0}}{2}\right)^3\right]^{\frac{1}{3}} \tag{1.77}$$

$$\varepsilon = 1 - \left(\frac{d_c}{d_{c0}}\right)^3 \cdot (1-\varepsilon_0) \tag{1.78}$$

$$k = k_0\left(\frac{d_c}{d_{c0}}\right)^2 \cdot \frac{\varepsilon^3/[(1-\varepsilon)^2]}{\varepsilon_0^3/[(1-\varepsilon_0)^2]} \tag{1.79}$$

The amount of soot that is trapped into the porous wall is only a fraction of the total mass that is captured by the unit collector and that contributes to the decrease of the permeability; the rest of it remains on the porous medium surface to form the *soot cake*. Ratio between trapped and surface-laden soot mass is described by the participation factor Φ (1.80):

$$\Phi = \frac{d_c^2 - d_{c0}^2}{(\psi b)^2 - d_{c0}^2} \tag{1.80}$$

where b is the characteristic size of the unit collector cell and ψ ($0 \leq \psi \leq 1$) a coefficient for taking into account the effects of pore bridging [52].

As a consequence of the two mechanism of soot removal (trapping inside the porous medium or deposition on its surface), the overall resistance of a loaded trap is defined by the sum of two Darcy terms:

$$D = -\mu u_w \left(\frac{\mathrm{w}_{por}}{k_{\mathrm{por}}} + \frac{\mathrm{w}_{soot}}{k_{\mathrm{soot}}} \right) \tag{1.81}$$

where w_{soot} and k_{soot} are, respectively, thickness and permeability of soot cake.

Chapter 2

DPF results and discussion

The modeling procedures explained in section 1.4 and 1.5 have been implemented in an open-source general-purpose CFD code, and the approach has been verified on real test cases for which experimental data are available in the literature. The goal of this part is to investigate the predictability of the new solver when applied to real-world cases, where a strong interaction is present between the full-scale filter and the flow field in the inlet and outlet cones.

The chapter is organized as follows. In section 2.1.1 the basics of the proposed approach will be evaluated and assessed. In particular, the following aspects will be investigated: capability of predicting the clean trap pressure drop, flow distribution properties on the frontal section and the details of the flow into monolith channels. In section 2.1.2 the open frontal area (OFA) correction term, explained in section 1.4.4.3, will be inserted into the flow equation and its influence will be discussed. The model predictivity with respect to different filter geometries with the same substrate properties will be assessed in section 2.1.3.

Loading results are collected in section 2.2. First, simplified 2-channel and 4-channel geometries will be studied to verify the implementation of the filtration model. Afterwards, a complete simulation of a full scale filter with soot loading and deposition will be shown.

2.1 Clean gas flow

2.1.1 Basic approach validation

2.1.1.1 Reference data

A first set of experimental data for the validation of the pressure drop predicted by the implemented code for clean traps has been taken from the work of Masoudi et al. published in [41]. Pressure drop across the filter of Tab. 2.1 was measured: in the experiments, dry

air flow supplied from a compressor wasdirected through a 50.8 mm diameter pipe, where a flow straightener was included to minimize the upstream flow fluctuations.

Table 2.1: Specification of the Corning EX-80 5.66"x6" 100/17 diesel particulate filter used in the experiments carried out in [41].

filter type	EX-80 5.66"x6" 100/17
channel length	152.4 mm
plug length	10 mm
channel width	2.11 mm
porous wall thickness, w_s	0.432 mm
cell density	100
porosity	49%
mean pore size	13 μm

Downstream of the straightener, air passed through a flow meter , then through a pipe having a length of 10 pipe diameters, to be sure that the turbulent flow velocity was completely developed before approaching the filter. The static pressure drop across the filter was measured by a differential manometer (0-1500 Pa). Minor flow temperature variations were monitored using a thermocouple inserted in the flow path upstream of the filter. The experimental setup was thought to have only a core (having a diameter of 67.5 mm) of the filter subjected to the flow. After positioning the filter on the assembly, the filter was subjected to a range of flow rates and the pressure drop across the filter was recorded (Fig. 2.1). A detailed description of the experimental setup and procedure is given in [41].

2.1.1.2 Case setup

The trap described in tab. 2.1 has been discretized using a hybrid tet/hex mesh depicted in fig. 2.2. The number of computational cells in the grid is 199260 (96462 hexahedra, 2186 pyramids, 100612 tetrahedra). Velocity calculated on the basis of the experimental mass flow rate is imposed on the inlet section while static pressure is set at the outlet (fig. 2.2). Ambient conditions are used to initialize temperature and pressure. For the first set of results, a steady-state solver based on the SIMPLE algorithm was adopted [26].

Besides the standard thermo- and fluid-dynamic quantites, the solver requires to be supplied also with the permeability of the porous medium. Unlike other properties of the porous walls, permeability does not have an exact physical meaning since it is defined on the basis

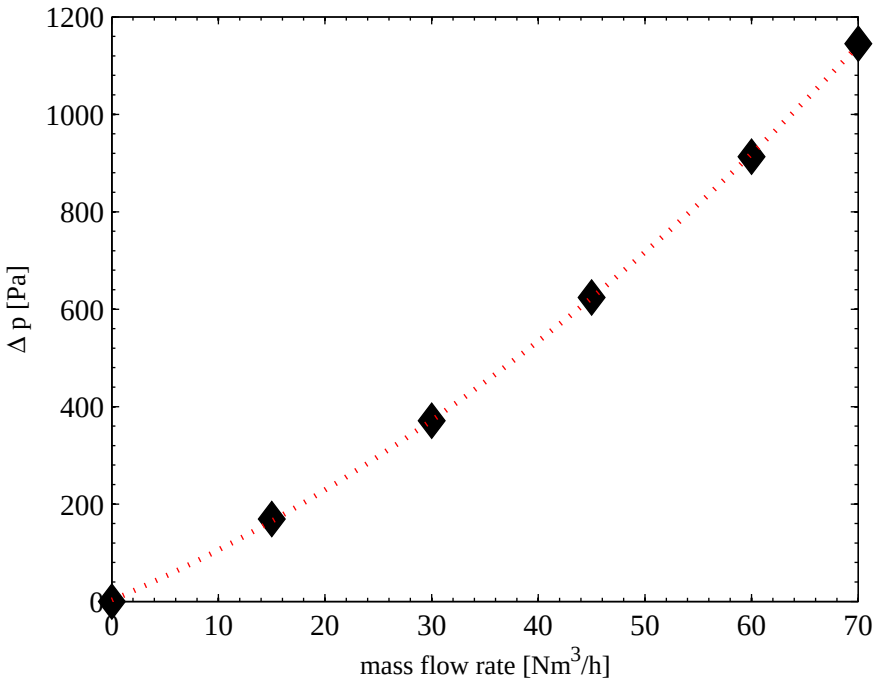

Figure 2.1: Experiemental pressure drop versus mass flow rate [41]

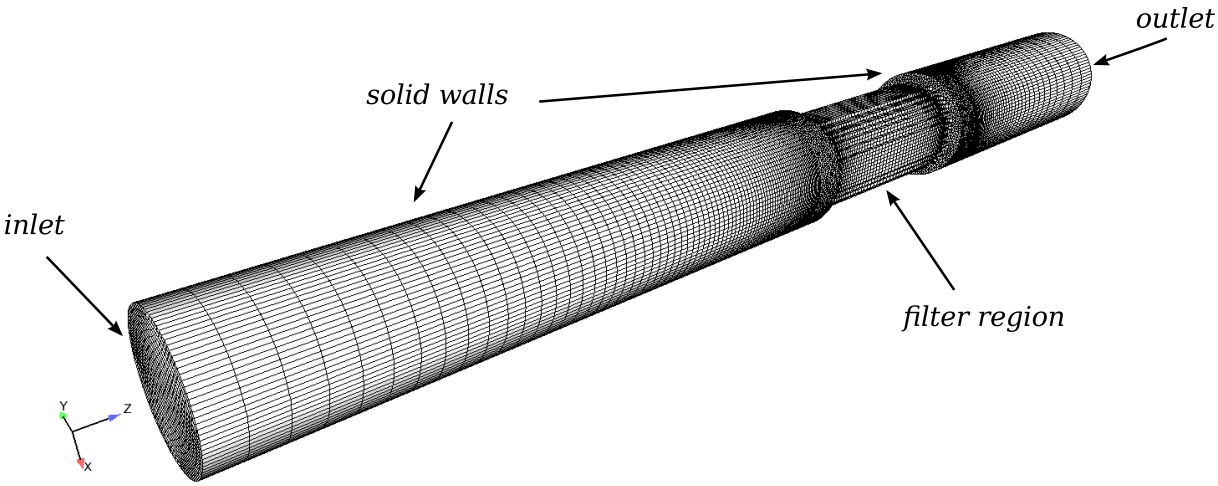

Figure 2.2: FV mesh used for simulations with specification of boundary conditions.

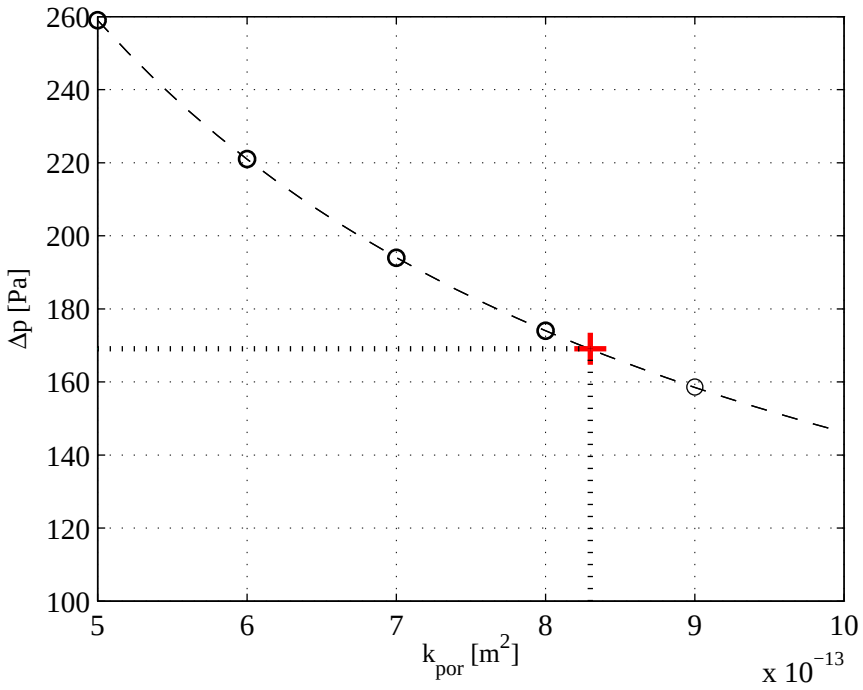

Figure 2.3: Tuning of permeability for the first point of the curve. Hollow circles: computed ΔP; dash line: fit with power-law function; red cross: matching point

of Darcy's Law. Thus, its value might change according to the approach used to model the pressure drop and hence it requires some tuning. In this work, the local permeability k_{por} has been tuned to match the filter pressure drop at the lowest flow rate point, in order to minimize other non-Darcy effects that might bias the result.

Five simulations with an inlet mass flow rate of 15 Nm^3/h (corresponding to $5.93 \cdot 10^{-3}$ kg/s) have been performed, with different values of permeability ranging from $5 \cdot 10^{-3}$ m^2 to $9 \cdot 10^{-3}$ m^2. The curve $\Delta P(k_{\text{por}})$ (figure 2.3) has been fit with a power-law function $y = ax^b + c$ that interpolates the data almost perfectly, with $R^2 = 1.0000$. The lowest experimental pressure drop point has been matched with a permeability of $8.3 \cdot 10^{-13}$ m^2 (represented by the red cross in figure 2.3).

2.1.1.3 Results and discussion

Pressure drop Pressure drop versus inlet mass flow rate is shown in Fig. 2.4. The agreement between simulations and experiments looks quite satisfying, even though a slight underestimation of the pressure drop can be observed. The discrepancy between numerical and experimental results increases with mass flow rate, suggesting that the deviation from the expected behavior is related to some non-linear phenomena. Among the possible causes:

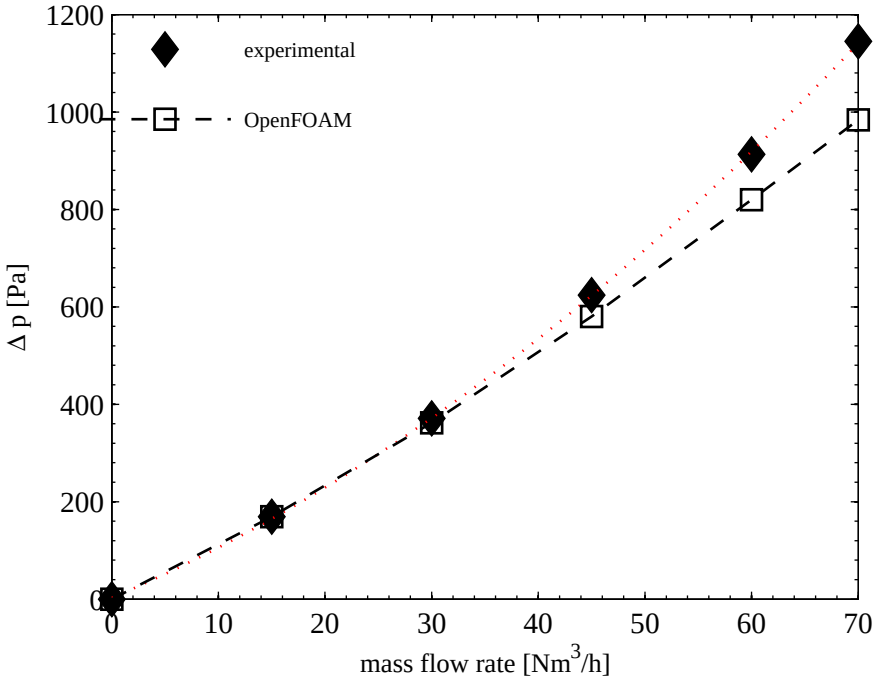

Figure 2.4: Comparison between experimental and computed pressure drop values.

underestimation of the OFA that may lead to higher mean velocities inside the channels, underestimation of contraction/expansion losses, inaccurate estimation of the Forchheimer coefficient β or the streamwise friction factor F.

Flow field Global flow field is represented in Fig. 2.5, while pressure field is represented in Fig. 2.6. These images give a precise idea of our original modeling approach. There is no continuity break between the inlet/outlet cones and the DPF as can be seen in Fig. 2.5, and the filter channels are clearly recognizable by the pressure difference between them (Fig. 2.6). Moreover, a magnified snapshot of the filter inlet and outlet region is visible in Fig. 2.7, where the modeling of channels as 1D array of cells is made evident.

Flow non-uniformity A 3D full-scale DPF model allows also for the prediction of the flow distribution. Despite in the studied case the flow straightener was thought to allow for uniform radial flow distribution over the filter cross section [41], this actually does not completely happen. The mean flow velocity has been sampled at two cross sections near the inlet and the outlet frontal faces of the monolith, called, respectively, “front plane” and “rear plane”, cf. Fig. 2.8.

Flow velocity (that is proportional to the mass flow flux) is lower in the channels near

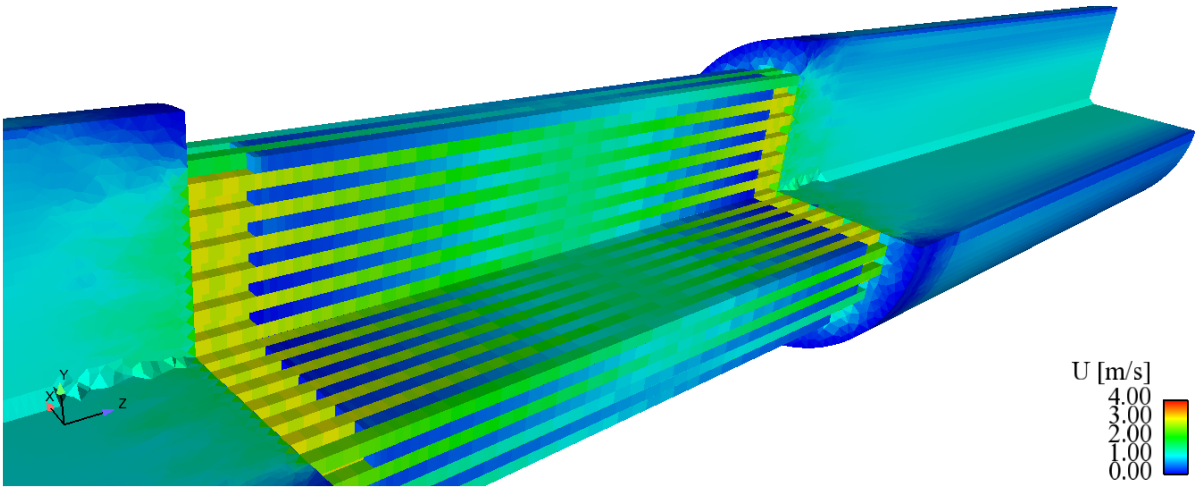

Figure 2.5: Global view of simulated velocity field in the filter region

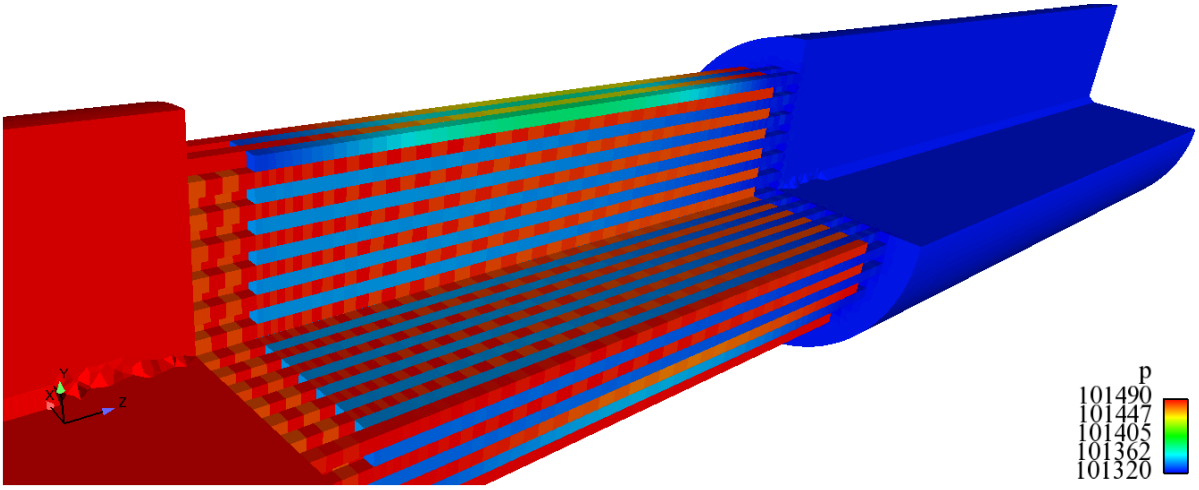

Figure 2.6: Global view of simulated pressure field in the filter region: inlet and outlet channels are clearly distinguishable.

(a)

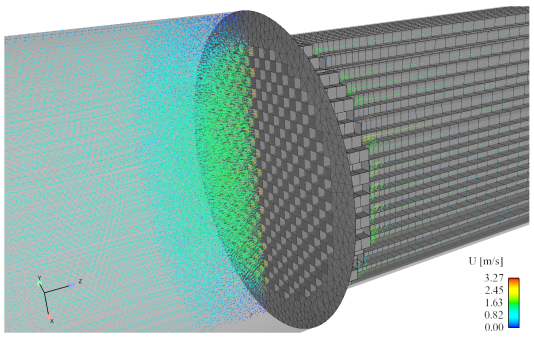

(b)

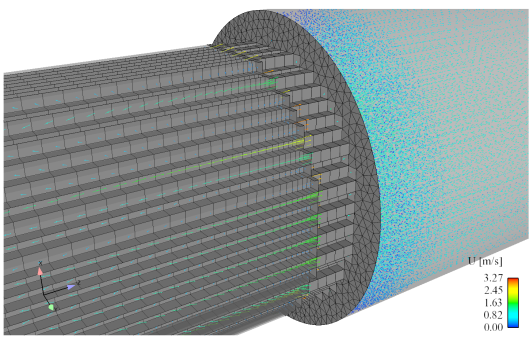

Figure 2.7: Closeup view of velocity field near the filter faces where contraction/expansion losses occur. (a) front (inlet) section; (b) rear (outlet) section.

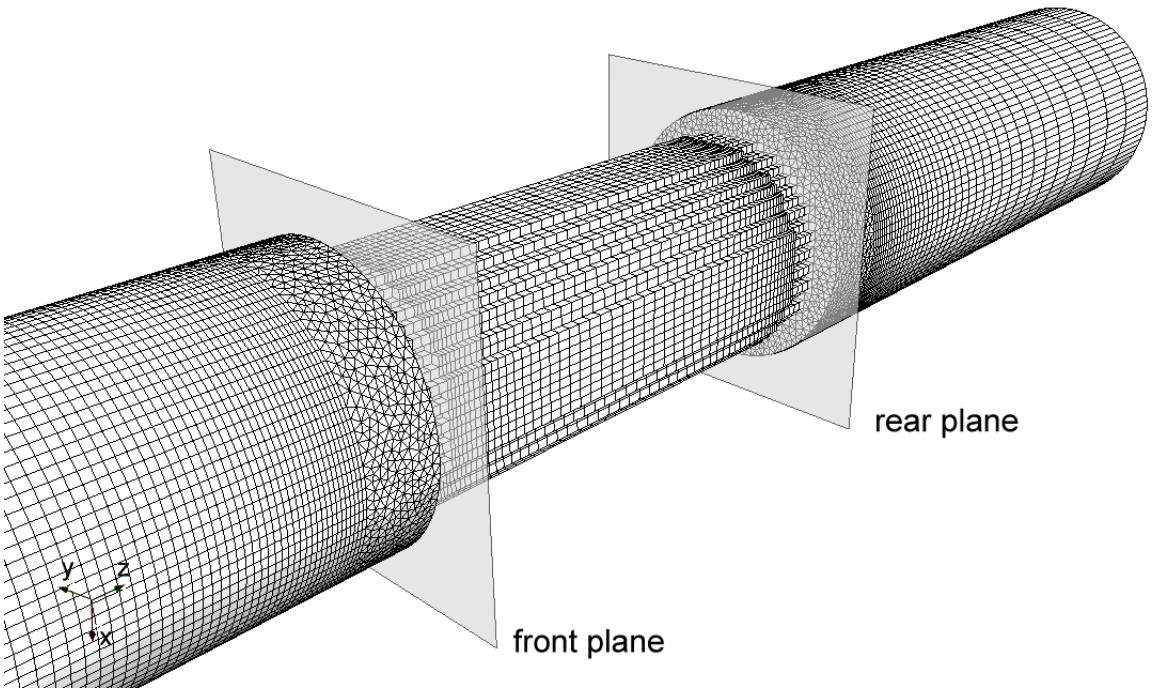

Figure 2.8: Location of front and rear planes used to evaluate flow uniformity.

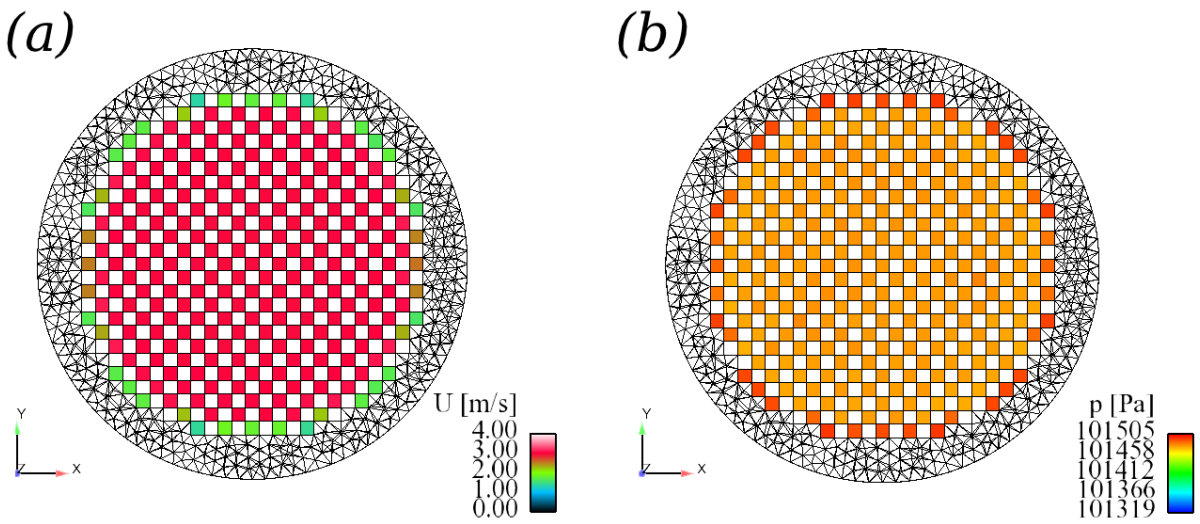

Figure 2.9: Velocity (a) and pressure (b) distribution on the filter front plane. Except for boundary channels, fields are uniform.

the walls (Fig. 2.9-a) where pressure is higher (Fig. 2.9-b). Non uniformity along the radial direction is caused by the geometry of the inlet cone, by the flow profile near the walls, but also by the resistance of filter channels to the flow.

By looking at Figs. 2.9 and 2.10, filter channels may be devided into three different kinds: channels having four filtrating walls, channels having three filtrating walls and channels hav-

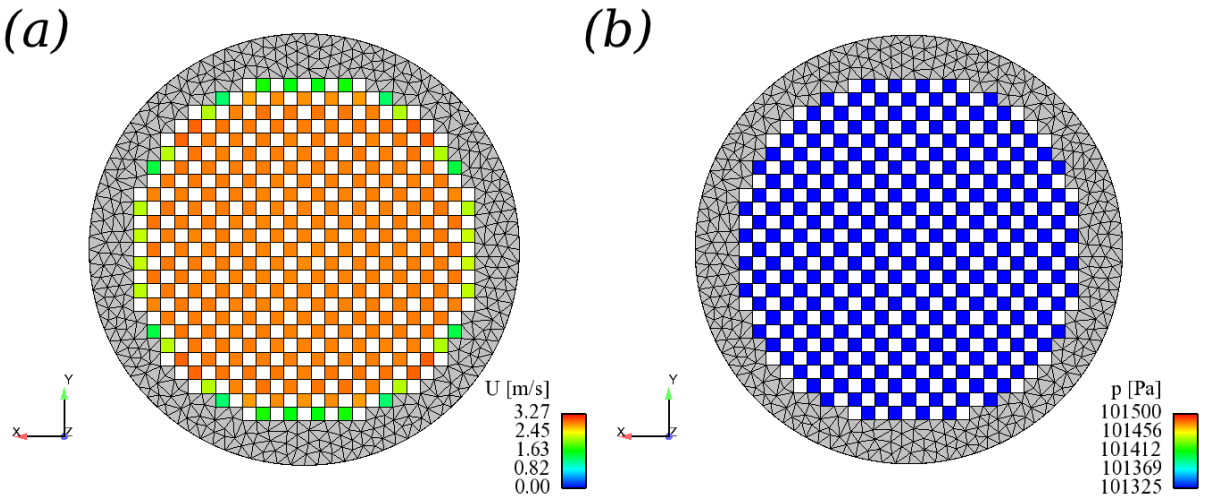

Figure 2.10: Velocity (a) and pressure (b) distribution on the filter rear plane. Except for boundary channels, fields are uniform.

ing two filtrating walls. The number of filtrating walls affects the wall-flow velocity profile and hence the pressure drop in the channel. Fig. 2.9 and 2.10 show, respectively, the radial flow distribution over the front and the rear section of the filter. As expected, pressure in the front face of the filter is higher near the edges, where the gas velocity is lower and where most of the inlet channels have two filtrating walls. For those channels, wallflow velocity (and the pressure drop) is higher. In the rear section of the filter monolith flow pressure is uniform (Fig. 2.10-b), as expected; a non-uniform pressure distribution over the outlet section would cause reverse flow towards those channel ends characterized by lower pressure.

Differences between velocity and pressure profiles into the channels with different number of filtrating walls are shown in the next figures (Figs. 2.11, 2.12 and 2.13). The velocity field has been sampled from the complete solution along the monolith length for some pairs of filter channels, either on the channel axis or at the center of the filtrating wall. Some interesting results emerge from this analysis.

Not only the mean velocity is higher when the number of filtrating wall decreases (as can be seen in Fig. 2.12), but also the profile of wall flow velocity is different. In particular, higher mean velocities due to the presence of only 2 filtrating walls instead of 4 cause higher filtration velocities. Because of Darcy's Law, greater pressure differentials are observed as well (Fig. 2.13). Also, the shape of the curve changes when decreasing the number of porous surfaces, leading to an increase in concavity and greater differences between the ends and the center of the channels.

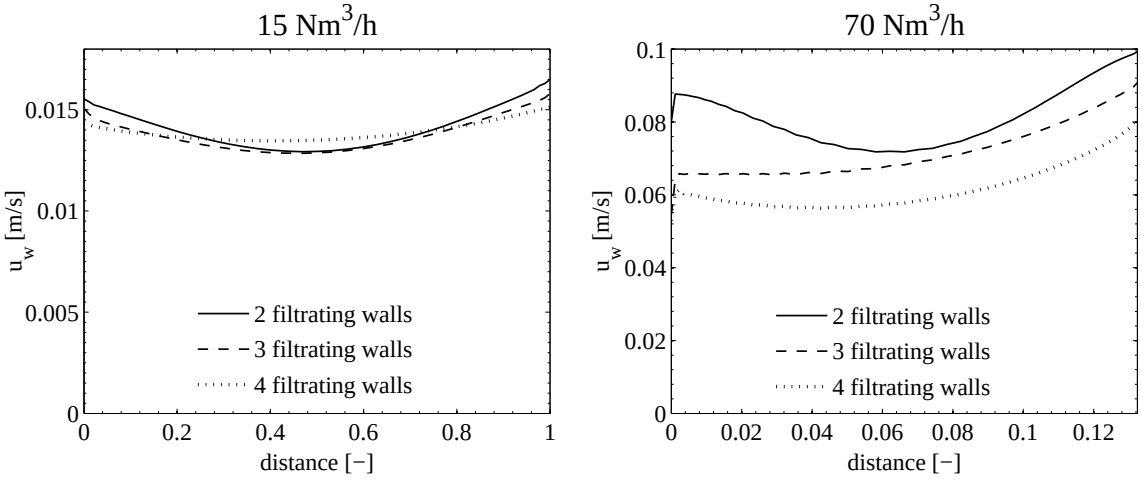

Figure 2.11: Wallflow velocity u_w for two mass flow rates and different locations of the channels. Channels inside the filter core have 4 filtrating walls, channels on the boundary either have 2 or 3 filtrating walls.

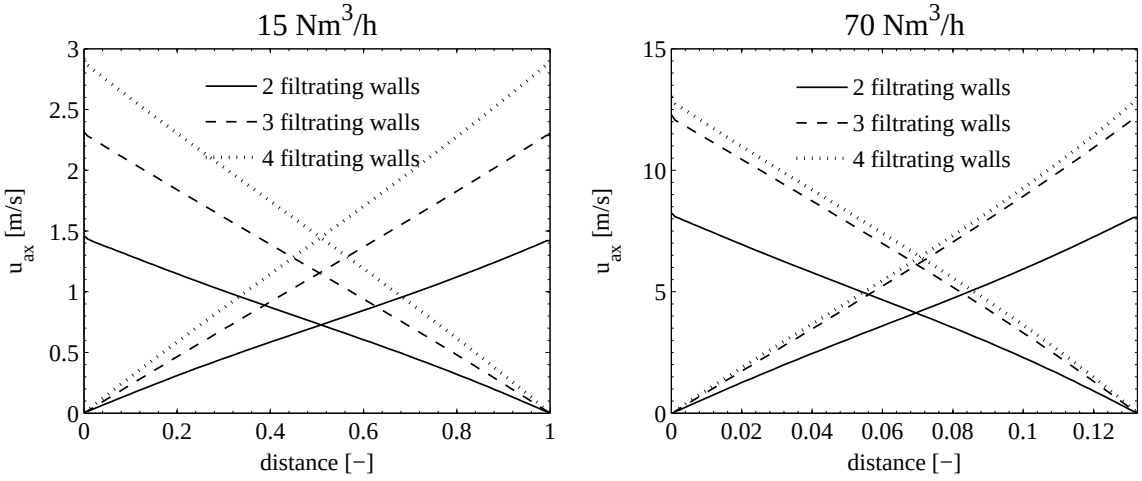

Figure 2.12: Axial velocity along filter axis for some selected channel pairs, whose wallflow velocity has been represented in previous figure (2.11). Inlet channels have a negative slope curve; conversely, outlet channels have increasing (positive slope) velocity.

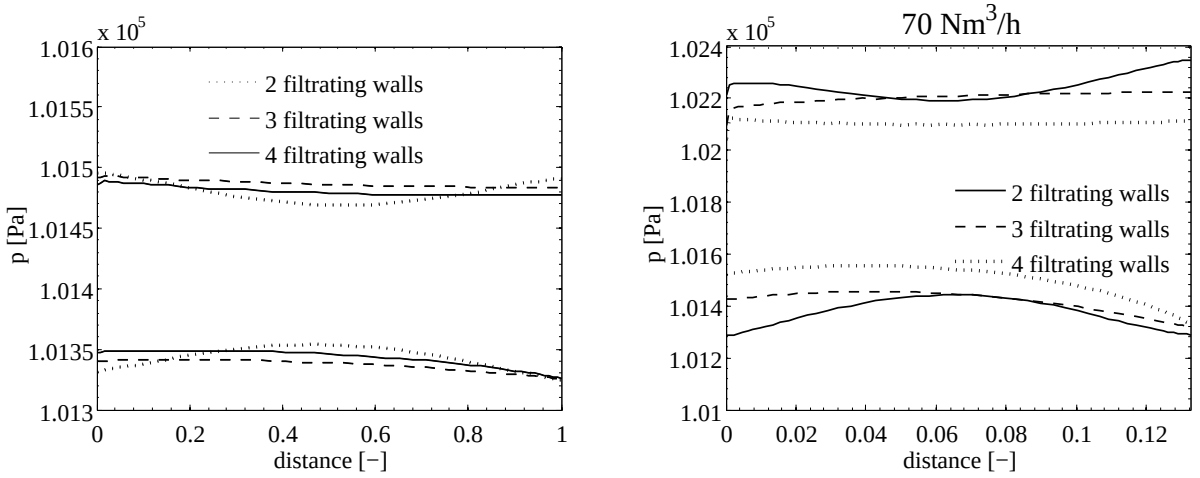

Figure 2.13: Pressure values along filter axis for the same channel pairs of previous graphs (fig. 2.12).

Numerical properties Finally, some considerations can be made about the numerical behaviour of the solver. Generally speaking, the SIMPLE algorithm is not always guaranteed to converge rapidly, especially for complex flow situations. The most common workaround is to improve convergence by adding only a portion of the new solution to the old one, i.e.

$$\phi^{n+1} = \phi^n + \alpha_\phi \cdot (\phi^{NEW} - \phi^n) \tag{2.1}$$

where $0 < \alpha_\phi \leq 1$ is defined as the *under-relaxation factor* for the unknown quantity ϕ. The lower the α, the more robust the solver will be, but the more the accuracy will suffer and, of course, the longer it will take to have a converged solution.

Due to the explicit insertion of the porous sink term, the system of PDE becomes very stiff and difficult to solve numerically. Achieving convergence with the SIMPLE algorithm will thus require very low under-relaxation factors. As the resistance increases (lower values of k_{por}), the under-relaxation factors have to be lowered as well in order to guarantee the stability of the solution. We found out that, using the explicit formulation of the Darcy loss, the under-relaxation factors have to be lower than $5 \cdot 10^{-4}$ to avoid instability (usual values for common flow problems are in the range $0.1 \div 0.9$). In Fig. 2.14, 2.15 and 2.16 the residual histories of, respectively, streamwise velocity, transverse velocity and pressure are plotted against the number of SIMPLE iterations. Normalized residuals are defined as:

$$r_{\mathbf{x}}^{(n)} = \frac{\|\mathbf{A}^{(n)}\mathbf{x}^{(n)} - \mathbf{b}^{(n-1)}\|}{\|\mathbf{x}^{(n)}\|} \tag{2.2}$$

where $\mathbf{x}^{(n)}$ is the discrete solution at time step n and $\mathbf{A}$ and $\mathbf{b}$ are, respectively, the matrix and the RHS of the discrete linear system.

Apart from the very low values of α needed for convergence, it may be seen that sometimes it is required to decrease the relaxation factors even more to achieve acceptably low levels of residuals. On the other hand, improving convergence by very small relaxations usually lowers accuracy of the solution. In this case, the lack of accuracy can be seen from Fig. 2.6 where some sort of checkerboard pattern is present in the pressure field even when numerical convergence has been reached.

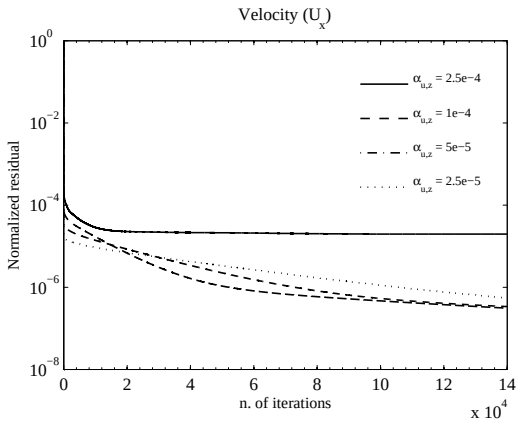

Figure 2.14: Residuals on momentum equation (axial component) with different under-relaxation factors α_U.

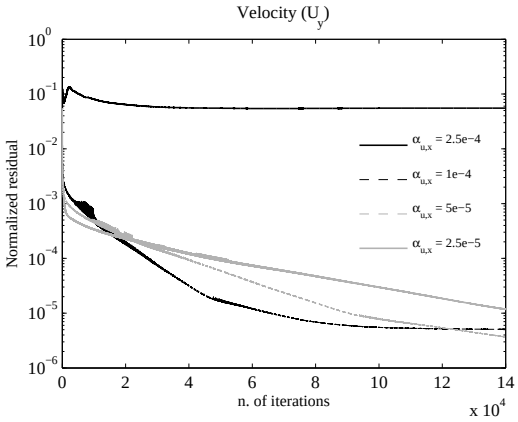

Figure 2.15: Residuals on momentum equation (transverse component) with different under-relaxation factors α_U. For $\alpha_U = 2.4 \cdot 10^{-4}$ convergence is not achieved.

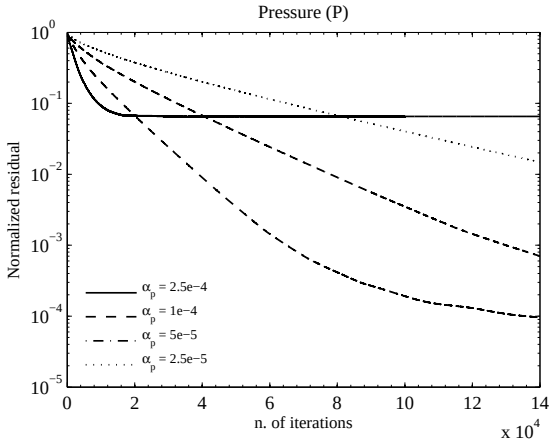

Figure 2.16: Residuals on pressure equation with different under-relaxation factors α_p. For $\alpha_p = 2.4 \cdot 10^{-4}$ convergence is not achieved.

A common way to improve accuracy of steady-state simulations, especially when stability issues arise, is to perform a pseudo-transient simulation [87]. Steady-state flow field can

be computed with an unsteady solver, like PISO or transient-SIMPLE, and allowing the solution to reach a converged state. In fig. 2.17, it is shown a comparison between the solution obtained with a steady SIMPLE solver (left) and with an unsteady piso solver. The strong velocity checkerboarding disappears completely when moving to an unsteady procedure. Unfortunately, due to the explicit formulation of source terms, small timesteps have to be used anyway, so that little or no advantage is gained over the computational time. However, if some inherently unsteady phenomena occur, an unsteady algorithm would be able to catch them, avoiding to draw inappropriate conclusions from unphysical solutions.

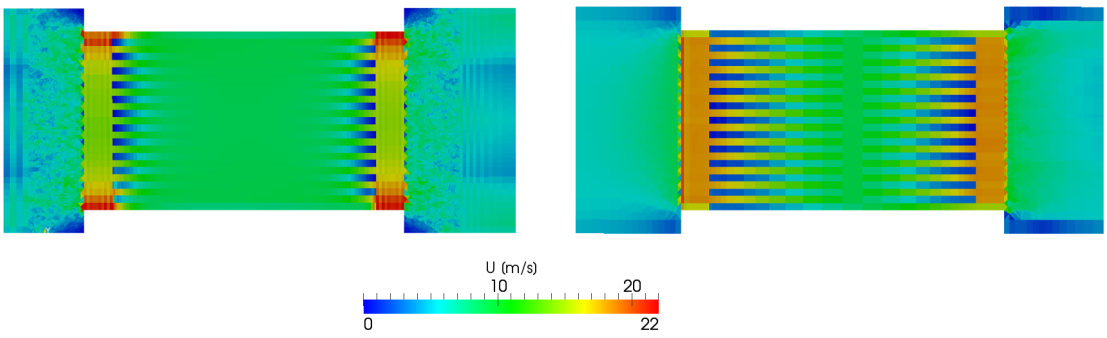

Figure 2.17: Comparison between solutions obtained with steady solver SIMPLE (left) and unsteady PISO (right). Using a transient solver to calculate a steady solution can lead to better accuarcy and to avoid checkerboarding when very small under-relaxation factors are used.

2.1.2 Open frontal area correction term

In section 1.4.4.3 it was pointed out that the difference of OFA between the real and the modeled geometry can easily lead to a misprediction of the mean velocity field and, thus, of the overall pressure drop of the filter. In this section three possible modeling strategies will be investigated. First, the cell width will be considered as equal to the channel transverse pitch, so that the external filter dimensions are preserved: this is important when dealing with complex piping geometries that cannot be easily scaled. Secondly, a cell width equal to the real channel inner side a will be considered, so that the correct OFA is used in the model, albeit the external dimensions are different from the real ones. Finally, the OFA correction term will be added to the first approach to verify its formulation.

The set of experimental data used for basic validation (section 2.1.1) has been used for this part too.

2.1.2.1 Case setup

The same solver and boundary setup of the previous section have been used for this part, except for the finite volume grid. Two different meshes have been employed, that are represented in Fig. 2.18. In particular, the first one (Fig. 2.18-a) has the channel width equal to the cell pitch $a + w$, whereas in the second one (Fig. 2.18-b) the channel width has been scaled down to a to ensure a correct modeling of the total OFA. Mesh of Fig. 2.18-a has been used for case 1 and 3, while mesh of Fig. 2.18-b has been used for case 2.

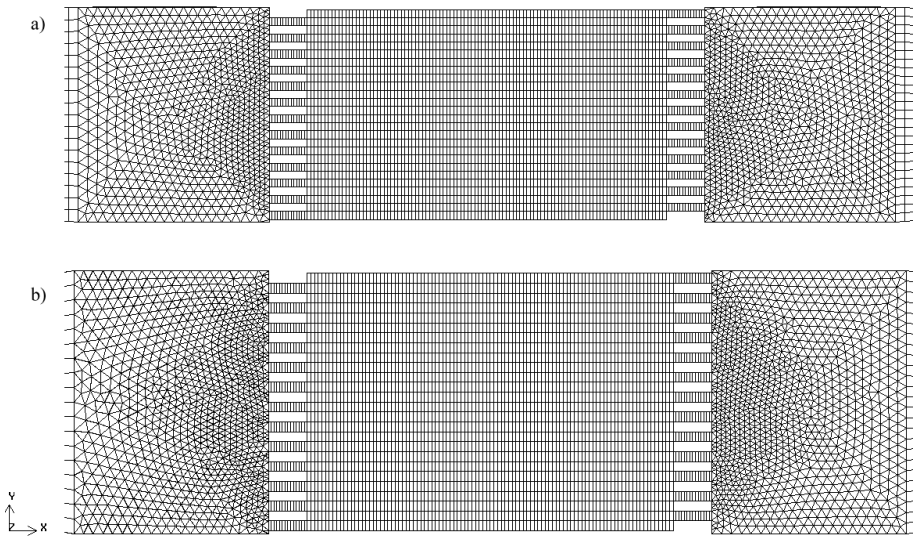

Figure 2.18: Comparison between meshes used for OFA influence evalation. Top mesh preserves actual channel width, bottom mesh preserves channel pitch and global geometry.

2.1.2.2 Results and discussion

Pressure drop versus inlet mass flow rate is depicted in Fig. 2.19 for the cases mentioned above. It is clearly seen that, besides the already observed underprediction of overall pressure drop that takes place with the larger cell size (side = $a + w$), adopting the real channel size as cell side (side = a) leads to a certain overprediction of the filter pressure drop. Finally, a better result is obtained by using the larger cell size and the correction term introduced in section 1.4.4.3. Still, the predictions of pressure drop at high flow rates are slightly underestimated even with the correction term. This can be probably due to a too coarse mesh resolution near the filter frontal faces, that in turns produces an incorrect estimation of contraction/expansion losses.

Wallflow velocity and pressure difference profiles between adjacent channels does not exhibit significant changes when different approaches are used, as can be seen in Fig. 2.20

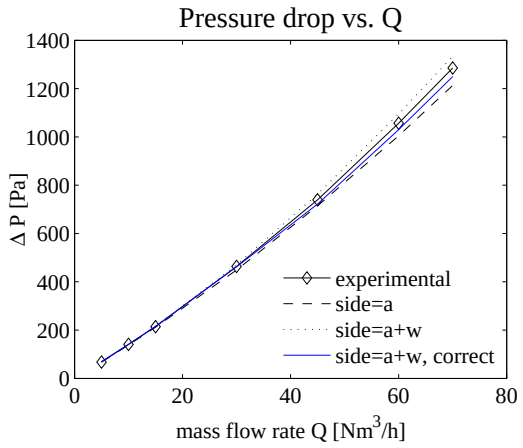

Figure 2.19: Comparison between pressure drop versus flow rate curves for various approaches: channel-width preserving, geometry-preserving, geometry-preserving with correction term.

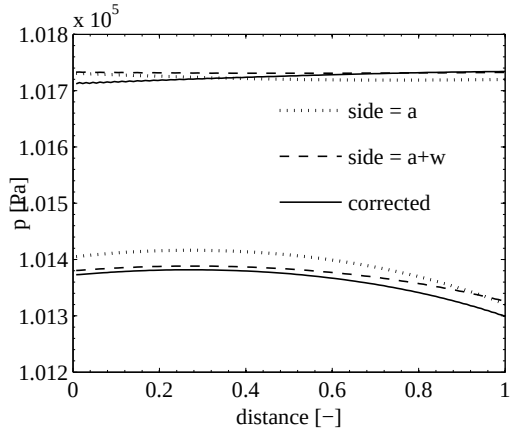

Figure 2.20: Comparison between channel pressure profiles for various approaches: channel-width preserving, geometry-preserving, geometry-preserving with correction term.

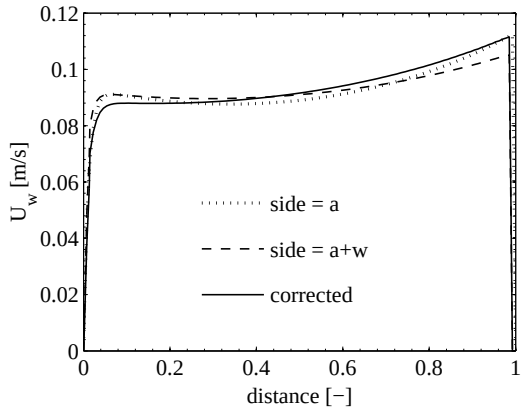

Figure 2.21: Comparison between wallflow velocity profiles for various approaches: channel-width preserving, geometry-preserving, geometry-preserving with correction term.

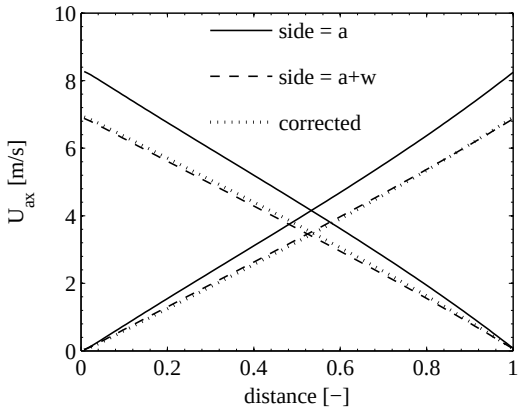

Figure 2.22: Comparison between axial velocity profiles for various approaches: channel-width preserving, geometry-preserving, geometry-preserving with correction term.

and 2.21. On the other hand, mean axial velocity is quite higher in the "shrinked" case (side = *a*), but this doesn't reflect on a difference in transverse velocity due to continuity equation being fulfilled anyway.

2.1.3 Model predictivity

In order to assess the model predictivity when geometry is changed, simulations have been performed with filters of varying lengths, namely, 63 mm, 114 mm and 165 mm. The porous medium permeability has not been retuned. In the following graphs (Figs. 2.23, 2.24 and 2.25) corresponding $\Delta P(\dot{m})$ curves are shown. Model predictivity with respect to geometry change is very good since – for all the case studied – the pressure drop is reproduced very well in all the cases.

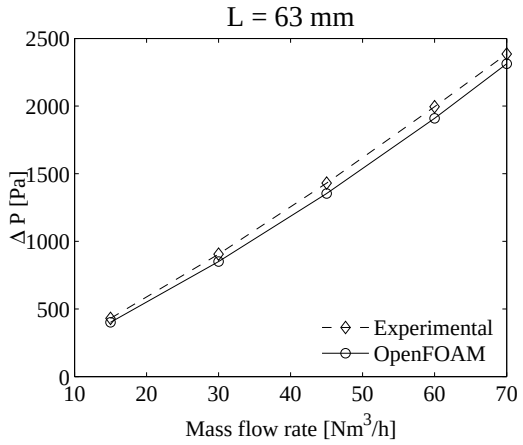

Figure 2.23: Pressure drop versus flow rate for a filter with L=63 mm. Permeability was tuned on the 152 mm case.

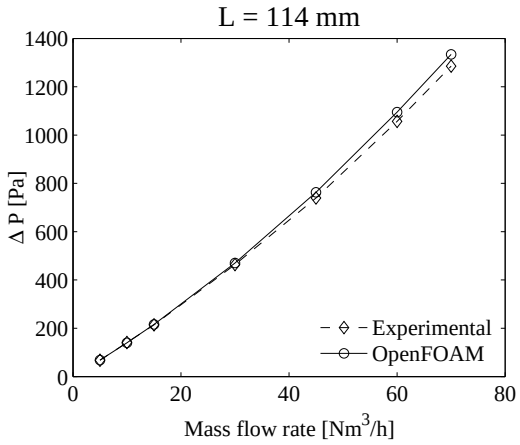

Figure 2.24: Pressure drop versus flow rate for a filter with L=114 mm. Permeability was tuned on the 152 mm case.

2.2 Filter loading

2.2.1 Case setup

Validation of soot transport and deposition model has been done on a simplified model with respect to the full filter geometry. Once the predictivity of the fluid-dynamic model has been assessed (cf. previous section), is it possible to analyze the filtration model on a reduced configuration to speed up the computation. Thus, realistic loading times (i.e., some hours) can be simulated in a reasonable amount of time.

The chosen geometry is a single couple of channels extracted from the same filter type

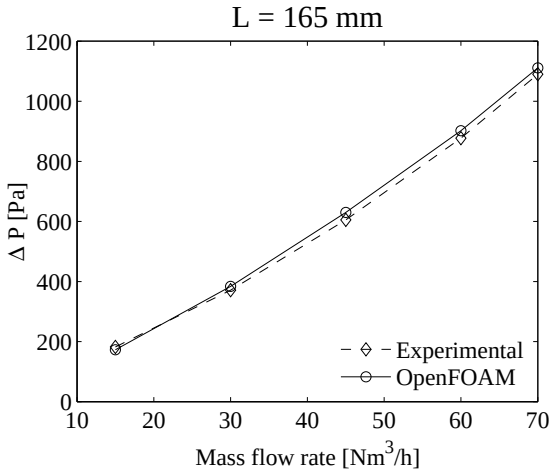

Figure 2.25: Pressure drop versus flow rate for a filter with L=165 mm. Permeability was tuned on the 152 mm case.

of previous section (cf. Tab. 2.1) with a total length of 203 mm, see Fig. 2.26. Test condition are taken from the experimental work of Huynh [41]. Fluid is exhaust gas considered as a prefect, nonreacting mixture (M_m = 29.17 kg/mol, c_p/c_v = 1.35) at a temperature of 548.15 K. Additional filter parameters are listed in tab. 2.2.

Table 2.2: Substrate properties for filter EX-80 described in table 2.1

Porosity [–]	0.48
Mean pore size μm	12.5
Percolation factor Ψ [–]	0.862

In the cited work by Huynh et al. [41], pressure difference between filter inlet and outlet section is plotted against time, for different engine load conditions. Validation of our model has been carried out for one of them, corresponding to 25% of the maximum engine load (311 Nm, 1800 rpm). On table 2.3, exhaust conditions at filter inlet and average characteristics of particulate are listed. Probability distribution function of soot particles diameter is depicted in the figure beside. Even tough the model is potentially able to deal with any type particle distribution, for the preliminary tests a constant diameter has been considered, corresponding to the maximum concentration value.

As mentioned before, a simplified configuration has been chosen to speed up computation time. Only a couple of DPF channels has been modeled, as depicted in fig. 2.26, with a porous wall between inlet and outlet channel. Either symmetry or wall boundary conditions have been set on external surfaces, whereas top and bottom plane (i.e. parallel

Table 2.3: Average properties of exhaust gas and contained soot. PDF of particles diameter is represented on the figure beside.

ex. flow rate [kg/s]	0.223
soot concentration [m/m]	$1.016 \cdot 10^{-5}$
$\Delta P_{\text{clean trap}}$ [Pa]	1160
Particle density [kg/m^3]	2000
Soot layer density [kg/m^3]	117
Soot cake permeability [m^2]	$2 \cdot 10^{-13}$
Mean particle diameter [nm]	100

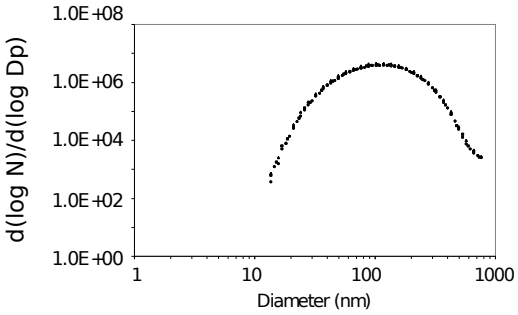

to the drawing plane in fig. 2.26) are of type "empty", that means that flow equations are solved in two dimensions only. Each channel is discretized with one cell in trasverse direction (which is consistent with the fluid-dynamic approach explained before) and 130 cells along the main axis. Inlet velocity of 19.63 m/s (determined from the experimental flow rate) has been imposed on the channel inlet section, while static pressure has been set on the outlet. No frontal area correction is used in this case, since any difference has been accounted *a priori* in calculating the inlet velocity. On the other hand, contraction and expansion losses are added *a posteriori* using the empirical formula adopted for 1D models:

$$\Delta P_{\text{contr+exp}} = (\zeta_{\text{contr}} + \zeta_{\text{exp}}) \rho \frac{U^2}{2} = (0.42 + 0.40) \rho \frac{U^2}{2} \tag{2.3}$$

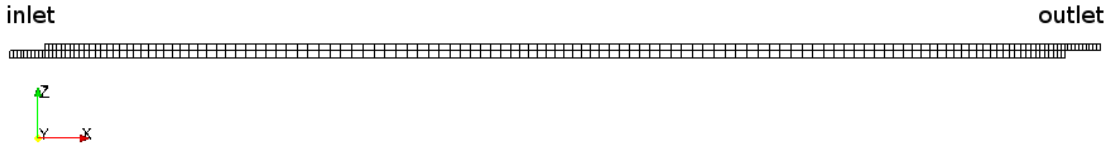

Figure 2.26: FV mesh of the two-channels simplified configuration used to validate the soot transport and deposition model.

2.2.2 Main results

2.2.2.1 Pressure drop

Validation of soot filtration and deposition model with respect to pressure drop is shown in fig. 2.27. Matching between experiments and numerical predictions appears very good along the whole time history, even if a very small underestimation of pressure drop is still

present in the final results. Such a behavior can be explained by the uncertainty in some input parameters, especially those regarding soot macroscopic properties (e.g. particle density, permeability) or porous substrate mean characteristics (e.g. mean pore diameter). Nonetheless, it has been considered preferrable to avoid tuning any additional physical parameter.

At the same time, in fig. 2.28 it is possible to see the soot cake thickness along filter axis for $T = 1$h and $T = 2$h. As expected, soot layer is thicker near the channel ends, where wallflow velocity is greater. It is also worth noting here that overall soot thickness remains very small with respect to channel transverse size, so the proposed approach remains valid at least for similar loading levels.

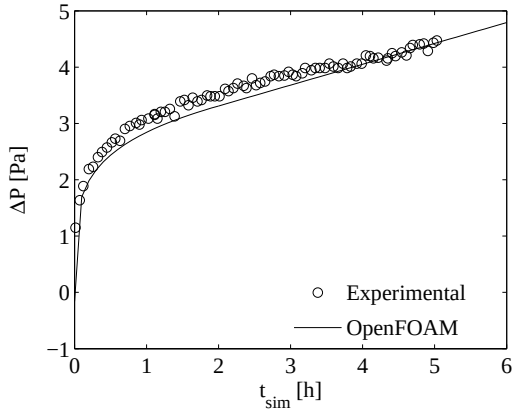

Figure 2.27: Validation of soot transport and deposition model with respect to pressure drop.

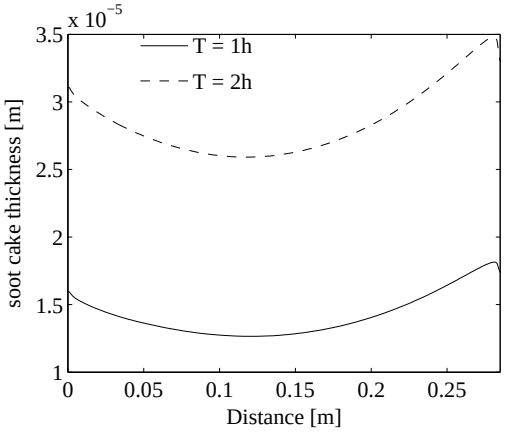

Figure 2.28: Soot cake thickness along filter axis after 1h and 2h of filter loading.

2.2.2.2 Porous medium

Evolution of porous medium filtrating characteristics can be summarized by its two main parameters: filtration efficiency η and partition coefficient ϕ. In figs. 2.30 and 2.29 the change of η and ϕ with time is represented. It is clearly visible that the partition coefficient reaches a value of almost unity at about $t \approx 1.5$h, that is the same point where the linear part of $\Delta P(t)$ begins. At the same time η undergoes a similar trend and its rate of growth decreases steeply when approaching $T = 1.5$h, because the most of collected soot now remains in the outer layer.

2.2.2.3 Velocity field

Profiles of mean velocity along the channel axis and across the porous wall are represented in figs. 2.32 and 2.31 respectively. Evolution of velocity profiles is clearly visible, especially

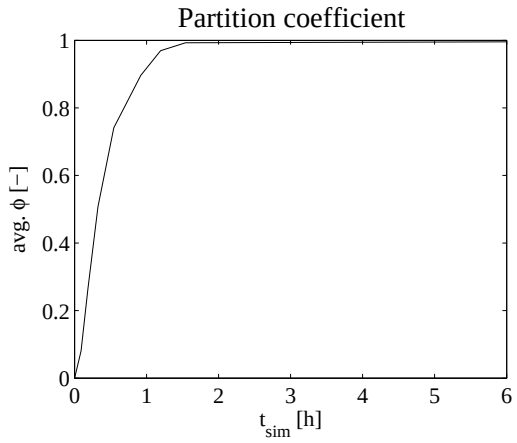

Figure 2.29: Variation of partition coefficient with time. When $\phi \approx 1$ the curve $\Delta P(t)$ becomes linear (fig. 2.27

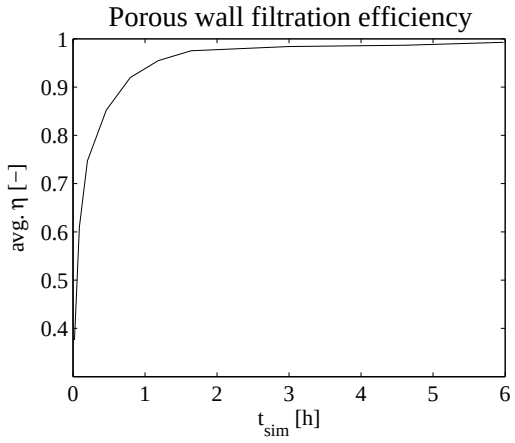

Figure 2.30: Variation of wall filtration efficiency with time.

between $T = 0$ and $T = 1$h: axial velocity approaches a linear profile, while crossflow velocity becomes more and more uniform across the porous wall length. Such a behavior is similar in all aspects to what is described by other authors using different kind of numerical models [65, 41].

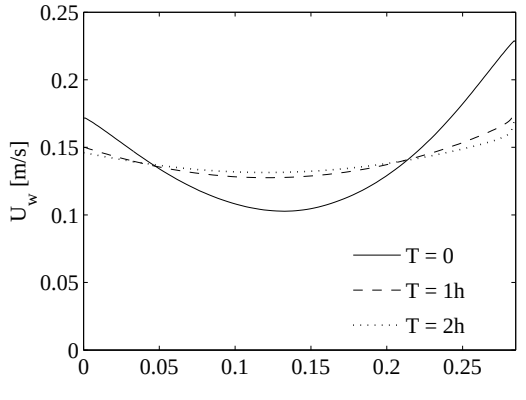

Figure 2.31: Graph of variation of wallflow velocity profile $U_w(z)$ with filter loading. As resistance increases, the curve flattens and the maximum shiftes.

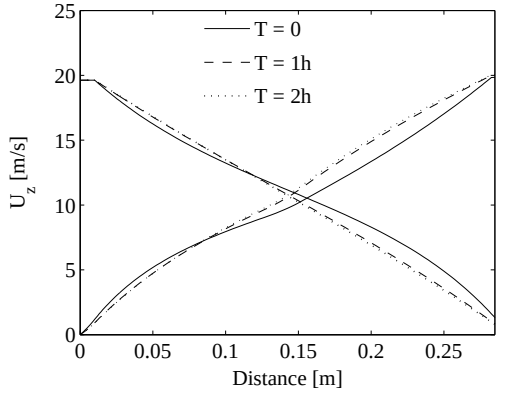

Figure 2.32: Graph of variation of axial velocity profiles $U_{ax}(z)$ with filter loading. As resistance increases, profiles move towards a stronger linear character.

2.2.3 Application to a full scale case

The soot loading and filtration model validated in the previous section does not require any modification or extension if applied to a full scale model, like the one used to validate the

hydro-dynamic part of the solver. However, poor numerical stability of the solver when high flow resistance are encountered (i.e. at medium-high loading levels), renders such a validation a challenging task. At the moment, no complete results are available about loading of a complete filter; nonetheless some partial results that are useful to test the global behavior of the code can be examined. Case setup is the same of section 2.1.1 for what concerns filter geometry and discretization, while substrate and soot properties are taken from the filtration model validation test case (sec: 2.2).

Four snapshot of the very first time steps of loading are represented in figure 2.33. At the beginning, filtration efficiency is low so part of the particulates escapes the filter and goes into the outlet channel. As loading proceeds, soot concentration in the outlet channel tends to a near-zero value.

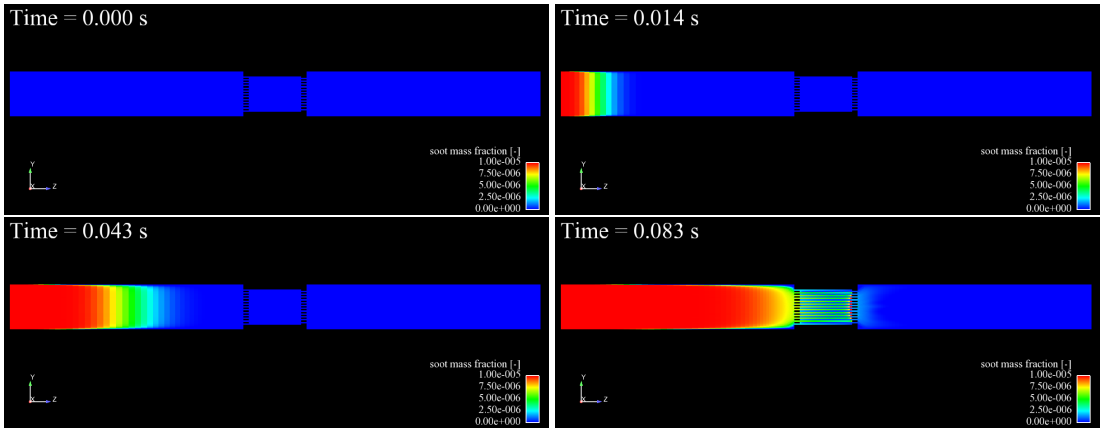

Figure 2.33: Snapshots of soot concentration field at the early times of loading stage.

Soot cake thickness can be seen in fig. 2.34: it is clearly visible that is a local value that can be depent upon the channel position inside the filter. Finally, distribution of porous wall permeability, which is a local quantity as well, can be appreciated in fig. 2.35.

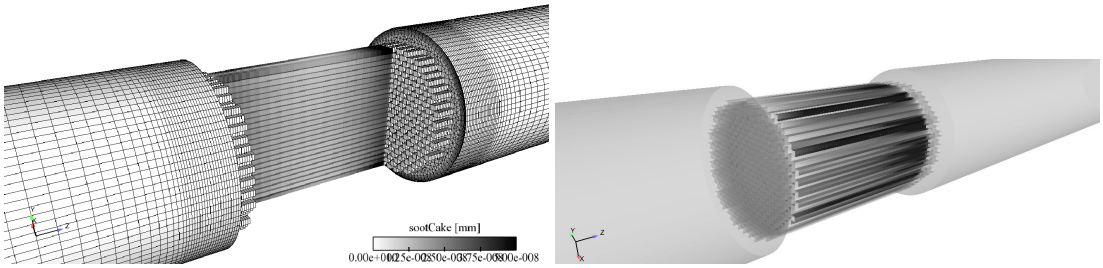

Figure 2.34: Contour plots of soot cake (left) and trapped soot mass (right) during loading

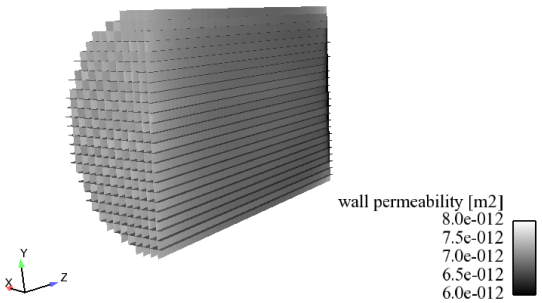

Figure 2.35: Contour plot of local porous wall permeability during soot loading

2.3 Closure

An original approach for simulating Diesel Particulate Filters has been proposed here. Features of our model are the capability of studying full-scale filter geometries inserted in their own duct system (inlet-outlet cones) and, at the same time, the possibility of studying details of flow into the monolith channels. If the porous walls thickness is neglected, the Darcy-Forchheimer porous resistance term can be applied on cell faces as a surface stress. Therefore, it is possible reduce the total number of computational cells and increase their average size, with great benefits in terms of computational cost. Moreover, the mesh generation procedure of the filter monolith can be automatized and a precise and realistic reproduction of the actual filter shape is possible (including, for instance, cement walls between filter segments, or complex shapes). Finally, the filter region belongs to the same fluid domain of the inlet-outlet ducts, so that no domain coupling techniques (that usually limit numerical efficienc) are needed.

Some modifications have to be applied to the momentum equation in the filter region, not only to account for porous resistance terms, but also to include gas-wall friction, differences in Open Frontal Area, and turbulence switch off.

Hydrodynamic solver has been fully validated, both in terms of global quantities (overall pressure drop, flow uniformity on frontal sections), but also with respect to flow details inside the channels. Solver predictivity with respect to geometry changes has been assessed: the only tuned parameters is porous wall permeability, that depends only on the porous wall microstructure and it is independent from the monolith geometry.

Filter loading can be simulated by extending the hydrodynamic model to account for soot transport, deposition and filtration. To speed up computations, soot is considered as a passive scalar which is convected by the fluid. When soot flux is intercepted by porous walls, a certain amount of it is removed from the exhaust flow according to wall filtration efficiency. The classic filtration model by Konstandopoulos and Johnson [51] reproduces changes in

porous wall characteristics (porosity, collection efficiency, permeability) due to soot interception. In turn, changes in permeability modify the Darcy resistance and the global flow fields.

The presence of surface source term inside the momentum and continuity equations requires a particular treatment of main variables (pressure and velocity). Whereas the original OpenFOAM solver uses a colocated approach, a pseudo-staggered approach with a subsequent velocity reconstruction must be employed in this case. This not only requires a modification of the original pressure-velocity coupling algorithm, but it also limits the possibility of inserting implicitly all surface sink terms. For these reasons, numerical properties of the solver are not very good and small timesteps are required for stability. Importance of small timesteps increases with porous wall resistance, so that simulating a complete filter loading, though possible by a theoretical point of view, is unfeasible in practice. Nonetheless, soot transport and deposition model has been validated on a simplified configuration (2-channel mesh) and some partial results of a full-scale filter loading are available.

Chapter 3

Large Eddy Simulations for Internal Combustion Engines

3.1 Motivation

Large Eddy Simulation consists in simulating turbulent flows, that are unsteady by their nature, by means of solving a particular system of PDE, that is obtained by applying a filter to the general Navier-Stokes equations [72].

The main principle of LES lies in *scale separation* between *resolved* and *unresolved* scales. Unresolved (small) scales are not explicitly computed but their energy content is taken into account by means of a closure model named "subgrid model". Larger scales, on the other hand, are fully resolved both in time and space, thus allowing for the study of complex phenomena with strong unsteady characteristics. Among them, gas exchanges cycles in Internal Combustion Engines are for sure a primary candidate.

In fact, despite it can be considered as a steady on a very large time scale, the working principle of an ICE is basically unsteady, like all volumetric machines. The high complexity of phenomena occuring during the gas exchange phase leads to the so-called *cycle-to-cycle* variation (CCV). Even when average working conditions (speed, load, ambient pressure and temperature, etc.) are kept constant, small random variations in gas exchange and combustion processes lead to sensible effects on engine output. Each working cycle is different from the others and such statistical variations are generally not negligible with respect to the total output. Thus, it is of foremost interest to be able to predict cycle-to-cycle variations, at least with respect to some statistics.

Turbulent motion of fluids, that occurs during all stages of an engine working cycle, is probably the most important source of randomness. Therefore, prediction of CCV is strongly connected to accurate time-resolving of turbulent scales, that is where LES gets into play.

3.1.1 Previous works in the field

First large-eddy simulations were performed in the early 1970s for the purpose of simulating the atmospheric boundary layer. Application of LES to Internal Combustion Engines is a relatively recent topic. One of the leading work in this field was done by Haworth [38], who simulated the gas motion into a simplified cylinder configuration with moving mesh, and demonstrated the capability of LES to reproduce higher-order statistics of flow field.

Later works by Thobois et al. [83, 84] succeeded in simulating both simplified configurations and real engine geometries with a limited number of cells, obtaining good results in terms of mean flow quantities. Finally, significant results towards prediction of CCV on real cylinder geometries were obtained by Hasse et al. [37] using a hybrid URANS/LES approach.

3.1.2 Scope of this work

The present work aims to investigate the influence of the inlet boundary condition on a standard test case. Case geometry and numerical setup are presented in detail in chapter 3.5, together with experimental reference data. It is anticipated here that the chosen case is number 83 of the ERCOFTAC database ("wall-mounted hump"). Though it does not have any connection with ICE components, nonetheless it can be thought as representative of typical fluid-dynamic problems that comes out in such a field, namely, a combination of channel flow and separation.

Being a standard test-case, some LES investigations on this case already exist. Among others, we recall here the work by Šaric [89] and You [95]. Both of them successfully simulated the proposed case, the former with a classic Smagorinsky model, the latter with the dynamic one. Also, good results were obtained by Morgan using Implicit LES [60] and by Krishnan by means of Detached Eddy Simulation [55]

In this chapter, main definitions about LES are briefly recalled, to serve as a basis for later considerations. At the same time, some important consequences of LES procedures are presented, to be used in the later results analysis.

3.2 Mathematical background

Let $\mathbf{u}(\mathbf{x}, t)$ be the solution of a Navier-Stokes problem in a space-time domain. Analogously, let $\mathbf{U}(\kappa, f)$ be the same solution as seen in a wavenumber-frequency domain. If the flow field is turbulent, $\mathbf{U}(\kappa, f)$ has a spectral content in the range $\kappa = 0 \ldots \kappa_{\max}$. Let us suppose to apply a lowpass filter operator $G(\kappa_c)$ (with κ_c as cutoff frequency) to the exact solution: the filtered field $\overline{\mathbf{U}} = G(\kappa_c)\mathbf{U} =$ will have a lower frequency content with respect to the unfiltered one.

In other words, applying a filter operator cuts out the smallest scales of turbulence, that are most demanding to determine in terms of computational costs.

Mass and momentum conservation equations can be written for the filtered field by applying the filter operator to the original Navier-Stokes system. In the incompressible case, the result takes the form of Eq. (3.1) and (3.2) .

$$\frac{\partial \overline{\mathbf{u}}}{\partial t} + \nabla \cdot (\overline{\mathbf{u}}\,\overline{\mathbf{u}}) = -\frac{\nabla \overline{p}}{\rho} + \nabla \cdot \left[\nu \frac{1}{2} (\nabla \overline{\mathbf{u}} + \nabla \overline{\mathbf{u}}^T) \right] + \nabla \cdot \boldsymbol{\tau} \tag{3.1}$$

$$\nabla \cdot \overline{\mathbf{u}} = 0 \tag{3.2}$$

In a FV framework, this filtering is applied implicitly by the computational mesh: in other words, scales smaller than the cell size can never be resolved, so a lowpass filter is always present. Nonetheless, their energy content has to be accounted in the conservation equations to correctly reproduce the energy cascade process from largest to smallest scales. The filter characteristic length is assumed to be some quantities related to the cell size. Usually, it is calculated as $\bar{\Delta} = V^{1/3}$

The quantity $\boldsymbol{\tau}$ appearing on the RHS of the momentum equation is known as *subgrid tensor* and it represents the momentum contribution of the unresolved (subgrid) scales. It is defined as: $\boldsymbol{\tau} = \overline{\mathbf{U}\mathbf{U}} - \overline{\mathbf{U}}\,\overline{\mathbf{U}}$ and it is unknown *a priori*, thus it has to be modeled by some closure equation that is called *subgrid model*.

3.2.1 Modeling the subgrid stresses

Model equations for $\boldsymbol{\tau}$ can be divided into two main classes: eddy-viscosity models and scale-similarity models. Beside them, there lie mixed models (a combination of eddy-viscosity and scale-similarity) and implicit SGS modeling.

3.2.1.1 Eddy-viscosity models

The most common class of subgrid models are based on the eddy-viscosity hypothesis: energy transfer mechanism from the resolved to the subgrid scales is supposed to be analogous to the molecular mechanisms represented by the diffusion term, in which the viscosity ν appears. The subgrid model can thus be written as:

$$-\nabla \cdot \boldsymbol{\tau}^{\boldsymbol{d}} = \nabla \cdot \left[\nu_{sgs} (\nabla \overline{\mathbf{u}} + \nabla \overline{\mathbf{u}}^T) \right] \tag{3.3}$$

where $\boldsymbol{\tau}^{\boldsymbol{d}} = \boldsymbol{\tau} - \mathrm{tr}(\boldsymbol{\tau})$ is the deviatoric part of $\boldsymbol{\tau}$.

Under the eddy-viscosity hypothesis, the closure problem reduces to calculating the subgrid viscosity ν_{sgs} from some known flow quantities. Again, relations for calculating ν_{sgs} can be divided into two classes: Smagorinsky-type and kinetic-energy based.

To the former type belong models that have the following form of the SGS viscosity [77]:

$$\nu_{sgs} = (C_s\bar{\Delta})^2 \left\langle 2|\overline{S}|^2 \right\rangle^{1/2} \tag{3.4}$$

where $|\overline{S}|^2 = S_{ij}S_{ij}$ and $S_{ij} = 1/2(\partial u_i/\partial x_j + \partial u_j/\partial x_i)$ is the filtered rate-of-strain tensor. Model coefficient C_s can be determined by theoretical reasoning or it can be computed using a theoretical procedure based on Germano's identity [29].

To the second class of SGS models belong those that write ν_{sgs} as a function of the subgrid kinetic energy $k_{sgs} = 1/2\overline{\left((\mathbf{u}-\overline{\mathbf{u}})\right)}$. In this context, ν_{sgs} is obtained by:

$$\nu_{sgs} = C_m\bar{\Delta}k_{sgs}^{1/2} \tag{3.5}$$

Again, the coefficient C_m can be inferred *a priori* or it can be computed dynamically [45, 46]. On the other hand, k_{sgs} cannot be calculated from known quantities, so a conservation equation has to be solved:

$$\frac{\partial k_{sgs}}{\partial t} + \bar{u}_i\frac{\partial k_{sgs}}{\partial x_i} - \frac{\partial}{\partial x_i}\left(D_k\frac{\partial k_{sgs}}{\partial x_i}\right) = \mathscr{P} - \varepsilon \tag{3.6}$$

where $\mathscr{P}$ is a production term and ε is the kinetic energy dissipation rate.

3.2.1.2 Scale-similarity models

In scale-similarity models the total subgrid stress is decomposed as:

$$\begin{aligned}
\overline{\mathbf{u}\mathbf{u}} - \overline{\mathbf{u}}\,\overline{\mathbf{u}} &= \overline{(\overline{\mathbf{u}}+\mathbf{u}')((\overline{\mathbf{u}}+\mathbf{u}'))} - \overline{\mathbf{u}}\,\overline{\mathbf{u}} \\
&= \overline{\overline{\mathbf{u}}\,\overline{\mathbf{u}}} + \overline{\overline{\mathbf{u}}\,\mathbf{u}'} + \overline{\overline{\mathbf{u}}\,\mathbf{u}'} + \overline{\mathbf{u}'\mathbf{u}'} - \overline{\mathbf{u}}\,\overline{\mathbf{u}} \\
&= (\overline{\overline{\mathbf{u}}\,\overline{\mathbf{u}}} - \overline{\mathbf{u}}\,\overline{\mathbf{u}}) + \left[\overline{\overline{\mathbf{u}}\,\mathbf{u}'} + \overline{\overline{\mathbf{u}}\,\mathbf{u}'}\right] + \overline{\mathbf{u}'\mathbf{u}'}
\end{aligned}$$

The three terms in brackets on the RHS are called, respectively, Leonard tensor, Cross tensor and Reynolds tensor. They represents, respectively, interactions between large scales, between large and small scales and between small scales:

$$\begin{aligned}
\boldsymbol{\tau} &= \boldsymbol{L} + \boldsymbol{C} + \boldsymbol{R} \\
\boldsymbol{L} &= (\overline{\overline{\mathbf{u}}\,\overline{\mathbf{u}}} - \overline{\mathbf{u}}\,\overline{\mathbf{u}}) \\
\boldsymbol{C} &= \left[\overline{\overline{\mathbf{u}}\,\mathbf{u}'} + \overline{\overline{\mathbf{u}}\,\mathbf{u}'}\right] \\
\boldsymbol{R} &= \overline{\mathbf{u}'\mathbf{u}'}
\end{aligned}$$

The underlying idea of scale-similarity models is that small scales just above cutoff are essentially similar to scales just below, so that energy transfer can be represented by the cross

tensor. Thus, modeling reduces in finding an expression for $\boldsymbol{C}$, that is usually modeled as [7, 8]

$$\boldsymbol{C}^M = C_r(\overline{\mathbf{u}}\,\overline{\mathbf{u}} - \overline{\bar{\mathbf{u}}}\,\overline{\bar{\mathbf{u}}}) \tag{3.7}$$

while $R^M = 0$.

Since the original Bardina's model is not sufficiently dissipative, a Smagorinsky term is added, and the final expression of the subgrid tensor is:

$$\boldsymbol{\tau} = C_r(\overline{\mathbf{u}}\,\overline{\mathbf{u}} - \overline{\bar{\mathbf{u}}}\,\overline{\bar{\mathbf{u}}}) - 2(C_s\bar{\Delta})^2\left\langle 2|\overline{S}|^2\right\rangle^{1/2} \tag{3.8}$$

3.2.1.3 Implicit LES

It is a well-known fact that some limited schemes for discretization of convection terms introduce a truncation error that is proportional to the second derivative of velocity. In other words, limited schemes act by adding an artificial dissipation to the flow [40]. Moreover, it has been seen that order of magnitude of artificial dissipation is the same of the subgrid viscosity.

Therefore, it is theoretically possible to avoid any explicit subgrid modeling and account for energy transfer at small scales by numerical dissipation. Such a method is called *implicit LES* (ILES) [28].

The only difficulty of ILES is to find an expression to evaluate ν_{sgs} *a posteriori*, in order to separate scheme- and grid- related effects. Generally speaking, ILES is used mainly in fields where uncertainty about details of physics is quite high (e.g. combustion) and robustness and ease of implementation is preferred over accuracy [72].

3.2.1.4 Detached Eddy Simulation and Hybrid LES-URANS

A final word has to be said about most recent advances in this field. One of the greatest requirements in terms of grid size, that is encountered when performing LES, is related to solid walls. In fact, the complex dynamic of near-wall structures puts DNS-like requirements on cell size near the wall. LES of complex geometries at high Reynolds numbers (e.g. for external aerodynamics) becomes nearly impossible.

On the other hand, RANS procedure for wall-bounded flows is well estabilished and, though less detailed, it is based on strong theoretical basis. The idea about Detached Eddy Simulation (DES) or hybrid LES-URANS is to solve the time-resolved filtered equations in the bulk domain, and to use URANS near the wall.

The only significant difference between DES and hybrid LES-URANS is that, in the former, the URANS approach is applied only in the first cell layer, while in the latter there is a larger zone where URANS is applied, and some criteria are needed to switch from one model

to another [20]. Moreover, there are some SGS models like Spalart-Allmaras that naturally produces a DES when applied to an unsteady Navier-Stokes problem [80].

3.2.2 Closure

Various classes of subgrid models used for large-eddy simulations in a finite volume context have been briefly presented. The coverage has been purposely concise and far from completeness, since it serves only to support later considerations rather than to provide extensive information about LES.

Introductory concepts to LES principle allows for formulating some general considerations about modeling issues that arise when doing practical work. In the next section, some of them will be presented, in particular: discretization schemes, mesh requirements, inlet boundary conditions.

About SGS models, it has to be said that the present study will be carried out having the eddy-viscosity paradigm as a general reference. It has been chosen so, because, to our opinion, it represents a good compromise between simplicity and the necessity to have some degree of control on the subgrid viscosity. Implicit LES would have been equally simple and robust to apply, but with little or no control on how the subgrid viscosity is generated, thus the influence of the SGS model on the results could not be studied.

3.3 Practical aspects of LES

3.3.1 Discretization schemes

The previous paragraph about ILES (3.2.1.3) introduced the problem of artificial dissipation generated by the truncation error of discrete NS equations. Though numerical viscosity can be exploited to carry out implicit SGS modeling, it is nonetheless a serious issue when an explicit SGS model is applied. For this reasons, LES best-practice guidelines suggests to always use a non-dissipartive second-order scheme to discretize the momentum advection term.

In particular, the use of a pure-upwind scheme would generate numerical errors that would overwhelm any subgrid term, thus rendering LES nearly unusable. Also, second-order limited schemes must be applied with caution, for artificial dissipation may be introduced as well. In the end, one of the less problematic schemes is the pure centered differencing scheme, that has no second-order terms in its truncation error. Thus, its effect on the discrete solution is purely dispersive.

On the other hand, stability is often compromised when centered differencing is used in a convection-dominated problem. Thus, temporal integration step has to be kept as low as

possible to guarantee stability of the solution.

Use of higher-order methods would be for sure advisable, since it increases the accuracy of the whole solution. Unfortunately, FV methods can guarantee at most a second order accuracy, provided at least second order schemes are used for differencing [43].

3.3.2 Mesh requirements

Influence of computation grid on discrete solution is twofold. On one hand, there are discretization errors related to FV formulation. In this context, poor mesh quality negatively affects the quality of the results, no matter which discretization scheme is chosen. It has been shown that poor meshes can introduce in the solution both second-order (dissipative) and third-order (dispersive) errors [43]. Moreover, cell shape has a similar influence on the results, even though the mesh is generated virtually free of any issue. Juretić [44] demonstrated that the best cell shape is a uniform cartesian mesh. Skewed, non-orthogonal and stretched meshes, as well as unstructured tetrahedral ones, are preferably to be avoided when performing LES, due to its sensitivity to numerical errors.

The other cause of error is connected with the implicit filtering: solving fluid-dynamics equations on a discrete grid always imply to cut smaller scales that cannot be resolved because of the finite cell size. As a consequence, the behavior of subgrid model change with mesh resolution and, in an ideal case, a LES tends to a DNS as cell sizes tend to the smallest length, i.e. the Kolmogorov scale. In this sense, discretization errors are connected to lack of resolution of turbulent scales. A number of works exist on this topic and several methods have been proposed to estimate LES quality on the basis of resolved quantities. Some techniques are based on global estimators like resolved kinetic energy [66]; others uses more complex parameters based on resolved kinetic energy, dissipation and numerical viscosity [14, 13, 49, 30]; moreover, local estimators are available, that are based on ratio of resolved lengths to Kolmogorov scales [11] or correlation function [19]. At the moment, the problem is still open.

Only for near-wall resolution, some practical criteria have been identified to express minimum resolution in wall units [58]. Along wall-normal direction, the reccomended resolution is such that the first mesh point lies in the range $0 \leq y^+ \leq 1$ (being (x, y, z) the streamwise, wall-normal and spanwise coordinates respectively, and the apex '$^+$' represents wall-unit scaling). Moreover, streamwise and spanwise resolution have to be contolled as well. Shumann (cited by [72]) reccomends $\Delta x^+ < 10$ and $\Delta z^+ < 2$ for a complete reproduction of near-wall dinamycs. However, other authors indicated less severe requirements for Δx^+ and Δz^+.

3.4 Inlet boundary conditions for LES

Another typical difficulty in LES, especially for some types of flow, is to accurately represent the turbulence characteristics at the domain inflow. In fact, unlike RANS simulations where only mean quantities can be specified, in LES the inlet space-time modes have to be reproduced as completely as possible. Failing to do so, would result in introducing severe sources of error into the computation.

In practice, less strict requirements have to be satisfied. The purpose of inlet turbulence can be regarded as to reproduce some salient turbulent characteristics, rather than reproducing a turbulent fields under all aspects. In particular, the following traits can be identified [82]:

- Stochastic variation (up to filter scale)
- Compatibility with continuity equation (i.e. being divergence-free)
- 'Resemblance' to turbulence
- Ease of turbulence specification
- Ease of implementation and adjustement

Mainly, there are three family of techniques to generate appropriate inlet conditions for LES: precursor DNS, mapping from internal field, synthetic turbulence generation.

3.4.1 Precursor DNS

A Direct Numerical Simulation can be run to generate a library of data that possess some relevant features of the required field, like temporal and spatial fluctuation with correlation and a correct energy spectrum. The library can be generated, for example, by boxes of isotropic turbulence, periodic channel flow, and so on. Data taken from the library are imposed on the inlet of the final computation domain to provide inflow conditions. The Reynolds number does not have to be the same of the final case. It is only sufficient that the appropriate turbulent scales are present, so that they can quickly develop into eddies during LES.

Precursor method is very fundamental since it puts 'real' turbulence into the domain. However, as one can imagine, it is quite demanding in terms of library generation, so it is seldom used for applied research.

3.4.2 Internal field mapping

Instead of generating a turbulent velocity field in some external domain, it can be taken from some region of the solution where turbulence had got time to develop up to a certain degree.

This is the basic idea of internal field mapping, that is graphically represented in fig. 3.1 with reference to a channel flow case. Velocity, together with other relevant variables like subgrid viscosity and kinetic energy, is sampled from a plane that is located at some length downstream of the inlet and remapped onto the inlet itself. Turbulence is initiated into the flow according to the prevailing mechanism that belongs to the specific flow type: in case of channel flow, this is near-wall dynamics. Also, velocity is scaled by some factor to guarantee a constant flow rate across the inlet [21].

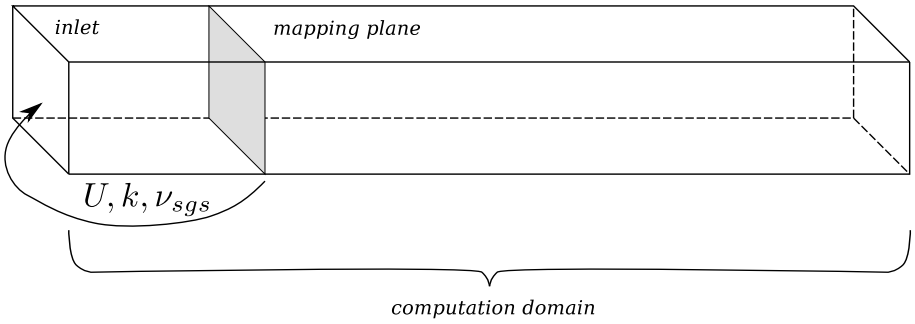

Figure 3.1: Working principle of internal mapping inlet BC. Flow field is sampled on the gray plane and remapped onto the inlet, with some scale adjustment.

The main advantage of such a technique is that actual turbulence is imposed on the inlet, provided that the choice of mapping location is appropriate and space discretization is correct. Moreover, no setup parameters are needed, so specification is easy and it can be applied on nearly all types of flows of engineering interest.

Disadvantages of this technique includes the time required to allow turbulence to develop between inlet and mapping plane and, in some cases, the additional domain that has to be added to create such a mapping region. A comprehensive coverage of plane mapping procedures can be found in the review paper by Baba-Ahmadi and Tabor [6].

3.4.3 Synthetic turbulence generation

The last family of inflow conditions presented here includes all techniques for generating *a priori* a fluctuating field that "looks like" turbulence, even though it has only some properties of true turbulence. Adding a random noise to the average velocity would not work in this case. In particular, the following characteristics have to be preserved:

- Solenoidality of fluctuations, otherwise they would be destroyed by the Navier-Stokes solver
- Spectral content corresponding to the flow problem that has to be simulated

- Space and time correlation

The basic concept is that fluctuations are generated by adding N random Fourier modes (with wavenumber $\kappa_j = \kappa_1 \dots \kappa_N$) using an expression like Eq. (3.9):

$$u_i''(x_j) = 2\sum_{n=1}^{N} \hat{u}^n \cos\left(\kappa_j^n x_j + \psi^n\right)\boldsymbol{\sigma}_i^n \tag{3.9}$$

Different algorithms for producing required quantities are proposed in the literature. Here, it is presented the synthetic turbulence inlet method by Davidson [18].

Vectors κ_j have unity magnitude, and direction is chosen according to random angles (ϕ_n, θ_n), see fig. 3.2-a. Wavenumber velocity vector $\boldsymbol{\sigma}_i$ lies in a plane (ξ_1, ξ_2) that is always orthogonal to κ_j, and it is oriented according to a third random angle α_n, see fig. 3.2-b. Being $\boldsymbol{\sigma}_i^n$ orthogonal to κ_j^n guarantees that fluctuations u_i'' are divergence-free, that is, they ensure mass conservation and thus they are not smoothed out by the Navier-Stokes solver.

Density function of α_n, θ_n and ϕ_n are reported in tab. 3.1; ψ_n denotes the random phase angle of the n^{th} mode.

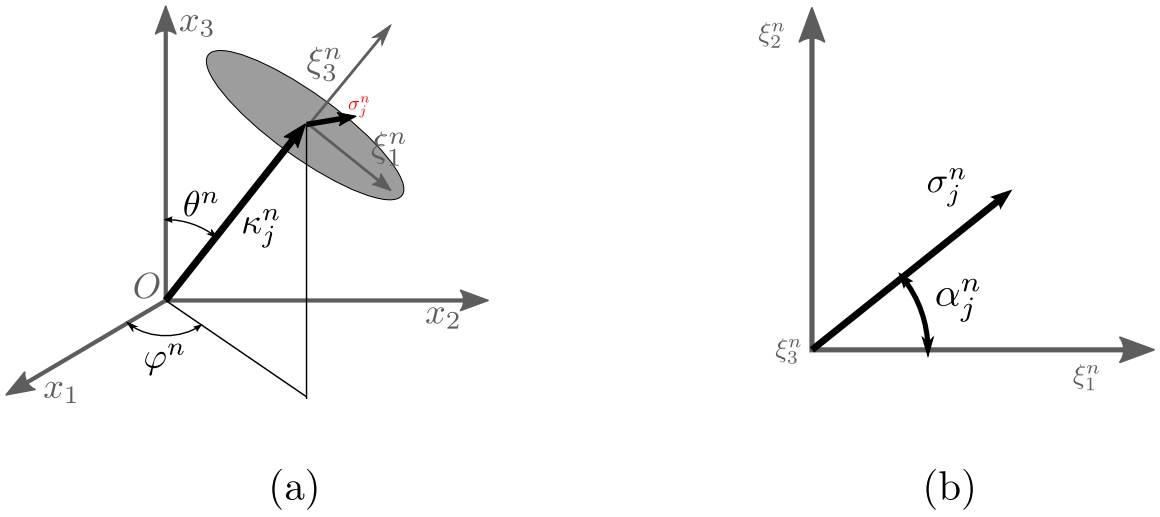

Figure 3.2: Random angles used in the synthetic turbulence generation. (a) orientation of wavenumber vector according to (ϕ, θ); (b) orientation of vector $\sigma_\mathbf{j}$ on the plane (ξ_1, ξ_2)

.

Amplitude $\hat{u}_n$ of each mode is computed according to a modified Von Kármán energy spectrum, that is represented in fig. 3.3 and whose expression is given in Eq. (3.10).

$$E(\kappa) = A\frac{u_{rms}^2}{\kappa_e}\frac{(\kappa/\kappa_e)^4}{\left[1+(\kappa/\kappa_e)^2\right]^{17/6}}\exp\left[-2(\kappa/\kappa_\eta)^2\right] \tag{3.10}$$

where:

Table 3.1

$\mathscr{P}(\phi_n) =$	$[1/(2\pi)];$	$0 \le \phi_n \le 2\pi$
$\mathscr{P}(\theta_n) =$	$[1/\sin\theta];$	$0 \le \theta_n \le \pi$
$\mathscr{P}(\alpha_n) =$	$[1/(2\pi)];$	$0 \le \alpha_n \le 2\pi$
$\mathscr{P}(\psi_n) =$	$[1/(2\pi)];$	$0 \le \psi_n \le 2\pi$

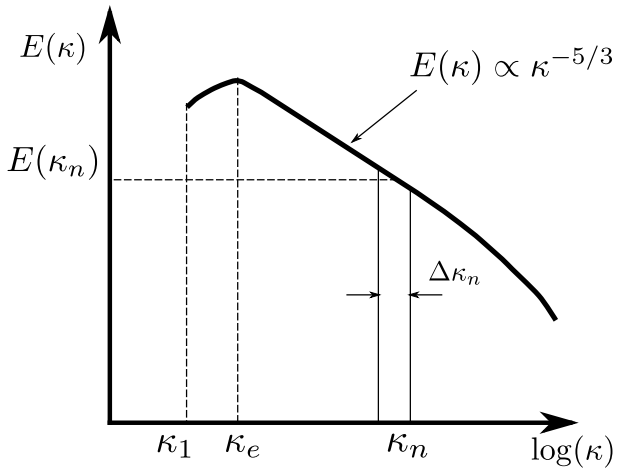

Figure 3.3: Generic shape of the modified Von Kármán spectrum whose expression is given in Eq. (3.10)

- $\kappa_\eta = \varepsilon^{1/4}\nu^{-3/4}$ is the maximum wavenumber, corresponding to Kolmogorov lengthscale
- $A = 1.456$ is a model's constant
- $\kappa_e = 9\pi/55\ A/\mathscr{L}$ is a function of the integral lengthscale ($\mathscr{L}$).

Having κ_n a uniform distribution with spacing $\Delta\kappa$, corresponding amplitude is $\hat{u}_n = \left[E(|\kappa_j|)\Delta\kappa\right]^{1/2}$.

Once the 'raw' fluctuations $u_i'(\mathbf{x}, t)$ are generated, they need some postprocessing before they can be added to the average field $\langle\mathbf{u}(\mathbf{x}, t)\rangle$ to give the final inlet velocity $\mathbf{u} = \langle\mathbf{u}(\mathbf{x}, t)\rangle + u'$. First, temporal correlation must be enforced, and this task is achieved by means of Billson's temporal filtering [10]:

$$\left(u'\right)^m = a\left(u'\right)^{m-1} + b\left(u''\right)^m \tag{3.11}$$

where ($\mathscr{T}$ is the integral timescale):

$$a = \exp\left(-\Delta t/\mathscr{T}\right), \qquad b = \sqrt{1-a^2}$$

Secondly, a blending function f_{bl} is applied to give the final value of fluctuations to be added to the average velocity:

$$\mathbf{u}(\mathbf{x}, t) = \langle \mathbf{u}(\mathbf{x}, t) \rangle + f_{bl} \cdot \mathbf{u}'(\mathbf{x}, t) \tag{3.12}$$

The purpose of the blending function is to limit freestream turbulence and to blend fluctuations close to the wall. Its expression writes:

$$f_{bl} = \max \left[0.5 \tanh \frac{|\mathbf{n}| - \delta}{b}, f_{max} \right] \tag{3.13}$$

where $|\mathbf{n}|$ is the distance from wall, δ is the boundary layer thickness, b is a coefficient controlling the blending function slope, and f_{max} the clipping value, that usually is set to 0.1.

The synthetic turbulence method requires perhaps less time than the mapping plane for turbulence to develop into the flow. However, an additional computational load has to be accounted for the step of turbulence generation. Depending on the inlet size, the total CPU time might increase up to 10%. Moreover, quite a deep level of detail is required about the inlet turbulence characteristics. In particular, integral length- and time- scales, together with turbulent kinetic energy, have to be specified in order to built the desired spectrum shape. In lack of precise experimental data, this can be done with accurate RANS simulation, that however extend the time required for case setup. On the other hand, it must be noted that, rather than 'actual' turbulence, synthetic fluctuations must be regarded as 'switches' that contribute in early initiation of turbulence into the flow.

3.5 Case setup

3.5.1 Geometry

Test case used for tuning and validation of OpenFOAM LES models is number 83 of the ERCOFTAC database: "Wall-mounted hump" [23]. A modified Glauert Hump body, consisting in a 2D profile with a convex hill on the fore of it, and a concave ramp on the downstream part, is mounted on a splitter plate and the whole is placed into a flow tunnel (see fig. 3.4). Air at ambient conditions (T = 298 K, p at sea level) flows over the body at Ma = 0.1, producing separation and a recirculation region. Detailed geometry and reference data can be found in the work by Greenblatt et al. [33, 34] and summarized here.

All lengths in fig. 3.4 and in the following paragraphs are given as multiples of the chord length c = 0.42 m and the origin of the cartesian reference system is conventionally located at hump leading edge. Geometry is essentially 2D, but 3D effects might occur near the side walls. However, measuerements are taken at the span-center line, so that mean flow field is expected to be 2D.

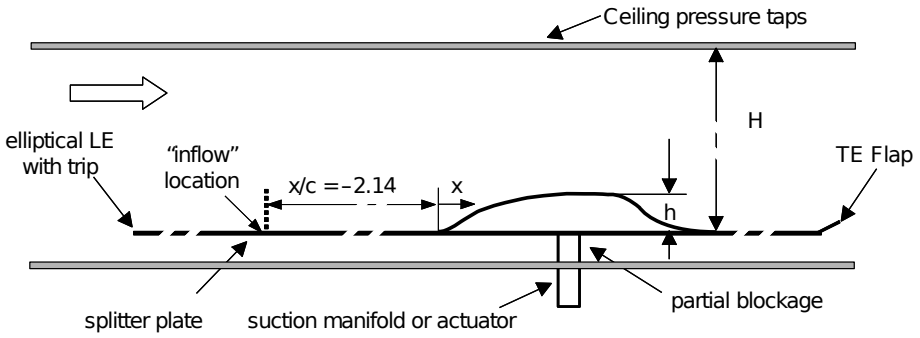

Figure 3.4: 2D sketch of the experimentlal apparate. Simulated domain ranges from $x/c = -2.14$ to the end of the domain, with exclusion of the trailing edge flap.

Tunnel dimensions at test section are 28 inches wide (0.7112 m) by 20 inches tall (0.504 m). The hump is mounted on a split plate that extends 76.188 inches (1.952 m, $x/c = 4.64$) downstream the model's leading edge and 44.437 inches upstream (1.129 m, $x/c = 2.68$). Nominal test section at the split plate is therefore $H = 382$ mm. The simplified geometry used in the calculations is shown in fig. 3.5. Computational domain extends for 2.14 chord lengths upstream of the hump leading edge and for 4 chord lengths downstream. Blockage effects given by the side walls can be accounted for by reducing the channel heigth near the hump, as in fig. 3.5. This way the correct freestream velocity is recovered.

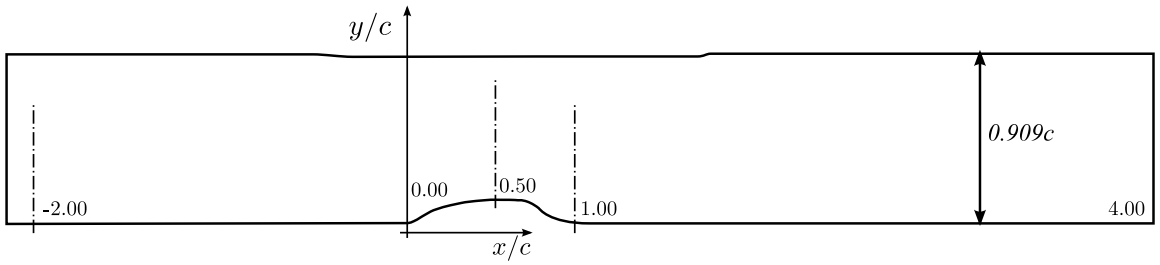

Figure 3.5: Side view of the simulated domain, with main dimensions indicated as multiples of chord length. Spanwise length is 0.2 c

3.5.2 Flow conditions

The cross section located at $x/c = -2.14$ is taken as reference "inflow" section and all inlet conditions for later case setup are measured in this point. Air Mach number is $Ma = 0.10$, corresponding to a freestream velocity $U = 34.6$ m/s; Reynolds number, calculated with the channel height, is $Re = 9.36 \cdot 10^5$. Flow regime is incompressible and fully turbulent: constant density Navier-Stokes equations does apply in this case.

3.5.3 Goal and scope of the work

The goal of the original test case was to study separation control techniques by means of a transverse slot located at $x/c = 0.65$. Either constant suction or alternate suction/blowing with zero net mass flux was applied to the slot to control the size of the separation bubble.

In this study, only the baseline case with no suction nor blowing is studied. Experiments have shown that when no separation control is activated (i.e., there is no suction nor blowing), influence of the slot is negligible. Virtually no difference in pressure trends along the hump (both mean and fluctuating) exists between a sealed and an open slot. Therefore, for simplicity, no slot is modeled along the hump profile.

Purpose of this work is to check the predictive capabilities of OpenFOAM with respect to a complex LES test case like the one presented a while ago. In particular, we will try to reproduce the characteristics of separation region, in terms of mean velocity and turbulence levels, for the 'baseline' case, i.e., with no separation control methods.

3.5.4 Reference data

3.5.4.1 Inlet conditions

Inflow section for simulations has been located at $x/c = -2.14$ (fig. 3.4) by convention. Turbulent boundary layer has been tripped by a thin layer of sand on the leading edge of the splitting plate; therefore, at the conventional inflow section, the flow regime can be regarded as fully turbulent. In fig. 3.6 the scaled mean velocity profile on the inlet is represented. Experimental data are taken by means of a Pitot probe, so a low accuracy is expected for measurements close to the wall.

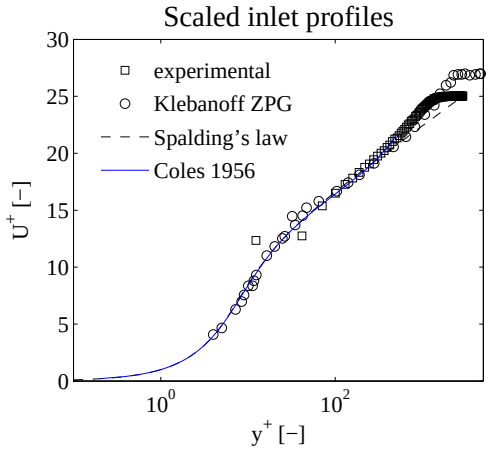

Figure 3.6: Comparison of experimental inlet velocity with some standard profiles. Best fit is obtained with Van Driest law with wake correction.

Experimental profile of fig. 3.6 is compared against some typical curves of velocity profiles in boundary layers (fig. 3.6: Spalding's universal law [81], Van Driest's law with wake correction [16], boundary layer measurements on a flat plate by Klebanoff [48]. Experimental data are not resolved neither in the viscous nor in the buffer zone, so a comparison can be made only in the log-law region. Here, the best approximation for measurements is Van Driest's semi-empirical law with wake correction, that is also the best approximation to the flat-plate boundary layer reported by Klebanoff. For these reasons, the inlet conditions can be assimilated to something in between channel flow and developing boundary layer on a flat plate.

3.5.4.2 PIV data in the separation region

Mean and fluctuating velocities have been measured in the separation region by means of the PIV technique. Globally, four blocks of data were acquired, covering approximately the recirculation region from a short distance upstream of the separation point to some lengths downstream of the separation ($x/c \approx 1.4$). Regions used for PIV are depicted in fig. 3.7. There is a small gap between region #1 and #2, whereas regions #2, #3 and #4 partially overlap. Moreover, zone #2 has a region that is *inside* the hump body: obviously data lying there are without any significance.

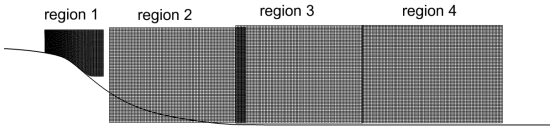

Figure 3.7: Domain covered by PIV measurements.

Mean velocity field is represented in fig. 3.8 and mean turbulent stress levels $\langle u'u' \rangle$, $\langle u'v' \rangle$, and $\langle v'v' \rangle$are depicted in fig. 3.9, 3.10, and 3.11 respectively. PIV data of turbulent stresses comes along with an high degree of uncertainty, that is up to 40% on $\langle u'u' \rangle$and up to 14% on $\langle u'v' \rangle$and $\langle v'v' \rangle$[23]. Following the ERCOFTAC guidelines, these data will be used for qualitative comparisons only.

3.5.4.3 Wall pressure coefficient and shear stress

Pressure coefficient along the hump is represented in fig. 3.12. It has been obtained from direct measuring of pressure by static ports placed over the hump surface.

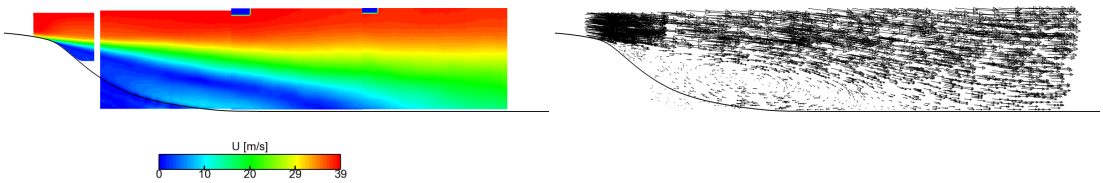

Figure 3.8: Mean velocity field measured by means of PIV. Left: contour plot of velocity magnitude; right: arrow glyph.

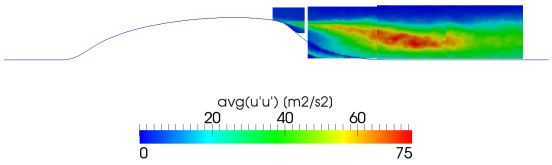

Figure 3.9: Contour plot of streamwise Reynolds stresses $\langle u'u' \rangle$measured by PIV

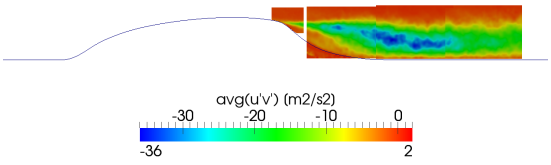

Figure 3.10: Contour plot of shear Reynolds stresses $\langle u'v' \rangle$measured by PIV

Wall shear stress was determined using oil-film interferometry. Streamwise friction coefficient is represented in fig. 3.13. Reattachment point was determined by interpolation (red square in fig. 3.13) and it is equal to $x/c = 1.11 \pm 0.003$.

3.5.5 Case setup

3.5.5.1 Finite volume mesh

Simulations have been performed on the simplified geometry of fig. 3.5. Channel dimension in spanwise direction is $0.2\,c$. Several mesh size were tested, with a total number of cells ranging from 2 million to over 11 million. Results presented here were obtained with $N \approx 7.6$ million cells ($N_x = 800$, $N_y = 150$ and $N_z = 64$). Example of mesh is shown in fig. 3.14 and detail of the last part of hump is in fig. 3.15.

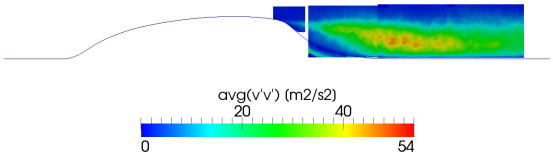

Figure 3.11: Contour plot of wall-normal Reynolds stresses $\langle v'v' \rangle$measured by PIV

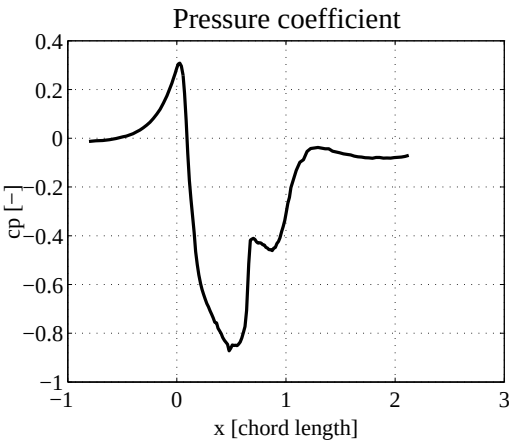

Figure 3.12: Experimental pressure coefficient C_p measured alung the hump profile

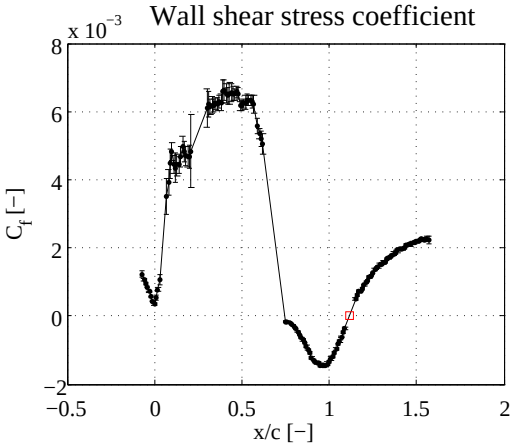

Figure 3.13: Experimental wall friction coefficient C_f along the hump profils

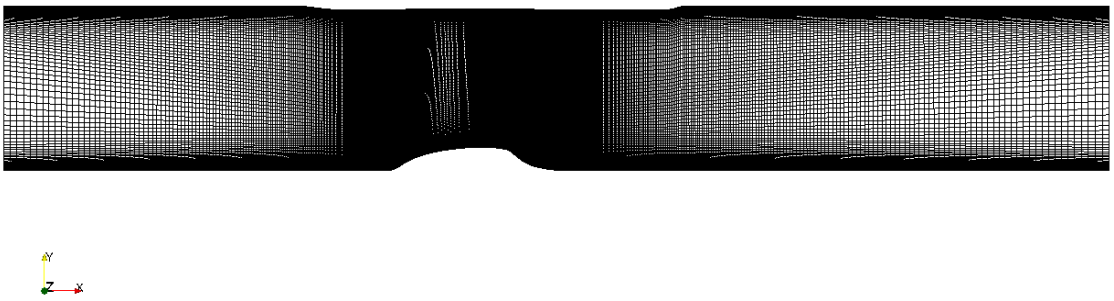

Figure 3.14: Global view of the mesh used for LES. Number of cells is $N_x = 800$, $N_y = 150$ and $N_z = 64$.

Mesh is refined in wall-normal direction to keep $y^+ < 1$ at least on the lower wall. On the other hand, it has been considered of minor importance to accurately solve the boundary layer on the ceiling wall. Mesh is axially refined in the hump region as well, whereas cell size near the inlet and outlet section is quite large. Number of cells is consistent to what other authors have used. For example, [89] used a structured mesh with $N_x = 426$, $N_y = 145$, $N_z = 64$ obtaining a good match between simulations and experiments.

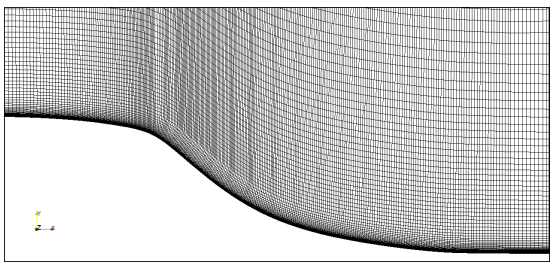

Figure 3.15: Closeup of the mesh near the separation region.

3.5.5.2 Filtering and subgrid scale modeling

In the context of the so-called double decomposition, Navier-Stokes equations undergo an implicit filtering by the finite volume mesh. So, no explicit filtering operation is applied when formulating the discrete form of conservation equations. However, if filter characteristic length is needed, it is calculated as the square root of cell volume:

$$\bar{\Delta}_i = V_i^{1/3} \quad i = 1 \ldots \text{n. cells} \tag{3.14}$$

The subgrid stress tensor appearing in the Navier-Stokes filtered equations (3.1) is modeled using the localized one-equation dynamic model (LDKM) by Kim and Menon [46]. Since all model's coefficients are computed using a dynamic procedure, the user has not to supply any value. Test filter needed to calculate intermediate-level quantities, that are required by the dynamic procedure, has a characteristic length $\tilde{\Delta} = 2\bar{\Delta}$.

3.5.5.3 Boundary conditions

Boundary conditions have been set up as follows. Walls are modeled as no-slip surfaces without any particular near-wall treatment. Outlet section has a convective condition on velocity ($\partial U/\partial n = 0$) and a Dirichlet condition on pressure. Front and back planes (at $z = 0$ and $z = 0.2$ x/c) are imposed a cyclic boundary condition for all variables. Inflow section is the subject of a parametric study to check whether it influences the results in any way, as it will be explained in the next section.

3.5.5.4 Inlet boundary conditions

Most commonly used inflow conditions for LES have been presented in section 3.4. In the present study, three of them will be applied to the test case, namely, fixed velocity profile (taken directly from experiments), mapped plane and synthetic turbulence.

Fixed profile The experimental mean velocity profile measured at $x/c = -2.14$ has been imposed on the inlet section of the domain. Since raw experimental data have a poor accuracy in the proximity of the wall, they have been spline-fitted to have a smoother profile, while retaining relevant quantities. Fig. 3.16 shows that near-wall velocity profile is consistent with the laminar law-of-the-wall. For points outside the measurement range ($y > 63$ mm) the constant freestream velocity has been imposed ($U_{\text{freestream}} = 34.6$ m/s).

As for velocity, subgrid-scale kinetic energy must be supplied as well if using SGS models based on it, such as dynamic model by Kim and Menon [46]. Since no fluctuations are imposed at inlet, we considered that all turbulent kinetic energy is unresolved: $k_{tot} = k_{sgs}$,

and $k_{tot} = 3/2\langle \overline{u}\,\overline{u}\rangle$, where the streamwise Reynolds stress $\langle \overline{u}\,\overline{u}\rangle$has been taken from experiments as well.

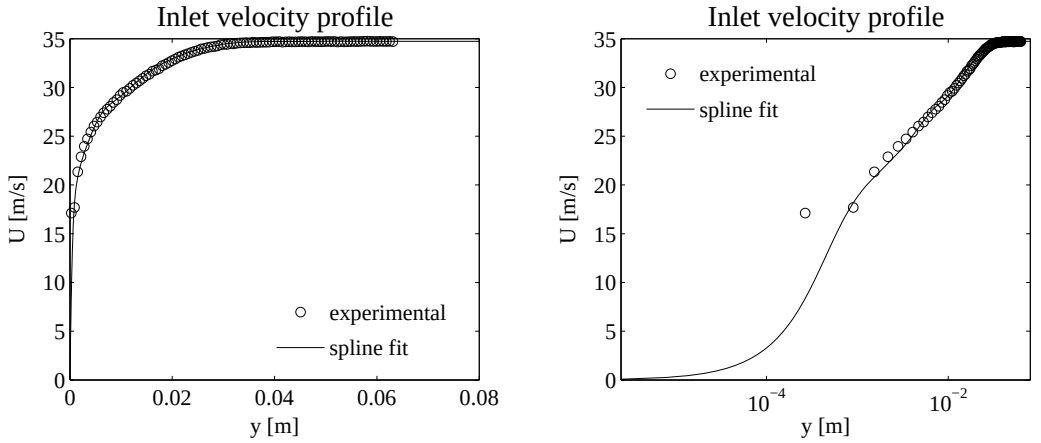

Figure 3.16: Mean velocity profile used for the constant inlet BC. Solid line is spline fit of experimental data (circles). Left: linear scale; right: logarithmic scale.

Mapped plane Mapped plane inlet condition require a minimum of setup. Sampling plane has been placed at one chord length downstream of the inlet ($x/c = -1.14$).

The following quantities have been imposed a mapped BC: velocity U, subgrid kinetic energy k_{sgs} and SGS viscosity ν_{sgs}. Also, velocity is rescaled at every timestep to ensure a constant flow rate.

Synthetic turbulence Synthetic turbulence generation procedure has many free parameters, in particular for what concerns global flow statistics. However, in most cases results are quite insensitive to many of them [18], so that some standard values can be adopted at least for time and length scaling factors, time filtering and wall blending function coefficients.

A precursor RANS simulation was run on a channel geometry with the same height as the hump case ($H = 0.909\,c$) and length equal to 20 chord units. Periodic boundary conditions are used for inlet and outlet to quickly obtain a fully developed boundary layer, at the same time ensuring a constant flow rate and a given bulk velocity. $k-\omega$ SST RANS model is employed and calculated dissipation rate is used to determine the turbulence integral length scale $\mathscr{L} = \sqrt{k}/\omega$. Maximum and minimum wavenumbers to generate the energy spectrum (according to (3.10)) are set as:

$$\kappa_{min} = 9\frac{\pi}{55}\frac{1.4526}{\mathscr{L}} \qquad \kappa_{\eta} = \varepsilon^{1/4}\nu^{-3/4} \tag{3.15}$$

Mean velocity profile on the inlet is the same as the previous case (fig. 3.16. Computed profiles of k and ω are shown in figs. 3.17 and 3.18 respectively.

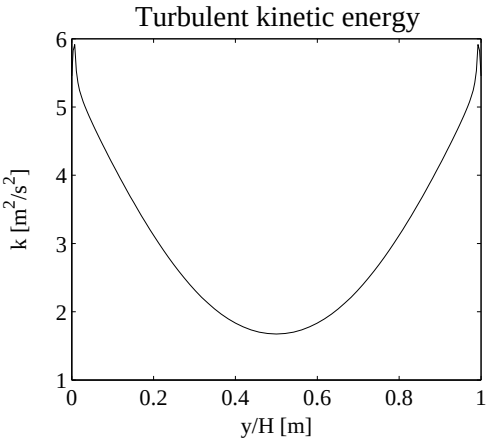

Figure 3.17: Profile of subgrid kinetic energy k used to initialize synthetic turbulence inlet BC

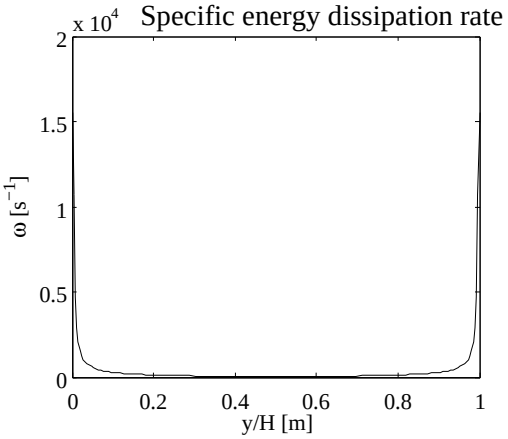

Figure 3.18: Profile of specific energy dissipation rate ω used to initialize synthetic turbulence inlet BC.

3.5.5.5 Numerical settings

Discretization schemes

- Discretization of temporal derivatives is done by the Crank-Nicholson differencing scheme [67]. In OpenFOAM there is the possiblity to blend classic Crank-Nicholson formulation with an Euler Implicit scheme to improve stability. This coefficient has been set to $\theta = 0.5$ due to the pure linear scheme used for convection terms.
- Pure linear interpolation has been used to discretize convection term in momentum equation $\nabla \cdot (UU)$, to avoid excess of numerical dissipation. Such a scheme is known to be unbounded and prone to cause instability; for that reason the maximum Courant number has been kept below to 0.6.
- Gradient and diffusion terms have been computed using centered differences.

Solver algorithm

- The numerical solver is based on the standard segregated PISO algorithm.
- Courant number has been limited to 0.6, that is quite a low value. The reason for that is the use of the centered difference scheme for convection terms.
- PISO is known to be accurate without additional momentum-corrector loops if the CFL criterion is fulfilled [26]. Moreover, the mesh is fully-structured and with good cell quality indicators. Therefore, only 2 pressure-correction steps are used in the solution algorithm.

Chapter 4

LES results and discussion

Validation of LES models can be performed according to two methods: *a priori* or *a posteriori* [72]. The former consists in validating the subgrid model alone, by comparing the computed subgrid stresses with those generated from an equivalent "exact solution" (like a DNS or a detailed experiment), which has been analytically filtered. On the other hand, *a posteriori* validation consists in comparing the exact LES solution with a reference one (experimental or DNS) in terms of some flow statistics.

It is generally acknowledged that *a posteriori* testing leads to better results, since it accounts for all simulation factors [88, 66, 14], even though it is difficult to discriminate between modeling and discretization errors.

Validation of OpenFOAM Large Eddy Simulations of the test-case described in the previous chapter will be carried out following the *a posteriori* procedure. In particular, the following quantities will be compared with experimental data: mean velocity streamlines and turbulent stresses in the separation region; pressure coefficient and wall friction coefficient along the hump profile.

All fluid-dynamic quantities have been averaged both in time and along the spanwise direction, to reduce the total number of flow-through-times needed to obtain flow convergence (flow-through times is defined as FTT = $(x_{out} - x_{in})/\overline{U}_0 = 0.073$ s).

Time averaging started after one FTT, and lasted for 5 FTT for the fixed inlet profile and for 2 FTT for the mapped plane and synthetic inlet. In figs. 4.1, 4.2 and 4.3, time history of mean velocity $\langle\overline{U}\rangle$ is shown. Velocity is sampled at three locations in the recirculation region at every timestep.

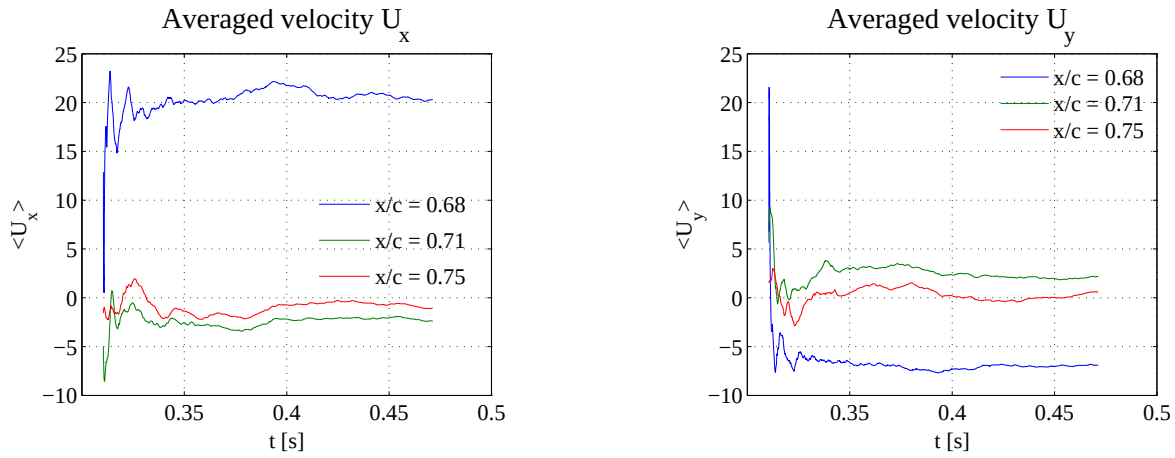

Figure 4.1: Sampled mean velocities U_x and U_y in three representative points for the fixed inlet case.

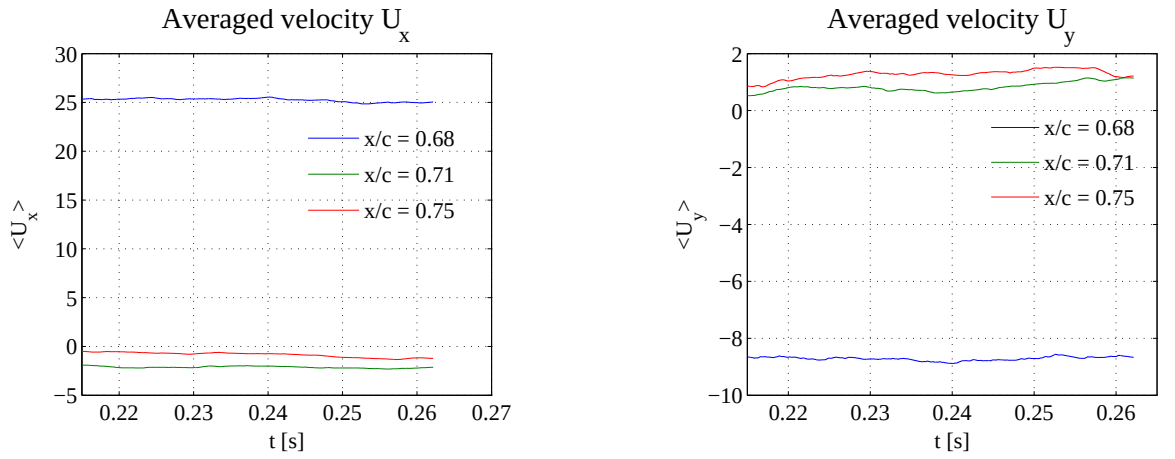

Figure 4.2: Sampled mean velocities in three representative points for the mapped inlet case.

4.1 Instantaneous velocity field

Operating principle of proposed boundary conditions can be seen in next figures (4.4 to 4.6) that show a snapshot of the instantaneous velocity field at $t = 5$ FTT.

When a fixed velocity profile is imposed on the inlet section (fig. 4.4), no turbulence is initially present in the flow. Only at some distance from the inflow, wall turbulence begins to develop and slowly produces fluctuations near the center of the channel.

Mapping the velocity field from an internal section back to the inflow allows for a quicker development of turbulence (fig. 4.5). Boundary layer appears to be better developed in near the entrance of the channel. As a consequence, global turbulence levels are higher.

Finally, generating synthetic fluctuations on the inlet (fig. 4.6) facilitates turbulence switching also near the center of the channel. Turbulent fluctuations are clearly visible in fig. 4.6,

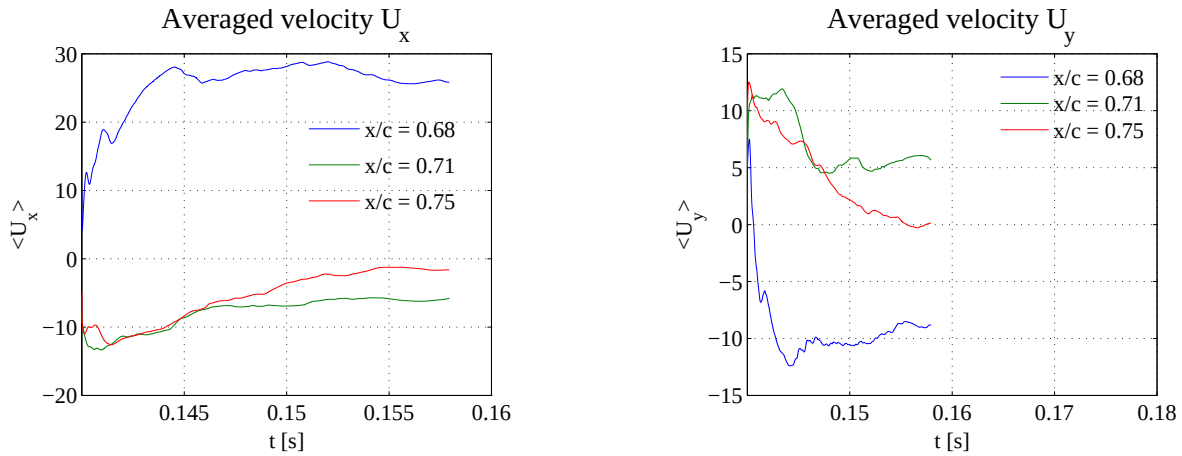

Figure 4.3: Sampled mean velocities U_x and U_y in three representative points for the synthetic turbulence case.

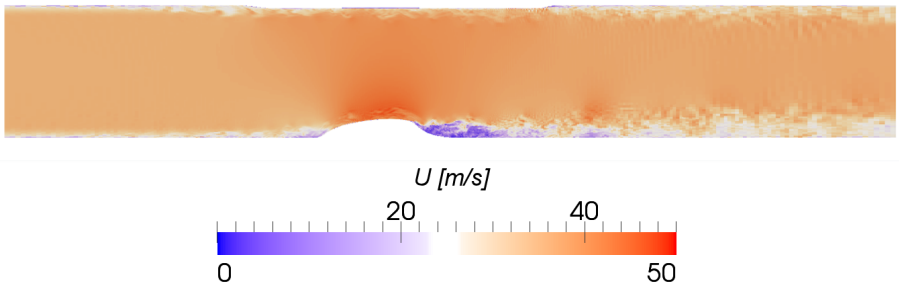

Figure 4.4: Snapshot of instantaneous velocity field at $t = 2FTT$ for the fixed inlet case.

even in the first zone of the channel where other boundary conditions does not seem to produce turbulence.

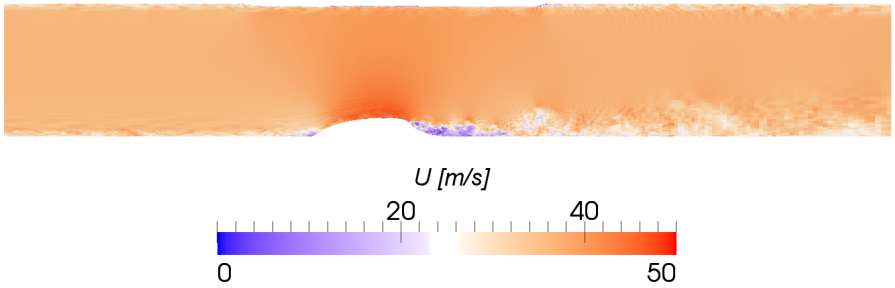

Figure 4.5: Snapshot of instantaneous velocity field at $t = 2FTT$ for the mapped inlet.

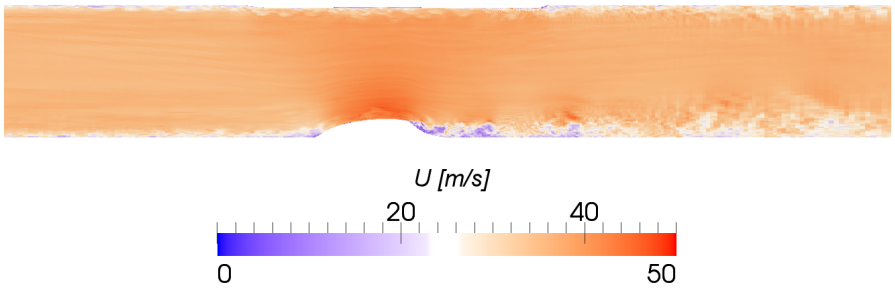

Figure 4.6: Snapshot of instantaneous velocity field at $t = 2FTT$ for the synthetic turbulence inlet case.

4.2 Mean velocity field

A comparison between computed and measured velocities can be seen by looking at mean streamlines in fig. 4.7 for fixed profile inlet; in fig. 4.8 for mapped plane inlet; and in fig. 4.9 for synthetic turbulence inlet.

Matching between simulations and experiments is quite poor. Although the vortex separation point seems to be captured quite well at a first sight, it is clearly visible that overall vortex size is half the size of the experimental one. This reflects also in the reattachment point, that is closer to the hump in the simulations with respect to the experiments. Inlet boundary condition seems to have scarce influence on the separated velocity field.

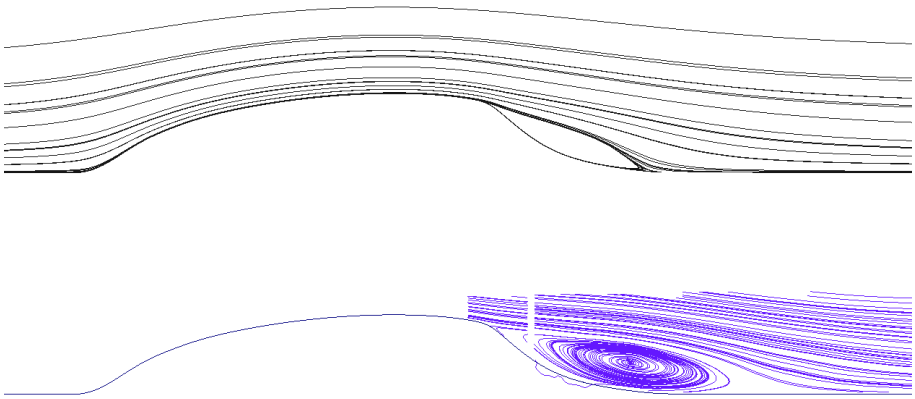

Figure 4.7: Comparison between computed (top) and experimental (bottom) mean flow streamlines for the fixed inlet case.

Mean velocity profiles in wall-normal direction are shown in fig. 4.10 for six stations along the hump after the separation point: $x/c = 0.65$ and $x/c = 0.66$, that bracket the experimental separation point); $x/c = 0.8, 0.9, 1.0$, that correspond to the bulk separation region; $x/c = 1.1$ to $x/c = 1.3$, that span the experimental and the computed reattachment point.

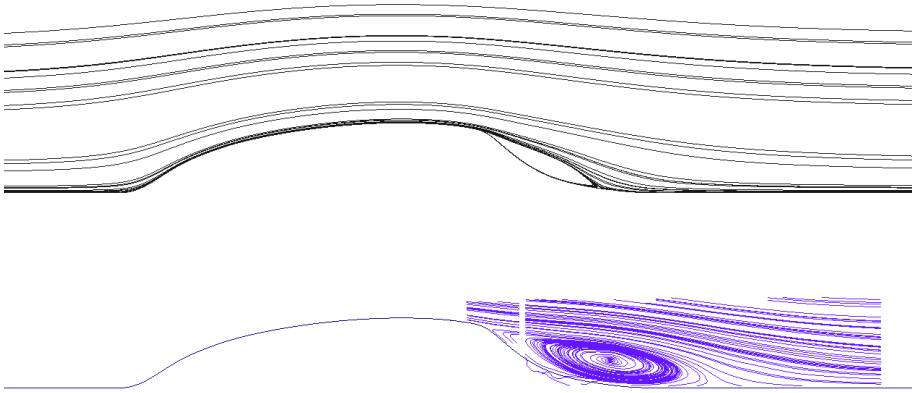

Figure 4.8: Comparison between computed (top) and experimental (bottom) mean flow streamlines for the mapped inlet case.

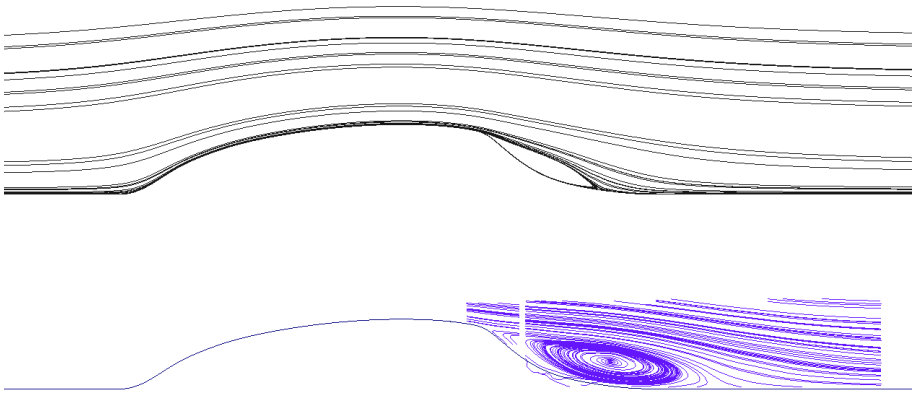

Figure 4.9: Comparison between computed (top) and experimental (bottom) mean flow streamlines for the synthetic turbulence inlet case.

Near-wall profiles are quite different between simulations and experiments, even for the first two locations ($x/c = 0.65-0.66$), where the boundary layer profile exhibits very strong differences. On the other hand, inlet boundary condition does not seem to be influential on that point.

Velocity profiles in other stations show even greater discrepancies in the bulk separation region, with a partial matching with experiments only in the outer region, with $y/c \gtrapprox 0.1$.

4.3 Wall shear stress

More details about near-wall velocity profiles can be found by examining the wall shear stress coefficient, fig. 4.11.

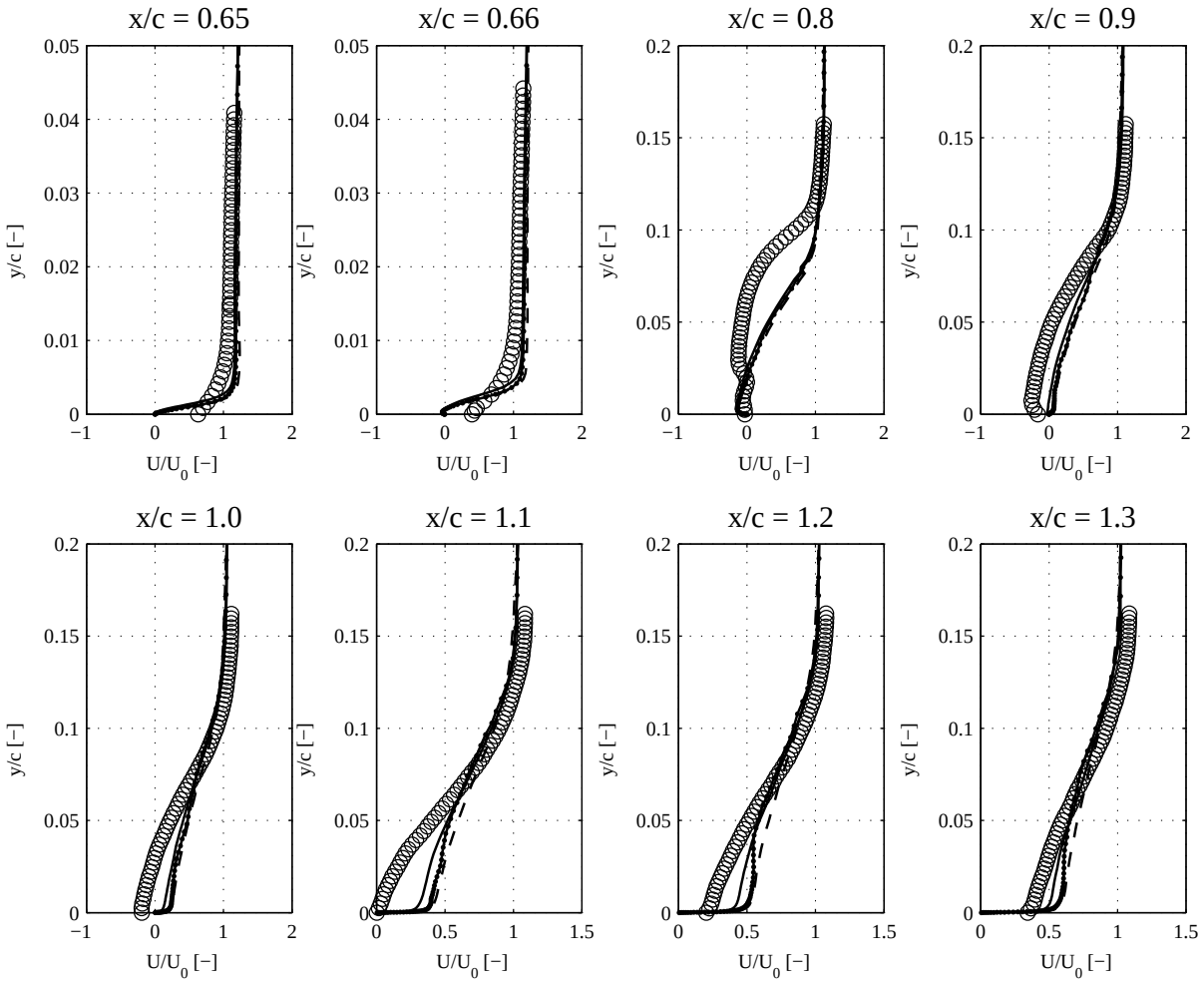

Figure 4.10: Mean velocity profiles in wall-normal direction for different inlet boundary condition: comparison against experiments.

Vortex separation and reattachment point can now be estimated with higher accuracy and they have been reported in tab. 4.1 for all cases. Despite streamlines indicated a quasi-perfect match in separation point, shear stress plot reveals that separation in experiments occurs slightly before than experiments. On the other hand, due to the strong underestimation of vortex size already pointed out, reattachment point is closer to hump trailing edge, with x_r/c ranging from 0.960 (fixed profile) to 0.915 (mapped plane).

Quite an underestimation of wall shear stress can be observed along the hump convex region as well ($x_c < 0.65$), where an adverse pressure gradient subsists (see also fig. 4.13). This fact suggests that near-wall velocities are probably solved with low accuracy and such errors affect the subsequent separation point and reattachment region.

Conversely, simulated C_f values are consistent with the experimental ones up to $x/c \approx 0.1$ and also the double peak between $x_c = 0.1$ and $x/c = 0.2$ is caught quite well (see fig.

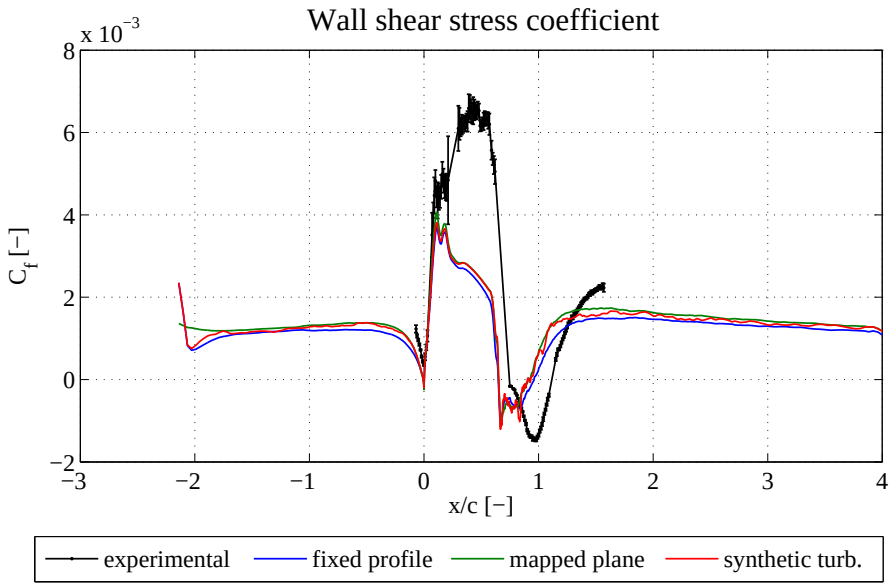

Figure 4.11: Wall friction coefficient for different inlet boundary condition: comparison against experiments.

Table 4.1: Computed separation and reattachment point for different inlet boundary condition: comparison against experiments.

inlet BC	x_s/c	x_r/c
experimental	0.75	1.11
fixed prof.	0.645	0.960
mapped plane	0.651	0.915
synth. turb.	0.652	0.931

4.12). Unfortunately, no data are available for $x/c < 0$ (channel upstream of the hump): such results could have helped in understanding if near-wall profiles are correctly solved in a plain channel-flow configuration.

4.4 Pressure coefficient

Pressure coefficient along the hump is represented in fig. 4.13 for both experimental measurements and simulations. Here the matching between computed solution and measured values is very good up to $x/c \approx 0.7$ where the separation occurs.

For $x/c > 0.7$ a local maximum exists in the measured data, that is absent in all the simu-

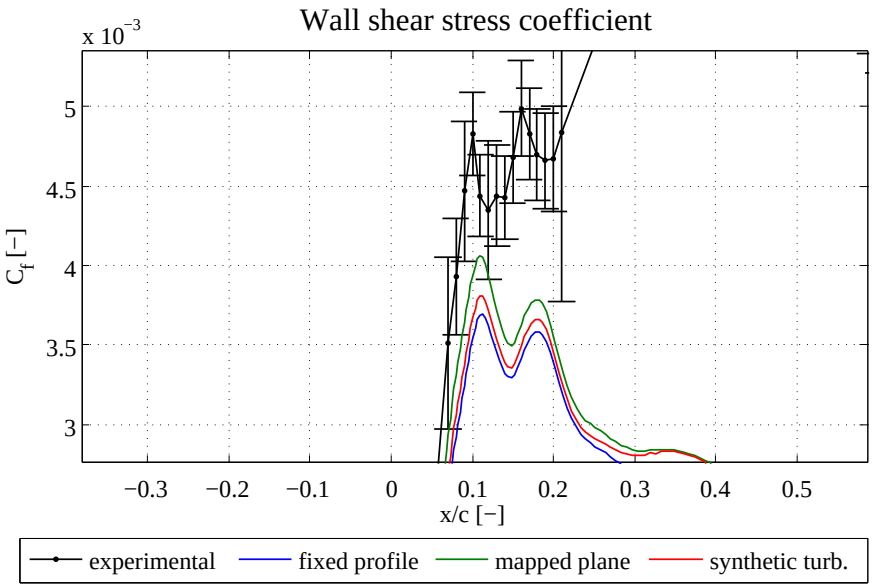

Figure 4.12: Detail of wall friction coefficient in the fore hump region. All inlet BC underestimates coefficient by a significant amount, though qualitative trends look similar.

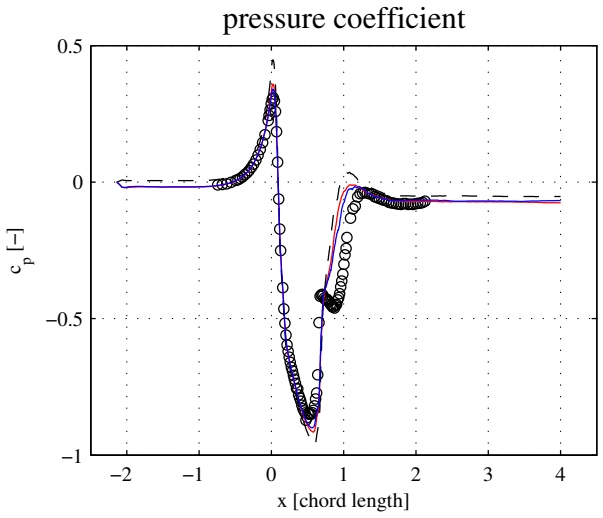

Figure 4.13: Pressure coefficient along the hump for different inlet boundary condition: comparison against experiments.

lations.

After reattachment ($x/c \approx 1.1$) pressure profiles tend to readjust to ambient values with quite a similar trend; however, the last maximum peak appears in different positions between simulations and experiments.

4.5 Resolved turbulence

In this section, resolved Reynolds stresses will be compared against measured ones. As pointed out in section 3.5.4, experimental turbulence levels presented here are valid only for qualitative comparisons.

A first comparison between simulated fields only (figs. 4.14 to 4.16, left column) does not reveal any significative difference between cases. Both qualitative contours and extreme values of Reynolds stresses $\langle \overline{u}\,\overline{u} \rangle$, $\langle \overline{v}\,\overline{v} \rangle$and $\langle \overline{u}\,\overline{v} \rangle$are similar. In particular, fixed profile (fig. 4.14) and synthetic turbulence (fig. 4.16 exhibits almost equal maximum values, whereas mapped plane case has locally higher levels of turbulence (fig. 4.15).

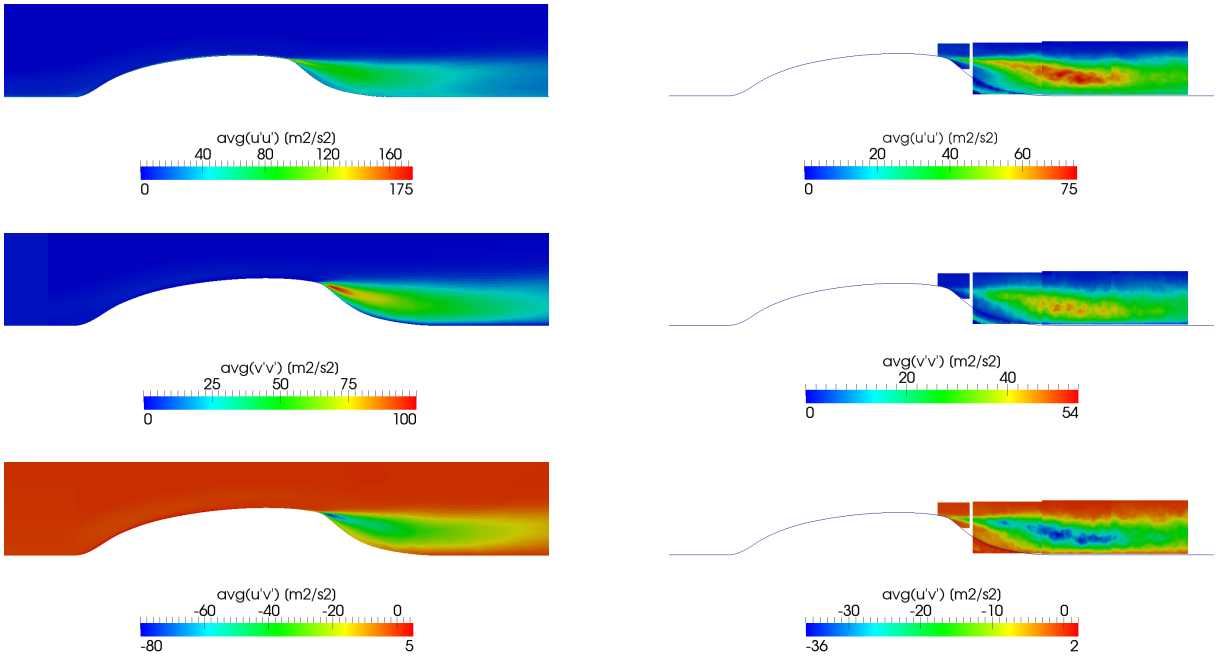

Figure 4.14: Comparison between measured and computed resolved Reynolds stresses for fixed inlet case. Due to high uncertainty in experiments, values can be used only for qualitative reasoning. Left: simulations; right: experiments

When comparing simulations and experiments, larger differences appear. In correspondence of the hump concave zone, where recirculation occurs, mean experimental turbulence levels are quite lower; order of magnitude is comparable to freestream flow.

On the other hand, simulations does not show such low turbulence zone near the hump. A turbulent plume that originates at separation point extends downstream filling all the space down to the lower wall. Such a behaviour can be observed with almost equal characteristics for fixed profile inlet (fig. 4.14) and mapped plane (fig. 4.15), whereas synthetic inlet case (fig. 4.16) looks more similar to experiments.

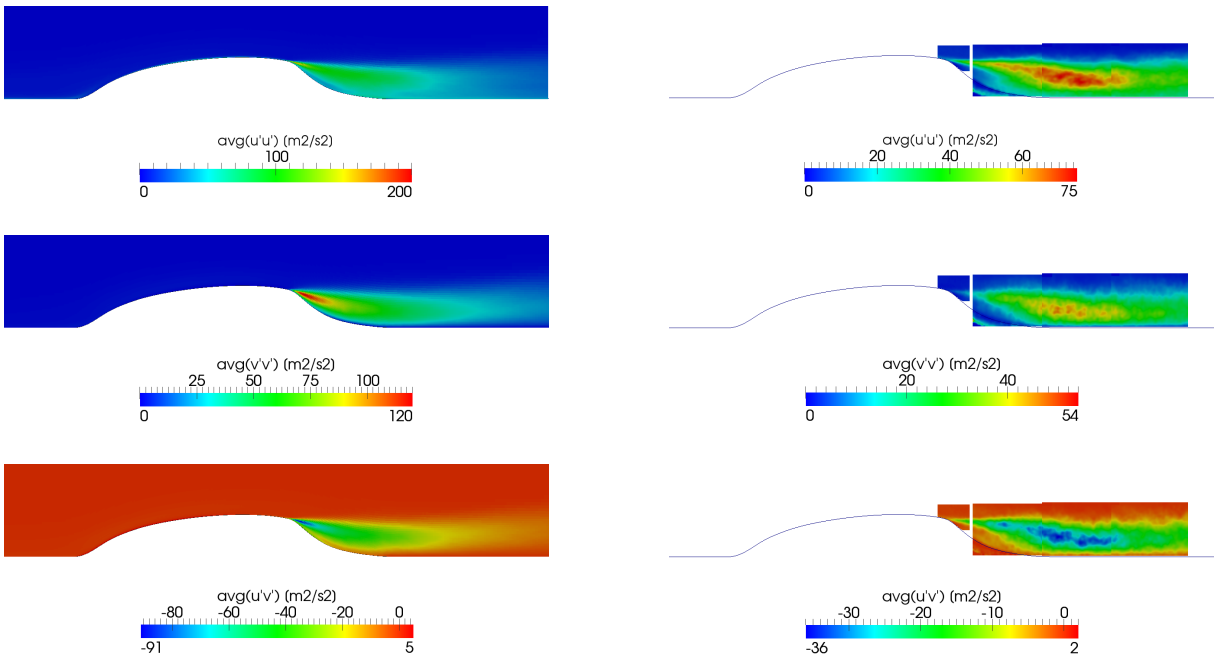

Figure 4.15: Comparison between measured and computed resolved Reynolds stresses for mapped inlet case. Due to high uncertainty in experiments, values can be used only for qualitative reasoning. Left: simulations; right: experiments

Moreover, experimental data show a narrow inner plume that lies approximately on the outer vortex boundary. Values of Reynolds stresses here are quite larger with respect to surrounding flow, due to strong velocity gradients. Such an inner structure is either not visible or it is strongly reduced in simulations.

In conclusion, resolved turbulence show some similarities with measured one, but, like other flow statistics, it has strong discrepancies as well. This indicates that probably some undetected source of error has been introduced in the simulations. In the next section we will give some hypotheses about it and a possible solution will be proposed.

4.6 Discussion

Results obtained via LES on the geometry and case setup under study could not been validated. Comparison of flow statistical moments (either mean velocity or resolved turbulence) showed deep discrepancies between simulations and experiments. In this section, possible causes of errors will be discussed. In particular, the influence of subgrid model and mesh will be analyzed.

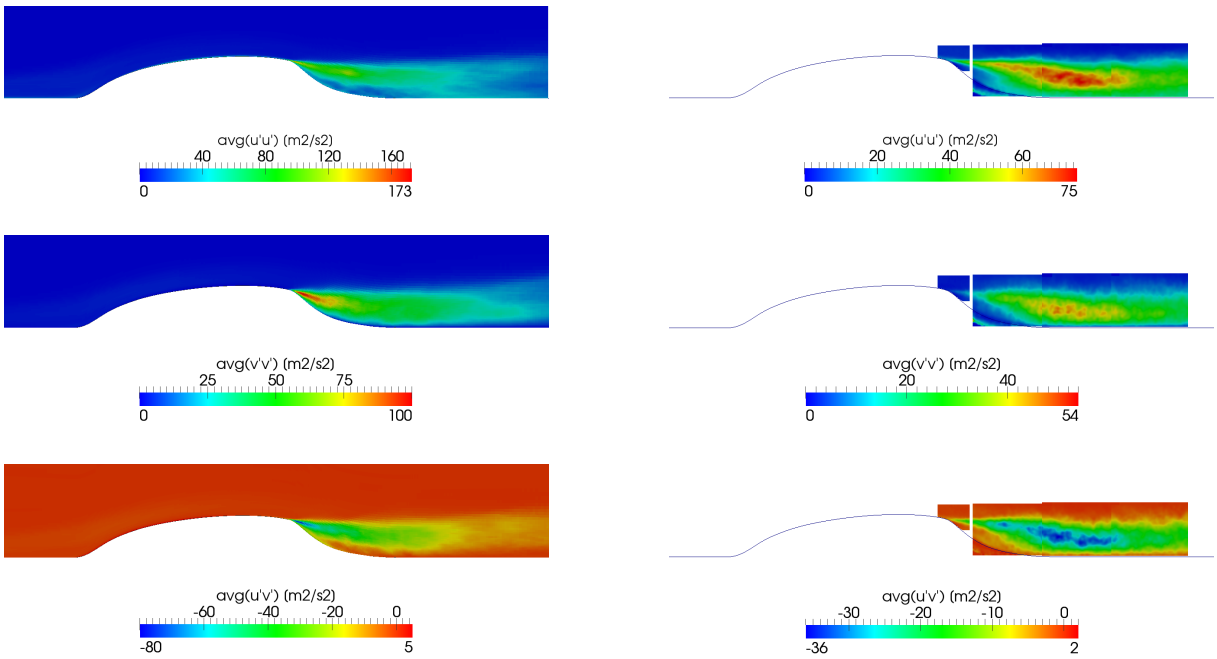

Figure 4.16: Comparison between measured and computed resolved Reynolds stresses for synthetic turbulence inlet case. Due to high uncertainty in experiments, values can be used only for qualitative reasoning. Left: simulations; right: experiments

4.6.1 Influence of the subgrid model

In order to understand the influence of subgrid model on the results, simulations have been carried out using different subgrid models. Among all possible choices, the following models have been tested and compared with results of previous section: classic (constant coefficient) Smagorinsky [77], dynamic homogeneous Smagorinsky, original subgrid-energy model by Kim and Menon [45].

4.6.1.1 Smagorinsky model setup

In OpenFOAM, the classic extension of Smagorinsky model based on the dynamic procedure by Germano [29] is implemented in a homogeneous fashion. The subgrid model coefficient C_d, that enters the closure relation as: $\langle \nu_{sgs} \rangle = (C_d \bar{\Delta})^2 \langle 2|\overline{S}|^2 \rangle^{1/2}$, is space-averaged over the domain. Such a model did not provide usable results for the case under study, since the predicted flow field showed no separation at all. However, this fact gave us the first evidence that subgrid model is possibly a critical parameter for this type of cases.

Classic Smagorinsky model employs a constant value of the subgrid-stress coefficient. In

the original formulation, subgrid viscosity is computed as:

$$\langle \nu_{sgs} \rangle = (C\bar{\Delta}) \left\langle 2|\bar{S}^2| \right\rangle^{1/2} \tag{4.1}$$

with the C coefficient that can vary from 0.148 to 0.18, depending on the method used to compute it [72]. In OpenFOAM, a similar relation is used, and subgrid viscosity is obtained as:

$$\langle \nu_{sgs} \rangle = C_k \bar{\Delta} \left\langle \frac{2C_k}{C_\varepsilon} \bar{\Delta}^2 |\bar{S}^2| \right\rangle^{1/2} \tag{4.2}$$

With the default values of $C_k = 0.094$ and $C_\varepsilon = 1.05$, one obtains $C = 0.168$, that lies within the admissible range. However, the value of C_s is flow-dependent, so it has often to be tuned to obtain correct results. For the present test, C_s has been set to 0.1, the same value used by Šaric et al. [89] for their work. Near-wall laminar sublayer is taken into account by multipliyng the filter characteristic width by the Van-Driest damping function [86]. Inlet BC is of the first kind (fixed profile) and all remaining setup parameters are the same used in the previous cases.

4.6.1.2 Mean velocity

The instantaneous and mean velocity field are represented in figures 4.17 and 4.18 respectively. Looking at the instantaneous velocity, wall structures appear to be less resolved, especially in the first part of the hump. At a first sight, flow separation occurs at the same point as before, while the reattachment is located farther from the hump. This trend is confirmed by the mean-flow streamlines (fig. 4.18), that show a recirculation bubble larger than the experimental one.

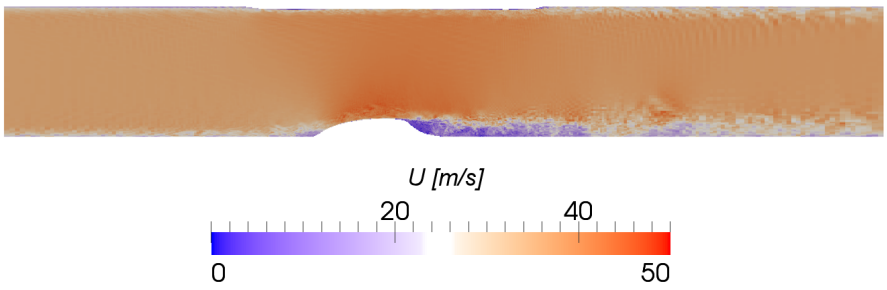

Figure 4.17: Snapshot of instantaneous velocity field at $t = 5FTT$ computed using fixed inlet and classic Smagorinky model with $C_s = 0.1$.

4.6.1.3 Resolved turbulence

Resolved Reynolds stresses (fig. 4.19) are closer to experiments with respect to other cases. Both the order of magnitude and the qualitative contours look very similar to experiments

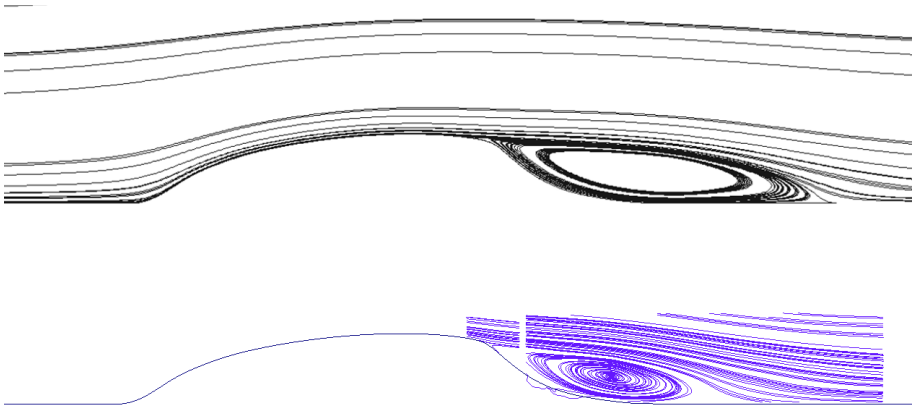

Figure 4.18: Streamlines of mean velocity field at $t = 5FTT$ computed using fixed inlet and classic Smagorinky model with $C_s = 0.1$.

and the correct shape of the turbulent 'plume' is reproduced quite well, with a low-turbulence zone in the concave region of the hump. Such a feature was not visible in simulations performed using the LDKM subgrid model, that showed poor agreement even in a qualitative sense.

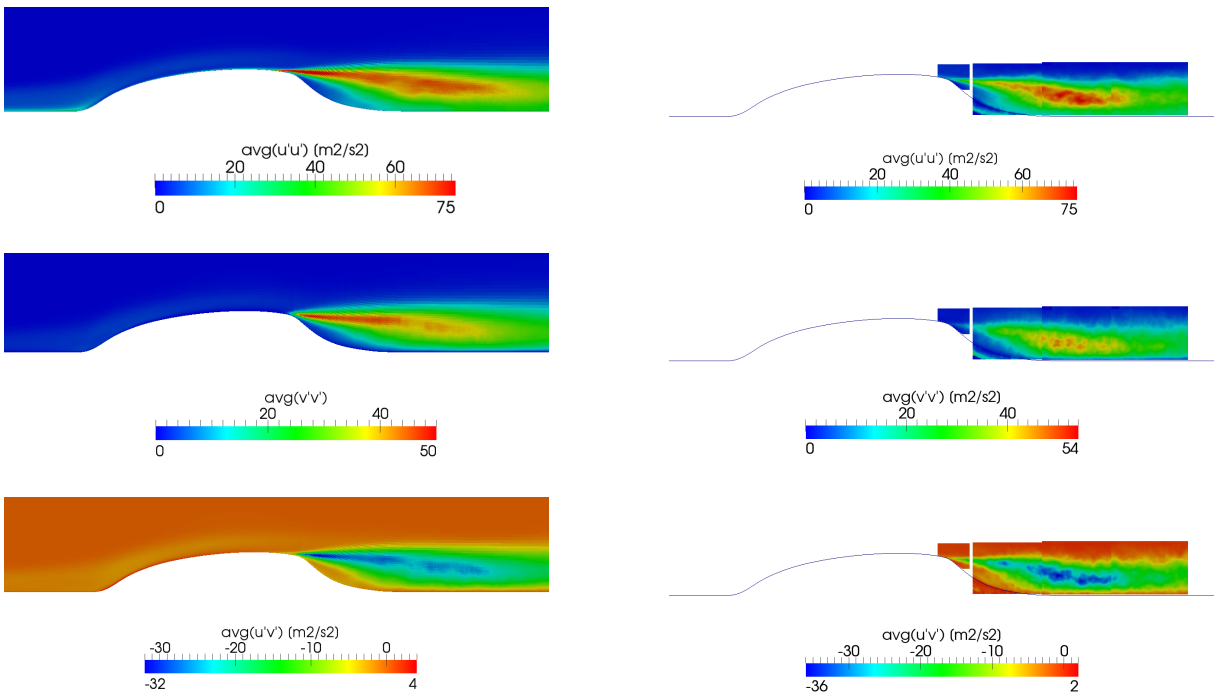

Figure 4.19: Comparison between measured and computed resolved Reynolds stresses for Smagorinsky subgrid model and fixed inlet BC. Left: simulations; right: experiments

4.6.1.4 Separation and reattachment point

Separation and reattachment points can be precisely computed by plotting the wall friction coefficient along the hump coordinate. From fig. 4.20 it can be easily seen that reattachment point is at $x/c \approx 1.33$, quite downstream with respect to the experiments ($x/c \approx 1.11$), whereas separation point is at $x/c \approx 0.64$, a value that is similar to what has been obtained before.

Also, like previous simulations, computed C_f underestimates real values, especially in the second part of the hump. However, overall accuracy is better, for the "double peak" of fig. 4.21 is caught with very good approximation.

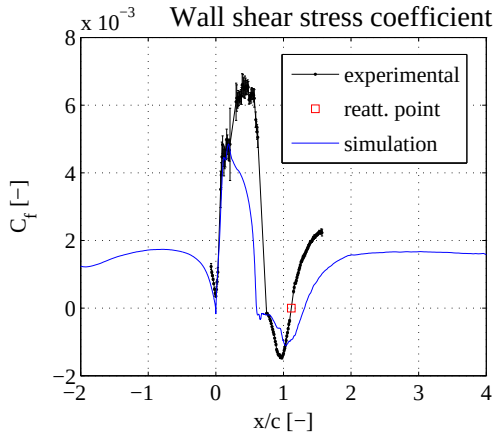

Figure 4.20

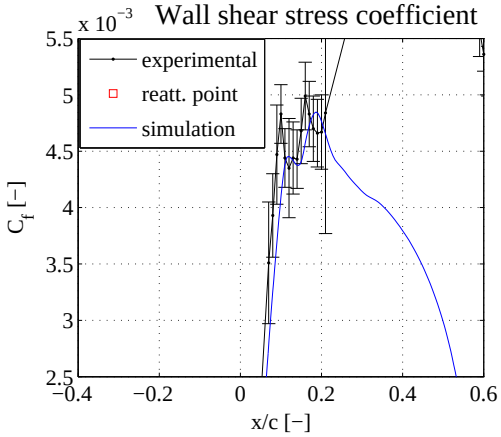

Figure 4.21

4.6.1.5 Pressure coefficient

Finally, the pressure coefficient C_p is compared in fig. 4.22. Again, the experimental profile is not caught well, especially after the local minimum at $x/c \approx 0.5$. Nonetheless, the global trend appears much better. The small negative pressure gradient zone, that lie just in correspondence of negative mean flow, is now clearly visible despite its absolute value is not correct. Such a feature was absent from LDKM simulations.

4.6.1.6 Final remarks

The evidence presented so far suggests that subgrid models plays a predominant role in the solution of this type of flow. In particular, a kinetic-energy based model seems to behave worse than the simpler fixed-coefficient Smagorinsky. Some hints that could serve to explain the reason for such a paradox can be inferred by looking at the boundary layer properties just before the adverse pressure gradient part of the profile ($x/c = 0.5$).

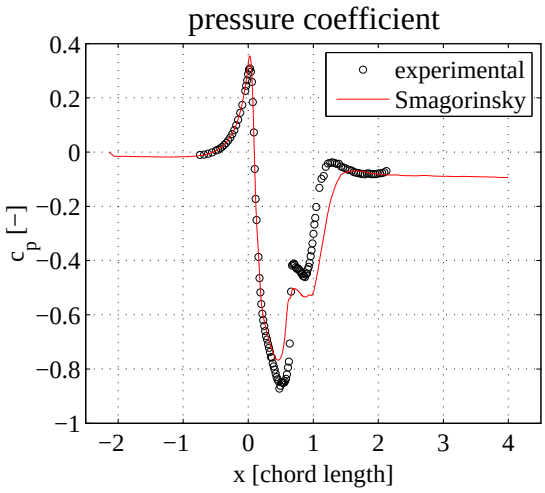

Figure 4.22: Pressure coefficient C_p for Smagorinsky case: comparison with experiments

The plot of subgrid viscosity versus wall distance, fig. 4.23, shows that in the former simulation (LDKM), viscosity goes smoothly to zero in some wall length scales. At $y^+ \lessapprox 30$, that corresponds to the outer buffer layer, $\nu_{sgs}/\nu \approx 0.01$, whereas with the Smagorinsky model $\nu_{sgs}/\nu \approx 4$. For Smagorinsky model, the same ν_{sgs}/ν ratio is obtained at $y^+ \lessapprox 3$, that is close to the viscous sublayer.

As a consequence of the lower subgrid dissipation, in the LDKM case the inner layer is expected to have higher energy levels. This is confirmed by the graph of the normal stresses $\langle \overline{u}\,\overline{u} \rangle$ versus wall-normal scaled distance, fig. 4.24. With the LDKM model, maximum value is more than double with respect to the Smagorinsky model, even though both peaks fall into the buffer layer region, as predicted by the theory.

Last thing to be discussed is whether such properties (subgrid viscosity, normal stresses) can have such a big influence on separated flow. Separation usually occurs for either adverse pressure gradient or flow curvature. In the present case, both of the mechanisms are present. Studies on boundary layer separation under adverse pressure gradient showed that there is a weak dependence on Reynolds number of the separation point, even though turbulent quantities scale with Reynolds [79]. Therefore, even if there are differences in turbulence profiles (as observed in fig. 4.24), the separation point indeed does not change.

On the other hand, reattachment point is seen to be strongly dependent on upstream Reynolds number, and thus on near-wall turbulence, for flows with bulk separation like the backward-facing step. In particular, reattachment length is observed to be shorter as freestream Reynolds number increases [78, 42], cited by [76].

Finally, the standard (homogeneous coefficient) Kim and Menon model [45] has been applied to the same test-case. No significant differences have been highlighted with respect

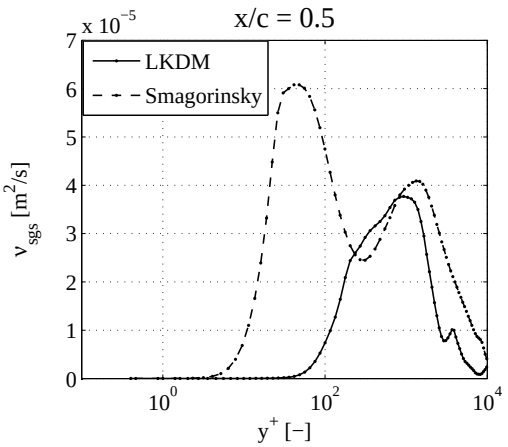

Figure 4.23

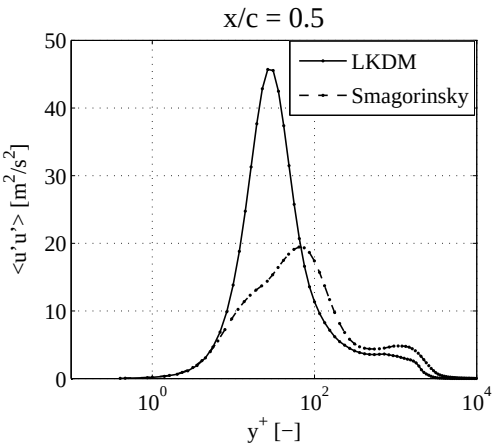

Figure 4.24

to the non-homogeneous model (LDKM), and thus no results are reported here.

4.6.2 Influence of the mesh

4.6.2.1 Coarse mesh characteristics

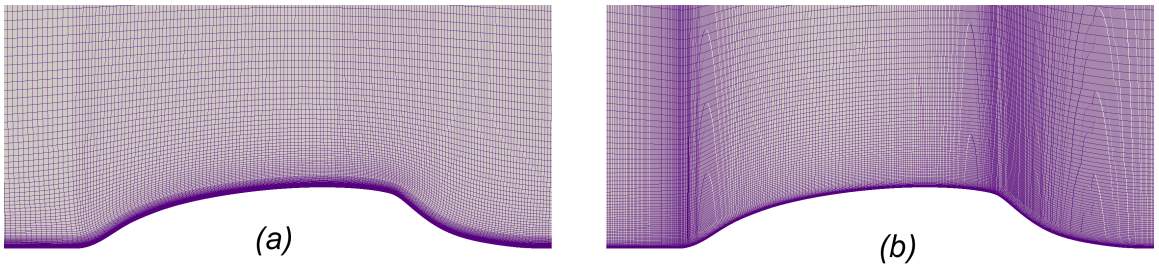

Figure 4.25: Close-up view of the mesh in the vicinity of the hump. (a) coarsened mesh, (b) original mesh

Space discretization in LES plays a major role on the accuracy of the solution, as it has been pointed out in section 3.3.2. However, a complete survey of mesh sensitivity on the proposed test case is out the scope of this work and it has not been carried out. Nonetheless, some useful information about mesh-related sources of error can be sought by comparing results obtained on two different meshes. The same case setup used in the previous cases has been applied on a coarsened mesh (fig. 4.25). The coarser mesh has larger cells both in streamwise and wall-normal directions, whereas spanwise cell number was left unchanged. Cell size distribution are represented in fig. 4.26 (streamwise) and 4.27 (wallnormal at $x/c = 0.5$).

Apart of being coarsened, the second mesh came along with different quality parame-

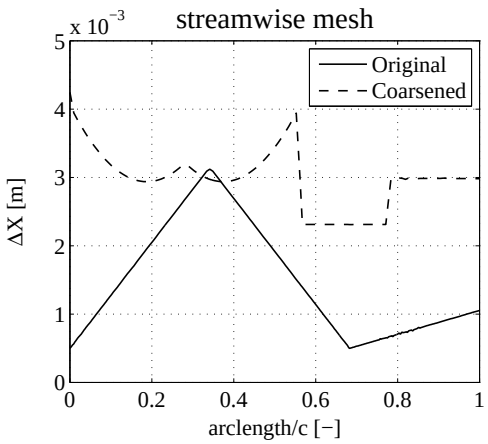

Figure 4.26: Comparison of axial cell size versus arc length along the hump. $x/c = 0$ is leading edge, $x/c = 1$ is trailing edge

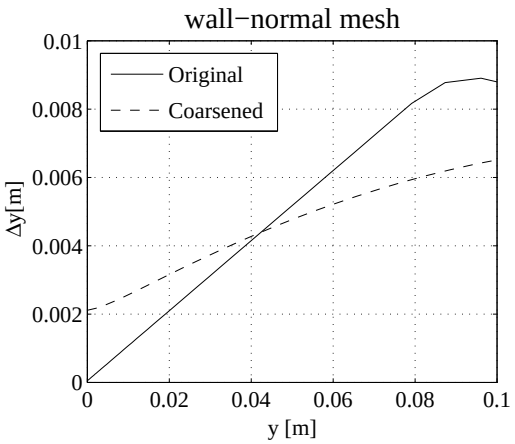

Figure 4.27: Comparison of wall-normal cell size at $x/c = 0.5$, just before the expected separation point

ters. Coarser mesh has maximum non-orthogonality of 68.15 (on average 3.98), maximum skewness 0.156, maximum cell aspect ratio 587.68. Finer mesh has a lower maximum non-orthogonality (43.32) while the average value is higher (7.39), as well as skewness (0.503) (3322.75); the latter, moreover, exceeds the maximum value tolerated by the code, i.e. 1000.

Local comparisons of mesh quality parameters can be seen in the following images. In the proximity of the hump, either skewness (fig. 4.28), shear factor (fig. 4.29 and stretching (fig. 4.30) are lower (better quality) in the coarser mesh.

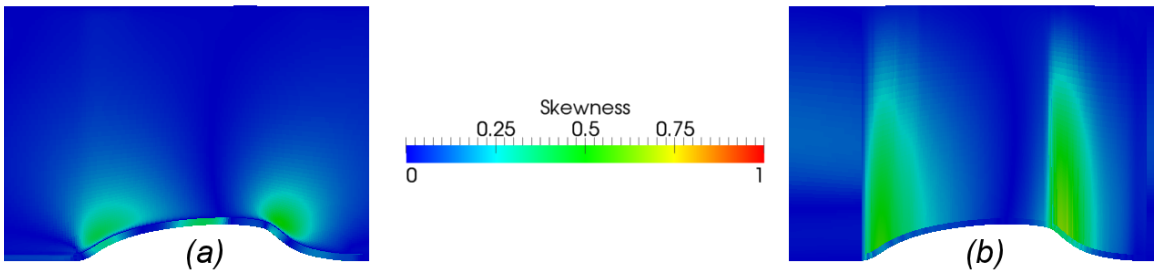

Figure 4.28: Contour plot of cell skewness. (a) coarsened mesh, (b) original mesh

4.6.2.2 Results

Streamlines of mean velocity and snapshot of instantaneous flow field at $t = 5FTT$ are represented in fig. 4.31 and 4.32, respectively. Quite surprisingly, no separation is visible at all. Reason for such a bad accordance is not easy to investigate, but most probably is related to mesh size in the boundary layer.

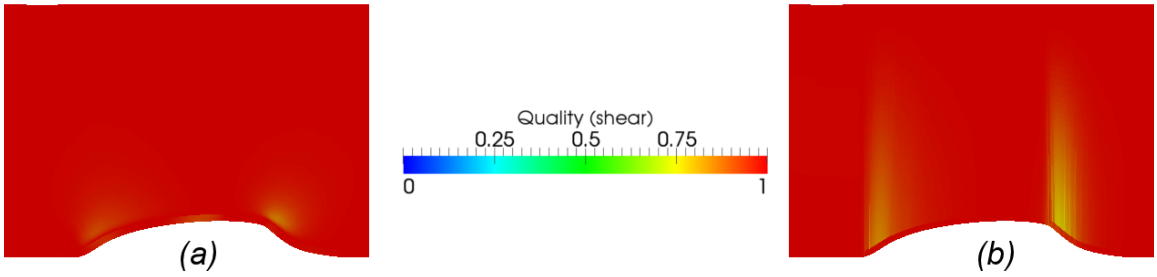

Figure 4.29: Contour plot of mesh shear factor. (a) coarsened mesh, (b) original mesh

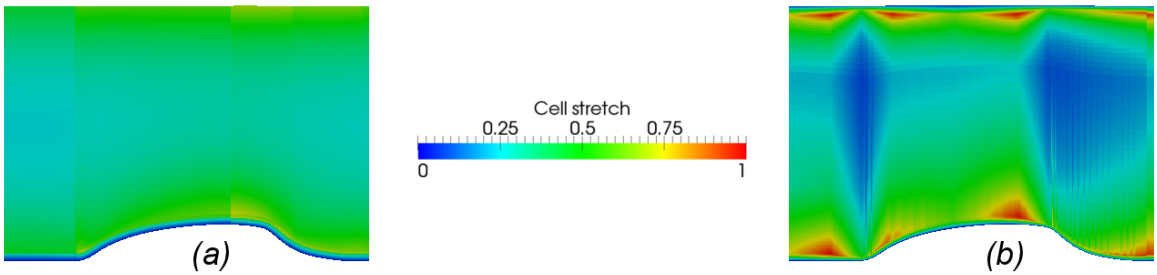

Figure 4.30: Contour plot of cell stretching factor. (a) coarsened mesh, (b) original mesh

In the following graphs, the scaled velocity profile $U^+(y^+)$ and streamwise stresses are reproduced. First difference between original and coarsened mesh lies in the size of the first wall cell. While in fine mesh $y_0^+ \approx 0.1$, that is well into the laminar sublayer, for the coarsened case we have $y_0^+ \approx 2$, that lies in the buffer zone. As a consequence, boundary layer is not correctly resolved, as one can see from fig. 4.33, where velocity profile for the coarser case does not resemble at all the expected trend.

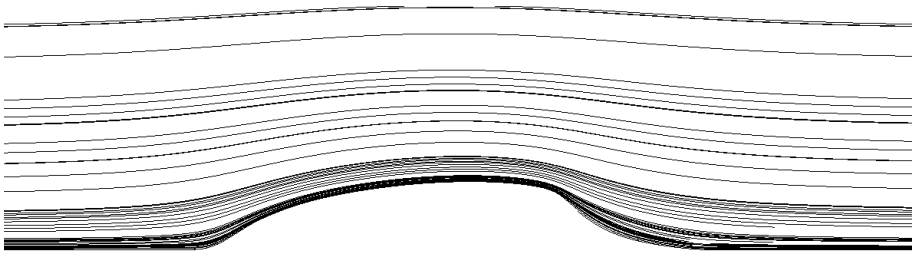

Figure 4.31: Streamlines of mean velocity for the coarsened case: the flow exhibits no separation

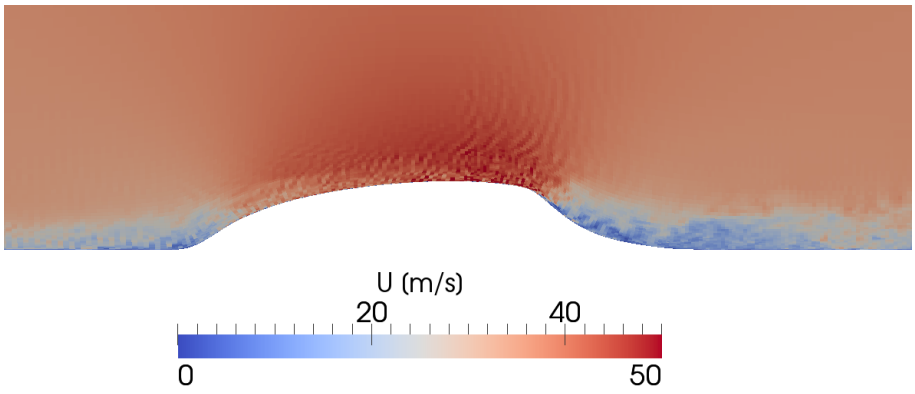

Figure 4.32: Snapshot of instantaneous flow field for the coarsened case for $t = 5\ FTT$

Moreover, turbulence remains underresolved and resolved Reynolds stresses are quite underpredicted, as might be seen from fig. 4.34. This could be inferred also by the subgrid viscosity plot (fig. 4.35), where ν_{sgs} values for $y^+ < 100$ for the coarser case are quite larger than the original ones.

Obviously, so large being the discrepancies between computed and reference data, no further quantitative analysis would be of any use.

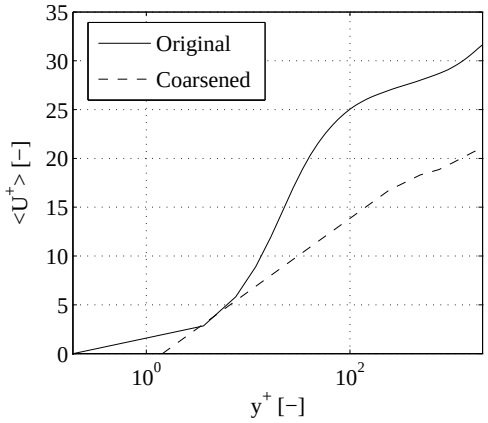

Figure 4.33: Comparison of near-wall scaled velocity profiles at $x/c = 0.5$, just before the expected separation point

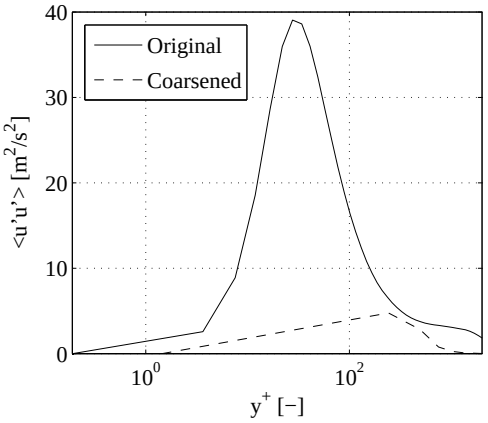

Figure 4.34: Comparison of near-wall streamwise resolved fluctuations at $x/c = 0.5$, just before the expected separation point

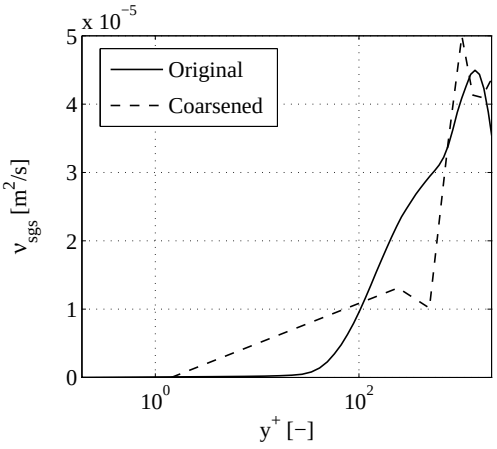

Figure 4.35: Comparison of near-wall subgrid viscosity at $x/c = 0.5$, just before the expected separation point

4.7 Closure

In front of a far-from-perfect match between simulation results and reference data, a short analysis allowed for highlighting some criticities and strengths of LES simulations for this type of flow. Main flow feature is the size and shape of the recirculation bubble, so this is the parameter that has been observed when studying the influence of case setup parameters.

Inflow boundary condition is scarcely influential on the separation region: all of the three method under examination (fixed velocity profile, mapped plane, synthetic turbulence) showed similar results, both in terms of qualitative trends and quantitative parameters.

Subgrid model is a critical aspect of simulations: switching from the sophisticated LDKM model to the simple fixed-coefficient Smagorinsky model caused the separation region to change by a significan amount. In particular, while separation point remained about the same, reattachment point moved downstream by 44%. A closer look at near-wall turbulence showed great differences in subgrid viscosity and wall-normal resolved fluctuations. LDKM model produced higher values of streamwise Reynolds stresses as a consequence of lower subgrid dissipation. By analogy with the backward-facing step case, this might have moved the reattachment point upstream.

Near-wall mesh is another critical point that showed up during the present analysis. The same setup of the baseline case has been run on a coarser mesh. Cell size was strongly enlarged both in wall-normal direction, and streamwise. As a consequence, first wall mesh point ended up to be at $y_0^+ \approx 2$ instead of $y_0^+ \approx 0.1$ (baseline). If near-wall flow remains

strongly under-resolved, separated flow characteristics would be affected, up to the point to show no separation at all. Such a behaviour can not be ascribed to quality parameters other than cell size, since coarser mesh came along with generally better quality parameters.

Conclusions

In this thesis work, application of CFD to ICE problems has been studied. As available computing power increases, CFD importance in the early design stage has shown a sensible growth as well.

In the first part of the present work, an original model to simulate clean flow and loading of DPF has been presented. Such a novel approach is able to solve, within one domain, both the filter region and the inlet/outlet cones, with clear advantages in terms of simulation efficiency. Moreover, it is possible to carry out a detailed study of flow pattern inside the DPF honeycomb matrix. Flow non-uniformities, as well as collected soot distribution, can be obtained with great detail (up to single-channel scale).

DPF modeling with this approach proved to be accurate and reliable. Substrate permeability is the only parameter to be tuned, but it does not change as long as the porous wall characteristics remain the same. Prediction of pressure drop and flow field is done with very good accuracy.

The model has been extended with the inclusion of a soot transport and deposition model. Pressure drop curve due to filter loading is predicted with very good accuracy, as well as changes in channel-scale velocities.

On the other hand, the explicit formulation of the solver poses some limits on the time integration step, thus a complete loading cycle of a full-scale filter is unfeasible for the moment. However, there are some evidence that an implicit reformulation of the source terms would bring important benefits by this point of view. Extending the model to include filter regeneration and heat transfer would be possible at that point.

Second part of this thesis considered evaluation of LES for ICE simulation. Purpose of this work was to draw some general conclusions about the correct case setup for LES, for types of flow similar to those encountered in ICE, in particular the influence of the inlet boundary condition. Test case used for validation has been the number 83 of ERCOFTAC database “wall-mounted hump”, for which a wide set of experimental data exists.

Three inlet boundary conditions have been tested: fixed velocity profile, mapped plane, synthetic turbulence. They differs in the level of detail of the generated field and, as a conse-

quence, in the additional computation cost.

For the proposed test-case, inlet boundary conditions has shown little influence on the final result. On the other hand, simulations proved to be very sensitive to FV mesh and subgrid model. Hence, any influence of the inlet condition is probably of lesser importance in this types of flow, whereas correctly solving near-wall turbulence (either by choosing an appropriate SGS model and with a sufficiently fine cell size) is mandatory for wall-bounded flows with separation. Unfortunately, no conclusive criteria can be stated at this point.

In the end, application of LES techniques to an ICE simulation remains a delicate problem. A robust procedure needs to be implemented before any attempt to apply LES to a real-world problem, for other factors enters the game (among others: compressible flow, complex geometry, moving mesh, etc.). Their influence might interact with other critical setup parameters, leading to little significance of the results.

Bibliography

[1] ACEA. European automobile industry report. European Automobile Manufacturers Association, 2009.

[2] ACEA. 2011 automobile industry pocket guide. European Automobile Manufacturers Association, September 2011.

[3] G. Ahmadi and Q. Chen. Dispersion and deposition of particles in a turbulent pipe flow with sudden expansion. *Journal of Aerosol Science Technology*, 29:1097–1116, 1998.

[4] R. Albanese, F. Grasso, and C. Meola. On the critical problem of F.D. pressure treatment for laminar flows confined by permeable walls. *Int. J. for Numerical Methods in Fluids*, 4(11):1027–1041, 1984.

[5] A.A. Amsden, P.J. O'Rourke, and T.D. Butler. *KIVA-II: A Computer Program for Chemically Reactive Flows with Sprays*. LA 11560-MS, Los Alamos National Laboratory, 1989.

[6] M. H. Baba-Ahmadi and G. Tabor. Inlet conditions for LES using mapping and feedback control. *Computers & Fluids*, 38(6):1299–1311, June 2009.

[7] J. Bardina, J. H. Ferziger, and W. C. Reynolds. Improved subgrid-scale models for large eddy simulation. AIAA paper 80-1357, 1980.

[8] J. Bardina, J. H. Ferziger, and W. C. Reynolds. Improved turbulence models based on large eddy simulation of homogeneous, incompressible, turbulent flows. Report TF-19, Thermosciences Division, Dept. Mechanical Engineering, Stanford University, 1983.

[9] A. Bejan. *Convection Heat Transfer*. John Wiley and Sons, New York, NY, 1985.

[10] Mattias Billson. *Computational Techniques for Turbulence Generated Noise*. PhD thesis, Chalmers University of Technology, Göteborg, Sweden, 2004.

[11] F. Brusiani and G. M. Bianchi. Basic numerical assessments to perform a quasi-complete les toward ic-engine applications. In *Proceedings of the ASME 2010 Interna-*

tional Mechanical Engineering Congress & Exposition, IMECE2010, Vancouver, British Columbia, Canada, November, 12-18 2010.

[12] CD-Adapco. *STAR-CD User Guide*, 2005.

[13] I. Celik, M. Klein, and J. Janicka. Assessment measures for engineering les applications. *Journal of Fluids Engineering*, 131(3):031102, 2009.

[14] I. B. Celik, Z. N. Cehreli, and I. Yavuz. Index of resolution quality for large eddy simulations. *Journal of Fluids Engineering*, 127(5):949–958, 2005.

[15] Showkat J. Chowdhury and Goodarz Ahmadi. A thermodynamically consistent rate-dependent model for turbulencež014part ii. computational results. *International Journal of Non-Linear Mechanics*, 27(4):705 – 718, 1992.

[16] D. Coles. The law of the wake in the turbulent boundary layer. *Journal of Fluids Mechanics*, 1:191–226, 1956.

[17] P. Darcy, S. Guerry, G. Latouchent, P. Barbier, and B. Fasolo. Multidimensional modelling of diesel particulate filter for regeneration control strategies. *Ingénieurs de l'automobile*, 799:29–35, 2009.

[18] Lars Davidson. Using isotropic synthetic fluctuations as inlet boundary conditions for unsteady simulations. *Advances and Applications in Fluid mechanics*, 1(1):1–35, 2007.

[19] Lars Davidson. Large eddy simulations: How to evaluate resolution. *International Journal of Heat and Fluid Flow*, 30(5):1016 – 1025, 2009.

[20] Lars Davidson. Fluid mechanics, turbulent flow and turbulence modeling. Lecture notes for courses TME075, TME256 and TME270, International Master's programme "solid and fluids mechanics", Chalmers University of Technology, Göteborg, Sweden, 2010.

[21] E. de Villiers. *The Potential of Large Eddy Simulation for the Modeling of Wall Bounded Flows*. PhD thesis, Imperial College of Science, Technology and Medicine, 2006.

[22] Mohamed Gad el Hak. Questions in fluid mechanics: Stokes' hypothesis for a newtonian, isotropic fluid. *Journal of Fluids Engineering*, 117(1):3–5, 1995.

[23] ERCOFTAC. Classic collection database. European Research Community on Flow, Turbulence and Combustion, 2011.

[24] Fa-Gung Fan and Goodarz Ahmadi. A sublayer model for turbulent deposition of particles in vertical ducts with smooth and rough surfaces. *Journal of Aerosol Science*, 24(1):45 – 64, 1993.

[25] G. Ferrari. *Motori a Combustione Interna*. Ed. Il Capitello, Torino, 2008.

[26] J. H. Ferziger and M. Perić. *Computational Methods for Fluid Dynamics*. Springer, 3rd edition edition, 2002.

[27] Fluent Inc. *Fluent 5 User's Guide*, 1998.

[28] C. Fureby and F.F. Grinstein. Monotonically integrated large eddy simulation of free shear flows. *AIAA Journal*, 37(5):544–556, 1999.

[29] M. Germano, U. Piomelli, P. Moin, and W. H. Cabot. A dynamic subgrid-scale eddy viscosity model. *Physics of fluids A*, 3:1760, 1991.

[30] B. J. Geurts and J. Frölich. A framework for predicting accuracy limitations in large-eddy-simulation. *Physics of fluids*, 14(6):L41–L44, 2002.

[31] J. W. Girard, F. Lacin, J. Hass, and J. Hodonsky. Flow uniformity optimization for diesel aftertreatment systems. SAE paper n. 2006-01-1092, SAE 2006 Int. Congress & Exp. (Detroit, Michigan), 2006.

[32] AVL List GmbH. *AVL FIRE Version 8 - Aftertreatment User Guide*, 2005.

[33] D. Greenblatt et al. A separation control cfd validation test case part 1: Baseline & steady suction. AIAA paper n. 2004-2220, 2nd AIAA Flow Control Conference, 28 June - 1 July 2004, Portland, OR (USA), 2004.

[34] D. Greenblatt et al. A separation control cfd validation test case part 2: Zero efflux oscillatory blowing. AIAA paper n. 2005-0485, 43nd AIAA Aerospace Sciences Meeting and Exhibit, 10-13 January 2005, Reno, NV (USA), 2005.

[35] C. Gutfinger and G. I. Tardos. Theoretical and experimental investigation on granular bed dust filters. *Athmosferic Environment*, 13:853–867, 1979.

[36] O. C. Haralampous, G. Koltsakis, and Z. Samaras. Partial regenerations in diesel particulate filters. SAE paper n. 2003-01-1881, SAE 2003 Int. Congress & Exp., Detroit, Michigan, 2003.

[37] Christian Hasse, Volker Sohm, and Bodo Durst. Numerical investigation of cyclic variations in gasoline engines using a hybrid URANS/LES modeling approach. *Computers & Fluids*, 39(1):25–48, January 2010.

[38] D. C. Haworth and K. Jansen. Large-eddy simulation on unstructured deforming meshes: towards reciprocating IC engines. *Computers & Fluids*, 29:493–524, 2000.

[39] C. Hinterberger, M. Olesen, and R. Kaiser. 3d simulation of soot loading and regeneration of diesel particulate filter systems. SAE paper n. 2007-01-1143, SAE 2007 Int. Congress & Exp. (Detroit, Michigan), 2007.

[40] Charles Hirsch. *Numerical Computation of Internal and External Flows*. Kindle Edition, 2007.

[41] C. Huynh, J. H. Johnson, S. Yang, S. Bagley, and J. Warner. A one-dimensional computational model for studying the filtration and regeneration characteristics of a catalyzed wall-flow diesel particulate filter. SAE paper n. 2003-01-0841, SAE 2003 Int. Congress & Exp. (Detroit, Michigan), 2003.

[42] K. Isomoto and S. Honami. The effect of inlet turbulence intensity on the reattachment process over a backward-facing step. *Journal of Fluids Engineering*, 111(1):87–92, 1989.

[43] H. Jasak. *Error analysis and estimation in the Finite Volume method with applications to fluid flows*. PhD thesis, Imperial College, University of London, 1996.

[44] F. Juretić and A. D. Gosman. Error analysis of the finite-volume method with respect to mesh type. *Numerical heat transfer, part B: fundamentals*, 57:414–439, 2010.

[45] W. Kim and S. Menon. A new dynamic one-equation subgrid-scale model for large eddy simulation. AIAA paper n. 1995-0356, 33rd Aerospace Sciences Meeting and Exhibit, January 9-12, 1995, Reno, NV (USA), 1995.

[46] W. W. Kim and S. Menon. Application of the localized dynamic subgrid-scale model to turbulent wall-bounded flows. In *Aerospace Sciences Meeting & Exhibit, 35th*, Reno, NV (USA), Jan, 6-9 1997. AIAA.

[47] R. B. Kinney. Fully developed frictional and heat-transfer characteristics of laminar flow in porous tubes. *International Journal of Heat and Mass Transfer*, 11:1393–1401, 1968.

[48] T. S. Klebanoff. Characteristics of turbulence in a boundary layer with zero pressure gradient. Technical Report TN 3178, NACA, 1954.

[49] M. Klein. An attempt to assess the quality of large eddy simulations in the context of implicit filtering. *Flow, turbulence and combustion*, 75:131–147, 2005.

[50] A. G. Konstandopoulos. Flow resistance descriptors for diesel particulate filters: Definitions, measurements and testing. SAE paper n. 2003-01-0846, SAE 2003 Int. Congress & Exp. (Detroit, Michigan), 2003.

[51] A. G. Konstandopoulos and J. H. Johnson. Wall-flow diesel particulate filters - their pressure drop and collection efficiency. SAE paper n. 890405, SAE 1989 Int. Congress & Exp. (Detroit, Michigan), 1989.

[52] A. G. Konstandopoulos, M. Kostogolu, E. Skaperdas, et al. Experimental studies of diesel particulate filters: Transient loading, regeneration and aging. SAE paper n. 2000-01-1016, SAE 2000 Int. Congress & Exp. (Detroit, Michigan), 2000.

[53] A. G. Konstandopoulos, M. Masoudi, et al. Inertial contributions to the pressure drop of diesel particulate filters. SAE paper n. 2001-01-0909, SAE 2001 Int. Congress & Exp. (Detroit, Michigan), 2001.

[54] A. G. Konstandopoulos, M. Masoudi, et al. Validation of a model and development of a simulator for predicting the pressure drop of diesel particulate filters. SAE paper n. 2001-01-0911, SAE 2001 Int. Congress & Exp. (Detroit, Michigan), 2001.

[55] V. Krishnan, K. D. Squires, and J. R. Forsythe. Prediction of separated flow characteristics over a hump using rans and des. AIAA-2004-2224, 2004.

[56] K. W. Lee and J. A. Gieseke. collection of aerosol particles by packed bed. *environmental science and technology*, 13:466–470, 1979.

[57] G. Mase. *Continuum Mechanics*. Schaum's outline. McGraw-Hill, 1969.

[58] P. Moin and J. Jimenez. Large eddy simulation of complex flows. In *24th AIAA Fluid Dynamics Conference*, Orlando (Florida), USA, 1993.

[59] A. Montorfano. Modellazione multidimensionale del meccanismo di deposizione del soot nelle trappole per il particolato. Master's thesis, Politecnico di Milano, July 2007. in Italian.

[60] P. E. Morgan, D. P. Rizzetta, and M. R. Visbal. Large-eddy simulation of separation control for flow over a wall-mounted hump. AIAA-2005-5017, 2005.

[61] OpenCFD Ltd. *OpenFOAM Programmer's Guide*, 2004.

[62] OpenCFD Ltd. *OpenFOAM User's Guide, v2.0.0*, 2011.

[63] F. Piscaglia and G. Ferrari. Development of an offline simulation tool to test the on-board diagnostic software for diesel after-treatment systems. SAE paper n. 2007-01-0133, SAE 2007 Int. Congress & Exp. (Detroit, Michigan), 2007.

[64] F. Piscaglia, A. Montorfano, G. Ferrari, and A. Onorati. Development of open-source CFD tools for the multi-dimensional simulation of diesel particulate filters. 63° Congresso Nazionale ATI, Palermo, September 23-26, 2008.

[65] F. Piscaglia, C. J. Rutland, and D. E. Foster. Development of a CFD model to study the hydrodynamic characteristics and the soot deposition mechanism on the porous wall of a diesel particulate filter. SAE paper n. 2005-01-0963, SAE 2005 Int. Congress & Exp. (Detroit, Michigan), 2005.

[66] S.B. Pope. *Turbulent flows*. Cambridge University Press, 2000.

[67] Alfio Quarteroni. *Modellistica Numerica per Problemi Differenziali*. Springer, 4 edition, 2008. in Italian.

[68] G Raithby. Laminar heat transfer in the thermal entrance region of circular tubes and two-dimensional rectangular ducts with wall suction and injection. *International Journal of Heat and Mass Transfer*, 14(2):223 – 243, 1971.

[69] C. M. Rhie and W. L. Chow. Numerical study of the turbulent flow past an airfoil with trailing edge separation. *AIAA journal*, 21(11):1525–1532, 1983.

[70] D. E. Rosner. *Transport processes in chemical reacting flow systems*. Butterworths, Stoneham, MA, 1985.

[71] H. Rusche. *Computational fluid dynamics of dispersed two-phase flows at high phase fractions*. PhD thesis, Imperial College, University of London, 2002.

[72] P. Sagaut. *Large eddy simulation for incompressible flows: an introduction*. Scientific computation. Springer-Verlag, 2006.

[73] F. Sbrizzai, P. Faraldi, and A. Soldati. Appraisal of three-dimensional numerical simulation for sub-micron particle deposition in a micro-porous ceramic filter. *Chemical Engineering Science*, 60:6551–6563, 2005.

[74] F. Sbrizzai, R. Verzicco, M. F. Pidria, and A. Soldati. Mechanisms for selective radial dispersion of microparticles in the transitional region of a confined turbulent round jet. *International Journal of Multiphase Flows*, 30:1389–1417, 2004.

[75] S. Sharipov and V. Seleznev. Data on internal rarified gas flows. *Journal of physical and Chemical Reference Data*, 27(3):657–706, 1998.

[76] Roger L. Simpson. Aspects of turbulent boundary-layer separation. *Progress in Aerospace Sciences*, 32(5):457 – 521, 1996.

[77] J. Smagorinsky. General circulation experiments with the primitive equations. i: the basic experiments. *Monthly Weather Review*, 91(3):99–165, 1963.

[78] R. M. C. So. Inlet centerline turbulence effects on reattachment length in axisymmetric sudden-expansion flows. *Experiments in Fluids*, 5(6):424–426, 1987.

[79] S. Song and J. K. Eaton. Reynolds number effectr on a turbulent boundary layer with separation, reattachment, and recovery. *Experiments in Fluids*, 36:246–258, 2004.

[80] P. R. Spalart, W.-H. Jou, M. Stretlets, and S. R. Allmaras. Comments on the feasibility of LES for wings and on the hybrid RANS/LES approach. In *Advances in DNS/LES, Proceedings of the First AFOSR International Conference on DNS/LES*, 1997.

[81] D. B. Spalding. A single formula for the law of the wall. *Journal of Applied Mechanics, Trans. ASME, Series E*, 28:455–458, 1961.

[82] G.R. Tabor and M.H. Baba-Ahmadi. Inlet conditions for large eddy simulation: A review. *Computers & Fluids*, 39(4):553 – 567, 2010.

[83] L. Thobois, G. Rymer, T. Soulères, and T. Poinsot. Large-eddy simulation in ic engine geometries. Sae Paper n. 2004-01-1854, SAE world Congress & exhibition, 2004.

[84] L. Thobois, G. Rymer, T. Soulères, T. Poinsot, and Van den Heuvel B. Large-eddy simulation for the prediction of aerodynamics in ic engines. In *Int. J. Vehicle Design "New strategies in Automotive Diesel Engines for Meeting Upcoming Pollutant Emission Restrictions"*, 2005.

[85] Eleuterio F. Toro. *Riemann solvers and numerical methods for fluid dynamics*. Springer, 2009.

[86] E. R. Van Driest. On turbulent flow near a wall. *Journal of the aeronautical sciences*, 23(11):1007–1011, 1036, 1956.

[87] H. K. Versteeg and W. Malalasekera. *An Introduction to Computational Fluid Dynamics*. Longman Scientific and Technical, 1995.

[88] B. Vreman, B. Geurts, and H. Kuerten. Comparison of numerical schemes in Large Eddy Simulation of the temporal mixing layer. *International Journal of Numerical Methods in Fluids*, 22:297–311, 1996.

[89] S. Šaric, S. Jakirlić, A. Djugum, and C. Tropea. Computational analysis of locally forced flow over a wall-mounted hump at high-re number. *Int J Heat Fluid Flow*, 27(4):707–720, 2006.

[90] H. G. Weller, G. Tabor, H. Jasak, and C. Fureby. A tensorial approach to computational continuum mechanics using object-oriented techniques. *Computers in Physics*, 12(6):620–631, 1998.

[91] D.E. Winterbone and R. J. Pearson. *Design Techniques for Engine Manifolds*. Professional Engineering Publishing, London, 2000.

[92] D.E. Winterbone and R. J. Pearson. *Theory of engine manifold design*. Professional Engineering Publishing, London, 2000.

[93] E. Wirojsakunchai, E. Schroeder, et al. Detailed diesel exhaust particulate characterization and real-time dpf filtration efficiency measurements during pm filling process. SAE paper n. 2007-01-0320 SAE 2007 Int. Congress & Exp. (Detroit, Michigan), 2007.

[94] Yong Yi. Simulating the soot loading in wall-flow dpf using a three dimensional macroscopic model. SAE paper n. 2006-01-0264, SAE 2006 Int. Congress & Exp. (Detroit, Michigan), 2006.

[95] D. You, M. Wang, and P. Moin. Large-eddy simulation of flow over a wall-mounted hump with separation control. Technical report, Center for Turbulence Research, Stanford University, 2005.